Dislocation Modeling in Face-Centered Cubic Metals: from Atomistics to Continuum

Von der Fakultät für Georessourcen und Materialtechnik der
Rheinisch-Westfälischen Technischen Hochschule Aachen

zur Erlangung des akademischen Grades eines

Doktors der Ingenieurwissenschaften

genehmigte Dissertation

vorgelegt von

M.Sc. Jaber Rezaei Mianroodi

aus Sary

Berichter: **Univ.-Prof. Dr. rer. nat. Bob Svendsen**
Prof. Dr. rer. nat. Alexander Hartmaier
Univ.-Prof. Dr. rer. nat. Reinhard Conradt

Tag der mündlichen Prüfung: 19.07.2016

Diese Dissertation ist auf den Internetseiten der Hochschulbibliothek online verfügbar.

Dedicated to my lovely wife and beloved parents.

Acknowledgements

I am truly and deeply grateful to Prof. Bob Svendsen for his fantastic scientific supervision. The amount of knowledge he has shared with me during our discussions is unbelievable and I owe this dissertation to him. I am also thankful for his infinite encouragements and supports. I am thankful to our former colleagues Dr.-Ing. Tobias Kayser and Prof. Dr.-Ing. Benjamin Klusemann for their help and discussions in our group. I would like to acknowledge Aachen Institute for Computational Engineering and Science (AICES) in RWTH-Aachen for academic and administrative supports, and for providing the required computational resources. Financial supports of the German Science Foundation (DFG) of Subproject A10 in the Collaborative Research Center SFB 761 is gratefully acknowledged. I would also like to thank all of my friends who supported me in writing, and encouraged me to strive towards my goal. My special thanks goes to Dr.-Ing. Reza Kebriaei, Dr.-Ing. Nima Hamidi Siboni, M. Sc. Shahed Rezaei, M. Sc. Muhammad Reza Hassani, M. Sc. Julian Kochmann, my brother M. Sc. Jamshid Rezaei Mianroodi as well as my wife M. Sc. Arghavan Afshar Bakeshloo whom I like to thank for proof-reading of this thesis. Finally I would like to gratefully thank my parents for their limitless support and encouragement toward my scientific career.

ABSTRACT

Dislocations in fcc crystals are studied here in several length and time scale regimes starting from atomistic calculations up to continuum models. Temperature-dependence of the stacking fault free energy (SFFE) for Fe is calculated utilizing the thermodynamic integration and a reference free energy model for solids based on the quasi-harmonic approximation. The underlying molecular dynamics (MD) simulation is based on the bond order potential for Fe of Müller et al. (2007). The SFFE of Fe at 0 K is calculated to be -20 mJ/m^2, negative due to the fact that the fcc phase is unstable at this temperature. The SFFE increases with temperature and becomes positive at around 200 K. Depending on system size, an SFFE for Fe between 5.5 and 9.1 mJ/m^2 is obtained at 298 K, increasing to between 70 and 80 mJ/m^2 at 1000 K. Next, the interaction between dislocations and stacking faults at low temperatures is studied with the help of MD. Observed interaction types in Cu include annihilation, penetration, and growth. Of particular importance is the mixed screw-edge character of the partial dislocations involved and the fact that the screw part cross slips more easily than its edge counterpart. The interaction of curved dislocations with twinned crystal is also studied with MD. In two of the in-plane shear loading directions, jerky stress flow is observed. Upon closer investigation, the jerky behavior is related to the fast motion of twin boundary. Next, the Peierls-Nabarro (PN) and Volterra (V) dislocation models are employed for dislocation-mediated bulk twin nucleation and growth. The dynamic model is applied to the modeling of variable dislocation separation in the twin. In this context, dislocations are closest together at the twin tip and increase in separation away from the tip. The phase field model for dislocation is based on periodic microelasticity (Wang et al. 2001, Bulatov & Cai 2006, Wang & Li 2010) to model the strongly non-local elastic interaction of dislocation lines via their (residual) strain fields. The energy storage is modeled here with the help of the "interface" energy concept and model of Cahn & Hilliard (1958) (see also Allen & Cahn 1979, Wang & Li 2010). The current approach is applied to determine the phase field free energy for Al and Cu. The identified models are then applied to simulate dislocation dissociation, stacking fault formation, glide and dislocation reactions in these materials. Transport and pile-up of infinite discrete dislocation walls driven by non-local interaction and external loading is also studied. The underlying model for dislocation wall interaction is based on the non-singular PN model. The influence of strongly non-local (SNL; long-range) interaction, and its approximation as weakly non-local (WNL; short-range), are studied. The pile-up behavior predicted by the current SNL-based continuous wall distribution modeling is consistent with that predicted by discrete wall distribution modeling (e.g., Roy et al. 2008, de Geus et al. 2013). Both deviate substantially from the pile-up behavior predicted by WNL-based continuous wall distribution modeling (e.g., Dogge 2014, Chapter 2).

ZUSAMMENFASSUNG

In dieser Dissertation werden Versetzungen in kubisch flächenzentrierten (kfz) Kristallen auf verschiedenen Längen- und Zeitskalen untersucht, von atomistischen Berechnungen bis hin zu Kontinuumsmodellen. Die Temperaturabhängigkeit der freien Energie von Stapelfehlern (SFFE) für Fe wird unter Verwendung der thermodynamischen Integration (TI) und einer Referenz für freie Energie-Modelle für Feststoffe berechnet, die auf der quasi-harmonischen Näherung basiert. Die zugrundeliegende Molekülardynamik (MD) Simulationen basieren auf dem Bindungsordnungspotential für Fe nach Müller et al. (2007). Die SFFE von Fe bei 0 K wurde als -20 mJ/m^2 berechnet. Das negative Vorzeichen resultiert aus der Instabilität der kfz-Phase bei dieser Temperatur. Die SFFE steigt mit zunehmender Temperatur und wird positiv bei etwa 200 K - bei dieser Temperatur ist die kfz-Phase metastabil. Abhängig von der Systemgröße liegt die SFFE für Fe zwischen 5.5 und 9.1 mJ/m^2 bei 298 K und erhöht sich bei 1000 K auf 70-80 mJ/m^2. Als nächstes wird die Wechselwirkung zwischen Versetzungen und Stapelfehlern bei niedrigen Temperaturen mit Hilfe von MD untersucht. Die observierten Interaktionstypen in Cu umfassen die Vernichtung, das Eindringen und Wachstum von Versetzungen. Von besonderer Bedeutung ist die Schrauben-Stufen-Eigenschaft der Partialversetzung und die Tatsache, dass der Schraubenanteil leichter quergleitet als sein Stufen Gegenstück. Das Zusammenspiel gekrümmter Versetzungen mit Zwillingskristallen wird als nächstes mit MD untersucht. In zwei der in der Ebene liegenden Scherrichtungen wird ein ruckartiger Spannungsfluss beobachtet. Bei näherer Untersuchung kann das ruckartige Verhalten auf die schnellen Bewegung von Zwillingsgrenzen zurückgeführt werden. Als nächstes werden die Peierls-Nabarro (PN) und Volterra (V) Versetzungs Modelle zur Beschreibung von versetzungs vermittelten Bulk Zwillingkeim und Wachstum eingesetzt. Insbesondere wird der dynamische Ansatz zur Modellierung variabler Versetzungstrennung in Zwillingen verwendet. In diesem Zusammenhang weisen Versetzungen den geringsten Abstand an der Zwillingsspitze auf. Das Phasenfeldmodell zur Modellierung von Versetzungen basiert insbesondere auf der Grundlage der periodischen Mikroelastizität nach (Wang et al. 2001, Bulatov & Cai 2006, Wang & Li 2010). Die stark nichtlokale elastische Wechselwirkung der Versetzungslinien wird über die Restspannungsfelder modelliert. Der Energiespeicher wird dabei auf der Basis des "Schnittstelle" Energiekonzepts und dem Modell nach Cahn & Hilliard (1958) (siehe auch Allen & Cahn 1979, Wang & Li 2010) modelliert. Der derzeitige Ansatz wird angewandt, um die freie Energie des Phasenfeldmodells für Al- und Cu zu bestimmen. Die identifizierten Modelle werden anschließend zur Modellierung von Versetzungs Dissoziation, Stapelfehlerbildung und dem Gleiten von Versetzungen in diesen Materialien verwendet. Der Transport und das Aufstauen (pile-up) unendlicher diskreter Versetzungswände unter nicht-lokaler Interaktion und externer Belastung wird ebenfalls untersucht. Das zugrundeliegende Modell für die Versetzungswand-Wechselwirkungen beruht auf dem nicht-singuläre PN-Modell. Der Einfluss der stark nichtlokalen (SNL; Langstrecken) Interaktion und seine schwach nichtlokale Annäherung (WNL; kurzer Reichweite) wird untersucht. Das pile-up Verhalten auf Basis der aktuellen SNL-Modell steht im Einklang mit dem Verhalten der diskreten Wandverteilungsmodellierung (z.B.., Roy et al. 2008, de Geus et al. 2013). Beide Ansätze weichen wesentlich von dem pile-up Verhalten WNL-basierter kontinuierlicher Wandverteilungsmodellierung (z.B.., Dogge 2014, Chapter 2) ab.

CONTENTS

1 Introduction **1**

1.1 Dislocations in fcc Metals 2

1.2 Stacking Faults and Twinning 4

1.3 Dissertation structure 5

I Atomistic Dislocation Modeling **7**

2 Stacking Fault Free Energy **9**

2.1 Introduction 9

2.2 Brief review of SFE calculation 10

2.3 Computational approach for finite temperature free energy 12

2.4 Application to free energy calculations for Fe 13

2.5 Results for stacking fault free energy 16

2.6 Conclusion 19

3 Straight Dislocation-Stacking Fault Interaction **21**

3.1 Introduction 21

3.2 Modeling approaches . . . 22
3.2.1 Partially periodic strain-controlled modeling . . . 23
3.2.2 Fully periodic stress-controlled modeling with finite-length stacking fault . . . 24
3.2.3 Fully periodic stress-controlled modeling with infinite stacking fault . . . 26
3.3 Periodic continuum & MD modeling of dislocation displacement field . . . 27
3.4 Results and discussion . . . 28
3.4.1 Comparison of strain-controlled and stress-controlled modeling . . . 28
3.4.2 Comparison of finite SF and infinite SF modelings . . . 31
3.4.3 Dislocation-SF interaction in different SF types . . . 31
3.4.4 Effect of interaction on material behavior . . . 35
3.5 Conclusion . . . 35

4 Twin Boundary Motion and Jerky Flow **37**
4.1 Introduction . . . 37
4.2 Simulation procedure . . . 38
4.3 Results and discussion . . . 39
4.3.1 Tensile loading . . . 39
4.3.2 Shear loading . . . 41
4.3.3 Details of twin boundary motion . . . 44
4.4 Conclusion . . . 47

II Continuum-Based Dislocation Modeling **49**

5 Critical twinning stress **51**
5.1 Introduction . . . 51
5.2 Twin model . . . 52
5.2.1 Geometry . . . 52
5.2.2 Twin disregistry function . . . 53

5.3 Energy model . . . 54
5.3.1 Total energy . . . 55
5.3.2 Interaction energy . . . 55
5.3.3 Stacking fault energy . . . 56
5.4 Comparisons for uniform dislocation separation . . . 58
5.5 Dynamic modeling . . . 62
5.5.1 Model relations . . . 62
5.5.2 Variable dislocation separation . . . 63
5.5.3 Effects of loading and twin thickness . . . 64
5.6 Conclusion . . . 64

6 Phase Field Based Dislocation Modeling **67**
6.1 Introduction . . . 67
6.2 Basic model relations . . . 69
6.3 Model formulation based on energy scaling . . . 71
6.4 Atomistic identification of the PF free energy model . . . 73
6.4.1 Basic properties and elastic energy . . . 73
6.4.2 Stacking fault energy . . . 74
6.4.3 Energy scaling . . . 75
6.5 Application to tensile loading of a dislocation loop . . . 77
6.6 Conclusion . . . 80

Appendices **83**
6.A Selected algorithmic & numerical details . . . 83
6.B Thermodynamic driving & Peach-Köhler forces . . . 84

7 Transport Based Dislocation Modeling **87**
7.1 Introduction . . . 87
7.2 Basic relations . . . 88

7.3 PN-based model for wall stress . . . 89
7.4 Weakly non-local approximation . . . 91
7.5 Algorithmic formulation . . . 91
7.5.1 Convolution integral . . . 91
7.5.2 Time discretization . . . 92
7.6 Results . . . 93
7.6.1 Mobility and boundary modeling . . . 93
7.6.2 Interaction stress for a fixed distribution . . . 94
7.6.3 Effect of boundary conditions . . . 95
7.6.4 Effect of loading and initial distribution . . . 97
7.6.5 Comparison of SNL- and WNL-based density and stress fields . . . 98
7.6.6 Effect of glide-plane spacing . . . 99
7.7 Conclusion . . . 100

Appendices **101**

7.A Comparison of selected Peierls-Nabarro- and Volterra-based relations . . . 101
7.B Characterization of the SNL-based maximum dislocation density . . . 102

8 Conclusion **105**

Bibliography **107**

List of Figures **115**

Index **119**

CHAPTER 1

INTRODUCTION

A versatile dislocation modeling approach is necessary for investigating complex alloys such as twinning induced plasticity (TWIP) or transformation induced plasticity (TRIP) steels. These steels are particularity interesting for industrial applications such as automotive manufacturing due to their high deformability and strength (Neu 2013). As it is shown in Figure 1.1 top, TWIP steels show high tensile strengths of about 1 GPa with high ductility at the same time. Their extraordinary deformability combined with high tensile strength makes them an excellent material for energy absorption applications. The source of such plastic behavior in TWIP steels is the formation of deformation twinning. The twins, as it is seen in HRTEM image in Figure 1.1 bottom-left, are the regions in the lattice with mirrored orientation with respect to the parent lattice. This change of the atomic orientation affects the dislocation motion and contributes to the hardening behavior of the material through interaction of the dislocations with stacking faults and secondary twins (Figure 1.1 bottom-right). Thus, investigating complex materials such as TWIP steels requires dislocation models capable of nucleation, glide, core transformation and stacking fault formation. The plastic flow in these steels are a combination of dislocation activity and twin growth. The phenomena contributing to the macroscopic strain-stress behavior shown in Figure 1.1 top panel are spanned across a wide range of length and time scales going down from continuum scales to atomistics. In addition, large-scale atomistic simulation of such alloys are usually impossible due to complexity of the chemical composition and the lack of empirical interatomic potential.

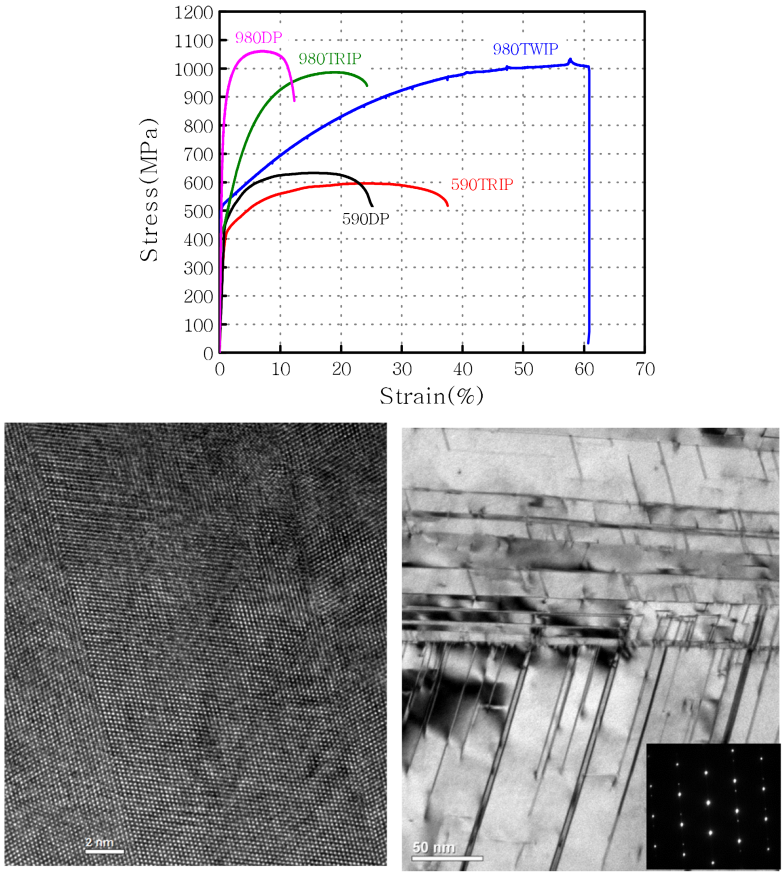


Figure 1.1: Top: stress-strain curves for a number of different steels compared with TWIP steels (Kwon et al. (2010)). Bottom-left: HRTEM image of a 10 nm wide twin in austenitic steel with the chemical composition of Fe-14 wt. % Cr-16% Mn-0.3% C-0.3% N after 20% deformation; showing the atomic structure at the twin interface. Bottom-right: Bright Field image of twins and stacking faults after 20% deformation exhibiting two sets of active twins (Beigmohamadi et al. (2014)).

1.1 Dislocations in fcc Metals

Permanent deformation of metals has been a source of fascination and progress through out the human history. Starting from shaping a bronze spear head up to manufacturing the blades of a gas turbine, all are founded on forming metals, the stiff, durable and accessible materials, into the desired shape. In the last century, digging deeper into the plasticity of metals has revealed a great deal of details about the source of their formidability with layers of complexities going down from continuum scale to the atomic scale. The beginning of the twentieth century is the dawn of the dislocation theory. Particularly the three groundbreaking papers in 1934 (i.e. Orowan 1934, Polanyi 1934, Taylor 1934) marked the start of the theory. The transformation, motion and interaction of dislocations are often irreversible and carry permanent deformation. Thus, the dislocations are the building blocks of the plastic deformation. The dislocations interact with other defects such as voids and grain boundaries as well. In addition to yield and plastic flow, dislocations are also responsible for creep, fatigue and ductility properties of crystalline

metals. A straightforward way to conceptualize the dislocations is through cut and move procedure as explained for example by Bulatov & Cai (2006). As it is shown in Figure 1.2 right, a dislocation is created when part of the lattice is cut and displaced while the other part is unchanged. When this dislocation glides and reaches the free surface, the lattice is permanently deformed, Figure 1.2 middle, while the structure is the same as the pristine lattice, Figure 1.2 left. This means the magnitude of the displacement (the Burgers vector $\boldsymbol{b}$) is the same as the lattice spacing in the direction of the displacement. The dislocations are also represented as a jump in the displacement field with induces an stress field in the material. A dislocation's motion is driven by the stress field of other dislocations as well as the external loading.

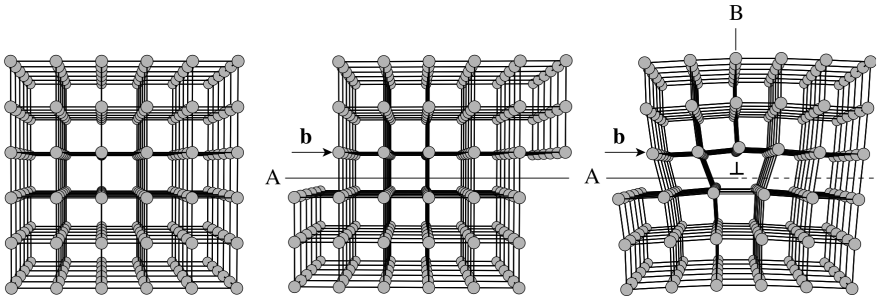


Figure 1.2: Left: pristine simple cubic lattice. Middle: permanently deformed lattice with no trace of dislocation inside the material after full glide of the dislocation. Right: An edge dislocation inside the lattice marked with $\perp$. When this dislocation glides to the right and goes out of the lattice, the material is permanently deformed with the configuration shown in the middle panel. Figure from Bulatov & Cai (2006)

A dislocation is characterized with its Burgers vector ($\boldsymbol{b}$ in Figure 1.2) and the line direction (normal to the paper in Figure 1.2). In case where the Burgers vector is perpendicular to the line direction the dislocation is called edge dislocation (Figure 1.3 left) and when it is parallel to the line direction it is called screw dislocation (Figure 1.3 middle). In general, in a mixed dislocation (Figure 1.3 right), the Burgers vector could have any angle with respect to the line direction. In this case the projection of the Burgers vector into the line direction is called screw component and the projection normal to the line direction is called edge component of a mixed dislocation.

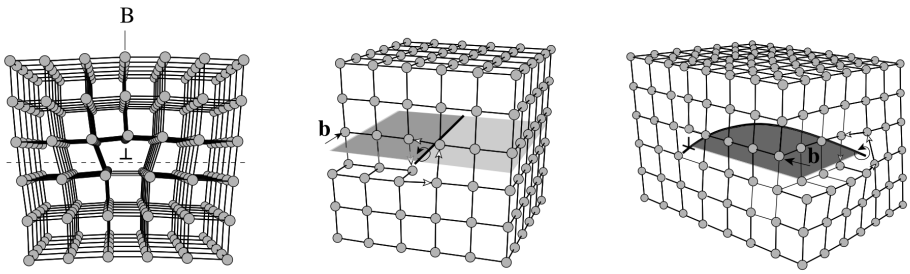


Figure 1.3: Left: edge dislocation. Middle: screw dislocation. Right: a mixed dislocation. Figure from Bulatov & Cai (2006)

A wide range of metals (for example Al, Cu, Ag, Au, Ni as well as austenite steels) have close packed crystal structure. In fcc crystals, close packed planes (i.e. (111) planes) are the most energetically favorable planes for the dislocations to nucleate and glide. The energetically favorable directions of the

Burgers vector is also determined by the crystallography of the fcc lattice. These are usually presented in form of the Thompson tetrahedron shown in Figure 1.4. The four close packed planes are rotated into a same plane in this figure for ease of visualization. In each of the glide planes, there are three perfect dislocations (with full Burgers vector) in form of $\{110\}$ and three partial dislocations in form of $\{112\}$.

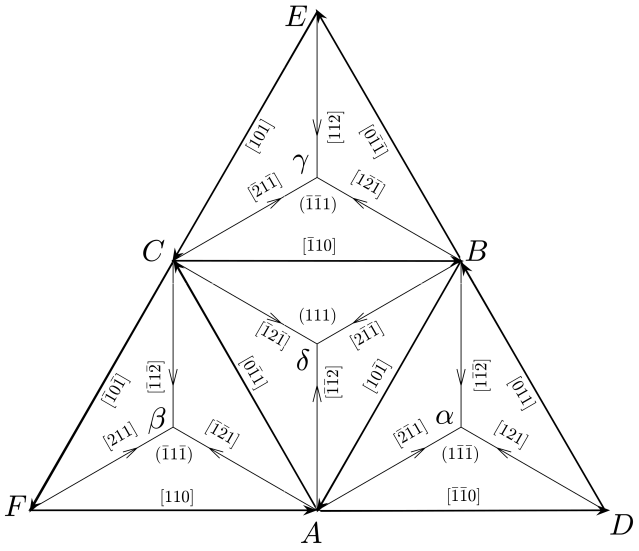


Figure 1.4: Thompson tetrahedron for fcc crystals showing the favored Burgers vector directions

1.2 Stacking Faults and Twinning

In most of the fcc metals, a perfect dislocation dissociates into two partial dislocations due to the lower energy of the dissociated state. The partial dislocations have a shorter Burger vector and thus lower energy concentration compared to the perfect dislocations. This is considered as a dislocation core transformation in fcc metals with

$$\boldsymbol{AB} \rightarrow \boldsymbol{A\delta} + \boldsymbol{\delta B} \tag{1.1}$$

for the Burger vectors shown in Figure 1.4. The elastic interaction force between the two partial dislocations is repulsive. However, their separation is finite since the dissociation also creates stacking fault (SF) in the fcc lattice structure which has an energy cost. The SF is bounded between the two partial dislocations and thus although an increase in the separation of the two partial dislocations reduces the interaction energy, it increases the stacking fault energy (SFE). The balance between the two forces determines the equilibrium SF width. The dissociation, in other words, is a process in which the line defects (dislocations) are sources for nucleation of surface defects (SFs). The surface faults also lead to volumetric changes in the material in terms of fcc to hcp transformation as well as twin formation.

In fcc crystals, close packed planes, i.e. (111), are usually designated by three letters: "A", "B" and "C" to emphasize that in fcc three different stacking sequences of (111) planes are available. The whole lattice is then represented as ..ABCABCABC... In the case of twinning, at the twin boundary the stacking sequence suddenly changes in a way that it is the mirrored sequence compared to the other side of the boundary, that is ..ABCA**B**ACBA.. with "**B**" representing the twin boundary. Since "**B**" has two "A" s in

its vicinity, it has the stacking sequence of an hcp lattice. Except this one layer of hcp (the twin boundary), the other parts of the lattice have fcc sequence. However, since the lattice structure is mirrored on the other side, its elasticity tensor as well as the dislocation glide planes, i.e. (111) planes, are different from the parent fcc phase.

As discussed in many works (e.g., Christian & Mahajan 1995), the formation of twinned regions in fcc metals is related to the partial dislocation nucleation and growth of lattice regions bounded by stacking faults in which atomic planes have been restacked by the passage of partial dislocations, resulting in lattice reorientation. Dislocation-based deformation mechanism in fcc systems such as glide and twinning are influenced by a number of factors which can be broadly categorized into material and environmental. In particular, on the environmental side, temperature and stress environments are important factors. Examples of the latter include boundaries such as crack tips and grain boundaries. Besides factors such as grain (system) size, loading conditions, temperature (e.g., Liu et al. 2014, Liang 2014), and/or complex microstructure, (e.g., Steinmetz et al. 2013), the twinning process is in general affected by dislocation interaction and by the energy required to form stacking faults (SFs), i.e., the stacking fault energy (SFE). In particular, if the SFE is smaller than the energy needed to form trailing partials, SFs may grow and result in twin formation. This can happen even in materials having a relatively large SFE due to other factors, e.g., grain size. Indeed, despite its large SFE, Chen et al. (2003) observed twin formation in nanocrystalline aluminium due to the small grain size. As discussed by Li et al. (2011), bulk or "inherent" twinnability of fcc metals can be viewed as a competition between the nucleation of a twinning partial dislocation (i.e., leading partial plus stacking fault) and trailing partial dislocation nucleation. Expressed more precisely, the competition here is between (i) further stacking fault growth, and (ii) trailing partial nucleation. As such, the energy required to grow further stacking fault, i.e., the SFE, is decisive here.

1.3 Dissertation structure

The dissertation is divided in to two parts, the first part is mainly focused on the atomistic modeling of dislocation properties and processes while the second part includes continuum-based models. The main portion of the first part is based on molecular statics (MS) and molecular dynamics (MD) simulations. Thermodynamic integration (TI) as well as quasi-harmonic approximation (QHA) are also used in the atomistic part of the dissertation. These chapters provide the detailed insight at the atomic level to the dislocation processes.

In chapter 2, the temperature dependency of the SFE is investigated. This is in particular important for materials with highly temperature dependent properties like Fe. QHA is employed here to calculate the free energy at low temperatures. Afterwards, TI is used to integrate low temperature free energy up to higher temperatures. The method is verified with comparison between the calculated fcc-bcc free energy of Fe as a function of temperature and the data available literature. As it was expected for Fe, increasing the temperature, increases the stacking fault free energy (SFFE).

In chapter 3, MD is used to simulate dislocation interaction with SFs. Any influence on the motion of dislocations directly effects the flow behavior of the material. Several different configurations are studied here. These include configurations with finite SF and infinite SF layers. The simulations are also performed both with strain controlled loading and stress controlled one. Two materials with relatively high (Al) and low (Cu) SFEs are modeled in this chapter. For Al, not surprisingly, most of the interaction modes are annihilation of the SF layer due to high SFE. For Cu, however, depending of the loading

condition and the SF type, three modes of annihilation, growth and penetration of the dislocation-SF interaction are identified and studied in details.

Chapter 4 is dedicated to study the interaction of volumetric phases (in particular twinned lattice) with the dislocations under external loading using 3D MD simulations. The effect of these interactions on the stress-strain curve is documented and interpreted in details. Four configurations consisting of fcc Cu with and without the twinned region and with and without a void are considered and compared with each other. The voids are added to facilitate the dislocation nucleation in contrast to the homogeneous nucleation in the configurations without voids. For each of these configurations, all possible loading directions, three shear and three normal, are investigated. Shear loading of the twinned crystal shows jerky flow in stress curve. Closer look at the atomistic simulations shows that the jerky stress behavior is due to the fast twin boundary motion.

The second part of the dissertation is dedicated to the continuum-based models, however, the connection to the atomistic realm is kept alive. In most of the cases, the data for the continuum models are obtained from atomistic simulations. In most of the cases, the results of the continuum model are also compared directly with their atomistic counterparts. Up-scaling from atomistic to continuum model is necessary to study the collective behavior of the dislocations at larger length and longer time scales.

In chapter 5, a combination of the continuum dislocation theory and atomistic data for SFE is used to predict the twinning stress. The model used for the calculation consists of partial dislocations stacked on top of each other which is the same structure visible in MD. The continuum dislocation model here is based on Peierls-Nabarro (PN) model in which the lattice periodicity and the finite core size are taken into account. As a result, the PN model predicts finite stress level at the dislocation core. The model in compared with singular Volterra-based model with infinite stress at the core in terms of the dislocation separation and the critical twinning stress. As expected, the Volterra model predicts infinite nucleation stress while the PN model results in finite nucleation stresses comparable to the nucleation stresses calculated with atomistics.

Chapter 6 provides a phase field (PF) model for general dislocation configurations in fcc crystals. The model is fully based on the atomistic data with no free parameter or external data source necessary. The phase field model provides several advantages compared to full atomistic simulations, e.g. the time scale of the PF simulations are much longer than the MD calculations. In addition, in cases of complex materials for which no empirical potential is available for full molecular simulation, the phase field approach can be used for large-scale simulations with the help of density functional theory. In other words, the model itself does not rely on the availability of an empirical interatomic potential.

Finally, in chapter 7, dislocation wall pile-up is studied. Here, instead of focusing on individual dislocations as in the previous chapters, the collective behavior of dislocation distribution is modeled through the dislocation transport theory. Non-local interaction of dislocations are based on PN dislocation model. The strongly non-local (SNL) model is compared here with the gradient-based weakly non-local (WNL) model in the dislocation pile-up context. In the SNL model the long range interaction of dislocations are fully taken into account while the WNL is based on the fist order term in the Taylor expansion of the stress field. The results show substantial differences in pile-up behavior near the boundary between the two models.

Part I

Atomistic Dislocation Modeling

CHAPTER 2

STACKING FAULT FREE ENERGY*

"You would make a ship sail against the winds and currents by lighting a bonfire under her decks? I have no time for such nonsense."

-Napoleon Bonaparte, 1800

2.1 Introduction

The microphysical and in particular dislocation mechanisms lying behind the thermomechanical deformation behavior of fcc metals are strongly influenced by the stacking fault energy (SFE). The SFE influences the stability of ideal dislocations, resulting in the predominance of dislocation glide and cross-slip in high SFE metals, and other mechanisms such as twinning in low SFE metals. Moreover, lower SFE affects the effective mobility of dislocations, impedes cross-slip and hinders cell structure formation, for example in austenitic steel. In medium to high SFE metals (e.g. Cu, Ni and Al), the microstructure evolves through the formation of dislocation cells. In contrast, in low SFE metals such as austenitic stainless steel, twinning and microbanding prevail.

Wei & Wei (2012) have shown that the interaction modes between the dislocations and planar faults are related to the SFE of the material. Furthermore, the deformation mechanism (i.e. dislocation glide plasticity or twining induced plasticity) is determined by SFE. In a number of fcc materials such as copper or aluminum, as well as more complex materials such as high magnanese steels exhibiting so-called twinning-induced plasticity (i.e., TWIP steels), the interaction between dislocations and other defects such as stacking faults (SFs) or twins plays an important role in their deformation behavior.

*This chapter is based on the work in Mianroodi & Svendsen (2016*a*)

Depending on the particular material, the process, and the environment conditions, this interaction can lead to twinning or detwining, determining the dominant deformation mechanism. In the case of TWIP materials, for example, dislocation-twin interaction may inhibit dislocation movement and result in significantly higher strength and hardening (e.g., Bouaziz et al. 2011).

The generalized stacking fault energy (GSFE) concept of Vitek (1968) has been employed in many studies at fixed and generally zero temperature to calculate the SFE for many different fcc materials. Given its strong temperature dependence and the relevance of the SFE for the stability of dislocation and deformation processes at finite temperature, it is useful to develop methods to extend these molecular statics (MS)-based zero temperature calculations of the SFE to finite temperature.

The purpose of the current work is to propose a computational approach to calculate the SFE as a function of temperature using the results of MD simulation and apply it to fcc metals. This temperature-dependent SFE is referred to in this work as the stacking fault free energy (SFFE), in contrast to SFE which is without temperature and entropy correction. To this end, MD simulation is combined with thermodynamic integration (TI) (e.g., Frenkel et al. 2002) and a reference free energy model based on the quasi-harmonic approximation (e.g., Tadmor & Miller 2011, §11.4).

To demonstrate the applicability of this approach, it is applied to the calculation of the SFFE of Fe in the range from 0 to 2000 K using the analytic bond order potential (ABOP) of Müller et al. (2007). This interatomic potential is one of the most successful potentials for temperature driven phase transitions in iron. It also gives relatively good properties for both fcc and bcc iron phases. The accuracy of the proposed approach is verified by reproducing the fcc-bcc free energy difference of Fe calculated by Müller et al. (2007). The MD calculations are performed using the LAMMPS package (Plimpton 1995). Simulation results are also visualized with the help of the OVITO package (Stukowski 2010).

2.2 Brief review of SFE calculation

For completeness, the conventional method to calculate the SFE at zero temperature (e.g., Vitek 1968, Boyer et al. 2004) is briefly summarized. In particular, this is based on the MS simulation box shown in Figure 2.1. This box is periodic in the x ($[1\bar{1}0]$) and y ($[11\bar{2}]$) directions, and bounded by a free surface in the z ($[111]$) direction. The box dimensions are $L_x = 10\sqrt{2}\,a_0$, $L_y = 6\sqrt{6}\,a_0$, and $L_z = 10\sqrt{3}\,a_0$ in terms of the lattice constant a_0 ($a_0 = 4.050$ Å for Al, $a_0 = 3.615$ Å for Cu, $a_0 = 3.611$ Å for fcc Fe).

After relaxation and energy minimization, the MS simulation starts from ideal fcc lattice with orientations shown in Figure 2.1. During the simulation, the upper half of the model is displaced rigidly in y direction, resulting in a fault plane of area A_f and a change in internal energy per unit area of

$$\gamma_\mathrm{SF} = \frac{E_\mathrm{f}/N_\mathrm{f} - E_\mathrm{i}/N_\mathrm{i}}{A_\mathrm{f}/N_\mathrm{f}} \,. \tag{2.1}$$

where E_a represents the internal energy and N_a is the number of atoms in the ideal ($a = \mathrm{i}$) and faulted ($a = \mathrm{f}$) configurations. Atoms at the distance from the free surfaces in z direction smaller than cutoff radius of the potential are excluded from energy calculations to remove the surface effect. Since there is no box relaxation in z direction during rigid displacement, the calculated SFE is called unrelaxed SFE (Zimmerman et al. 2000). In contract to this case, we have also considered the case where the simulation box is relaxed in z direction and the box is periodic in z with $L_z = 12\sqrt{3}\,a_0$. The SFE calculated in latter case is called relaxed SFE throughout this work. Periodicity in z direction results two SF layers, one

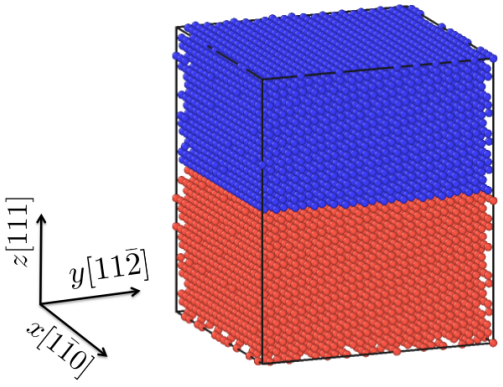


Figure 2.1: Simulation box for calculation of the SFE. The SF is created by rigidly displacing the upper part (blue) with respect to the (fixed) lower part (red). See text for details.

between the two regions in the middle of the box and another one at the boundary between two periodic images. Thus, in the relaxed simulations, the energy calculations are done in the regions between $z = \frac{L_z}{4}$ to $z = \frac{3L_z}{4}$ to include only one SF layer.

To briefly illustrate the procedure, consider for example the calculation of the SFE for Cu at zero temperature (e.g., Ezaz et al. 2011, Wei & Wei 2012) as based on the embedded atom potentials of Mishin et al. (2001). The results of this are shown in Figure 2.2. For the MD calculations involved, a time step of 2 fs has been used. To begin, a stepwise displacement of $a_0\sqrt{6}/6$ in the y direction forces the system over the unstable stacking fault energy barrier γ_{USF} in Figure 2.2 at $b = \frac{1}{2}$, results in restacking (blue layers in Figure 2.2a) and the formation of an intrinsic SF (ISF) at $b = 1$ with energy of γ_{ISF}. A second rigid displacement of the upper half with respect to the lower half from $b = 1$ to $b = 2$ results the energy increase from a to b'. Since this energy barrier (ab') is relatively large, the system chooses another path (ab). In MD simulations, this is modeled by adding one atomic layer from the moving upper half to the fixed lower half. Applying the second rigid displacement to the new upper half, forces the system over the barrier γ_{UTF} at $b = \frac{3}{2}$ and results in further restacking (Figure 2.2b) and growth of the ISF into an extrinsic stacking fault (ESF) at $b = 2$ with energy of γ_{ESF}. Since growth from an ISF to a ESF takes less energy than the second rigid displacement of the upper blue layer in Figure 2.2a from $b = 1$ to $b = 2$, this is favored. In the simulation, this fact is utilized by repeatedly fixing last restacked layer to the lower half of simulation box for the next rigid displacement step to avoid such high energy barriers like ab'. Further rigid displacement over the energy barrier at $b = \frac{5}{2}$ results in further growth of the ESF into a twinning stacking fault (TSF) at $b = 3$ and energy of γ_{TSF}. Continued rigid displacement together with fixing the last restacked layer every time a full displacement of $[11\bar{2}]$ is applied, leads to twin nucleation and growth. Note that the explained SFE calculation method is multi-layer, i.e. after each full displacement in direction of $[11\bar{2}]$, the adjacent close packed layer is activated. Thus, the system will not go back to fcc. Instead, the two hcp layers will move apart from each other. If the displacement is always restricted to a single atomic layer (i.e. choosing energy path ab'), then after b' the system goes back to fcc and zero relative energy. However, since twinning and twin growth is focus of this work, we continue to work with the multi-layer SFE.

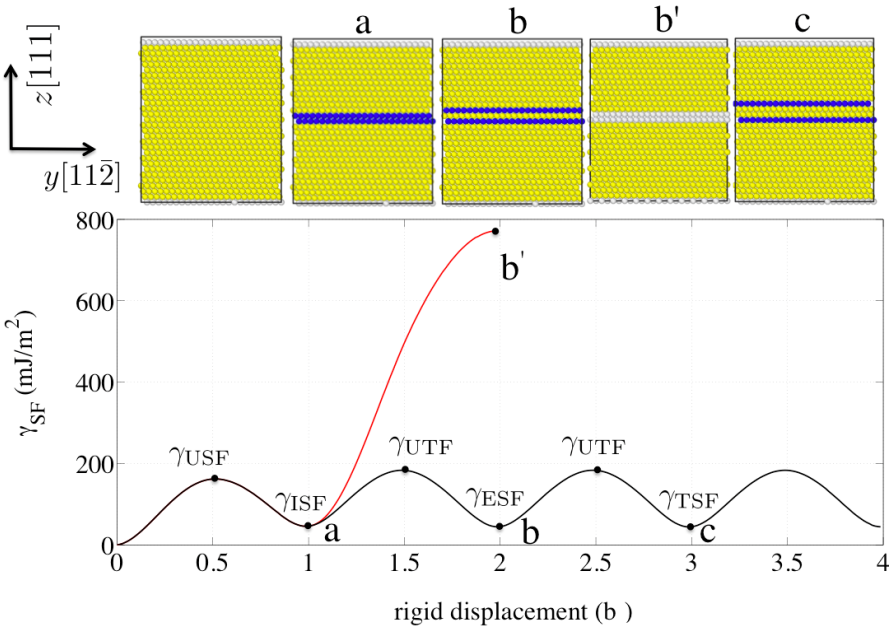


Figure 2.2: Atomic configuration (above) and $\gamma_{\rm SF}$ from (2.1) as a function of rigid displacement in the y ($[11\bar{2}]$) direction in units of b ($\frac{1}{6}|[11\bar{2}]|$) (below) for Cu. See text for details. The determination of local atomic coordination as depicted in the atomic configurations above is based on common neighbor analysis (CNA): fcc (yellow), hcp (blue), unknown (i.e., free surface; white).

2.3 Computational approach for finite temperature free energy

Since we consider constant number-stress-temperature (NST) conditions, the Gibbs free energy G is relevant. In what follows, we also work with the relation

$$G(T,\boldsymbol{P}) = F(T,\boldsymbol{F}) - V_0\,\boldsymbol{P}\cdot\boldsymbol{F} \tag{2.2}$$

between G and the Helmholtz free energy F in terms of the initial volume V_0, the first Piola-Kirchhoff stress $\boldsymbol{P}$, and the deformation gradient $\boldsymbol{F}$. As usual (e.g., Frenkel et al. 2002), thermodynamic integration (TI) is based on integration of the equilibrium thermodynamic relation $E = G - T\,\partial G/\partial T$ at zero stress, yielding

$$\frac{G(T,\mathbf{0})}{T} = \frac{G(T_0,\mathbf{0})}{T_0} - \int_{T_0}^{T} \frac{E(\theta)}{\theta^2}\,d\theta\,. \tag{2.3}$$

In this relation, the internal energy $E(T)$ is obtained from a series of MD simulations at temperature between T_0 and T_1 at zero stress. As a model for $G(T_0,\mathbf{0})$, the quasi-harmonic approximation (QHA)

$$F_{\rm QH}(T,\bar{\mathbf{r}}) = F^{\rm kin}(T) + F^{\rm pot}_{\rm QH}(T,\bar{\mathbf{r}}) \tag{2.4}$$

to F is employed (e.g., Tadmor & Miller 2011, §11.4). Here, $\bar{\mathbf{r}}$ is the array of mean atomic positions modeled as minima of $F_{\rm QH}(T,\mathbf{r})$, $F^{\rm kin}(T)$ is the kinetic part of $F_{\rm QH}$, and

$$F^{\rm pot}_{\rm QH}(T,\bar{\mathbf{r}}) = U(\bar{\mathbf{r}}) + \frac{k_{\rm B}T}{2}\ln\left(\frac{\prod_{r=1}^{n_{\rm nz}}\lambda_r(\bar{\mathbf{r}})}{(2\pi k_{\rm B}T)^{n_{\rm nz}}}\right) \tag{2.5}$$

its potential part ($k_{\mathrm{B}}T \ll 1$) in terms of the interatomic potential U and Boltzmann's constant k_{B}. Further, $\lambda_r(\bar{\mathbf{r}})$, $r = 1, \ldots, n_{\mathrm{nz}}$, represent the non-zero eigenvalues of the force-constant matrix $\partial_{\mathbf{r}}\partial_{\mathbf{r}}U(\bar{\mathbf{r}})$. Although analytical expressions for the derivatives of potentials U of the bond-order type being considered here for Fe have been worked out in the literature (e.g., Porter et al. 1997), it is more convenient to employ algorithmic differentiation methods for this purpose. In this work, the ADOL-C package (Walther & Griewank 2012) has been used.

As one can imagine, the accuracy of the results is highly dependent on the number of simulations used as well as the details of the integration procedure. In addition, the reference temperature T_0 should be as low as possible to insure the validity of the quasi-harmonic approximation. These issues are discussed in the sequel.

2.4 Application to free energy calculations for Fe

To test the current MD-based approach to finite-temperature free energy calculations just discussed, we begin by applying it to calculate the free energy difference between the bcc and fcc phases of Fe as a function of temperature at constant stress and compare the results with those of Müller et al. (2007). In contrast to the unrelaxed 0 K case, the simulation box employed for finite temperature calculations is periodic in all directions as shown in Figure 2.3. For SFFE calculations, two system sizes

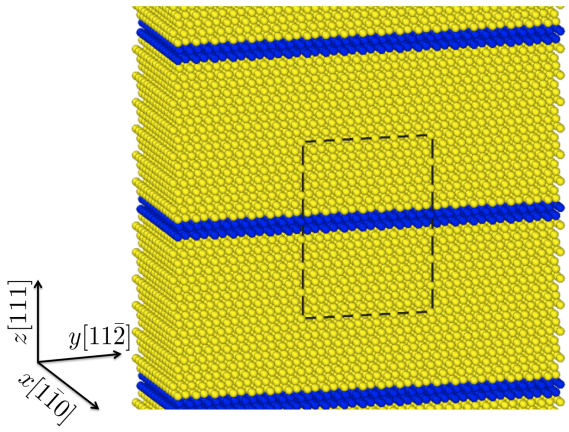


Figure 2.3: Periodic simulation box used for phase transition and SFFE calculations. Lattice regions (yellow) are fcc or bcc, SF regions (blue) are hcp. For the phase transition calculations, of course, there is no SF.

are considered, i.e., 3920 atoms ($L_x = 7\sqrt{2}\ a_0, L_y = 7\sqrt{6}\ a_0/2, L_z = 20\sqrt{3}\ a_0/3$) and 5888 atoms ($L_x = 8\sqrt{2}\ a_0, L_y = 8\sqrt{6}\ a_0/2, L_z = 23\sqrt{3}\ a_0/3$). In the case of the SFFE calculations, in order to avoid the interaction between SF layers in the periodic images, it is necessary to choose the box size large enough.

To begin, the energy of the starting configuration is minimized using conjugate gradient method. After that, the models are relaxed using NPT ensemble at zero stress and constant temperature. Unless otherwise is stated, throughout this work, the damping coefficients for the thermostat and barostat are set to

200 and 2000 times the time step size, respectively. These values provide a good relaxation time with small fluctuations. The use of (2.3) to calculate $G(T, \mathbf{0})$ is based on a series of MD simulations at zero stress and NT conditions which are performed at 10 K intervals up to the desired temperature $T = T_1$ to determine $E(T)$. Each MD simulation is carried out for 15000 time steps of 2 fs. The value of $E(T)$ for each MD simulation is obtained by averaging in the last 5000 steps. The array $\bar{\mathbf{r}}$ of average atomic positions is also calculated using the last 5000 steps at $T_0 = 10$ K. The lower T_0, the more accurate $G(T_0, \mathbf{0}) = F_{\mathrm{QH}}(T_0, \bar{\mathbf{r}})$ from (2.4) and (2.5). Using Nose-Hoover chain thermostat and barostat with chain number of 3 produces good statistics for the low temperature simulations. The calculated free energies for fcc and bcc phases of Fe using QHA alone and also QHA as reference for thermodynamic integration of (2.3) are shown in Figures 2.4 and 2.5, respectively.

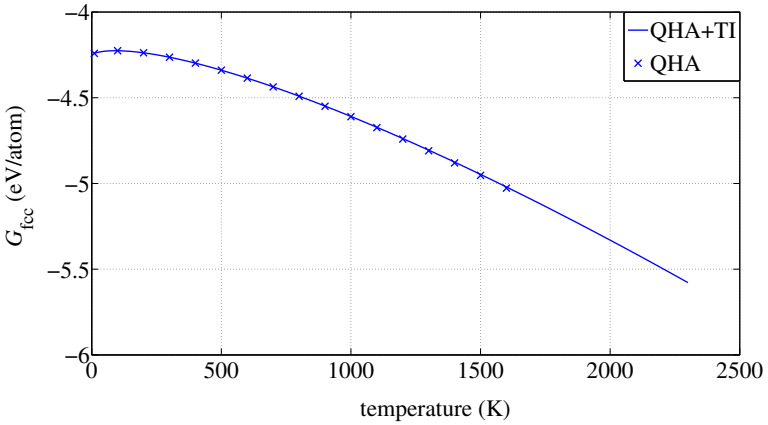


Figure 2.4: Free energy of fcc iron as a function of temperature calculated using QHA and QHA as reference for thermodynamic integration (TI)

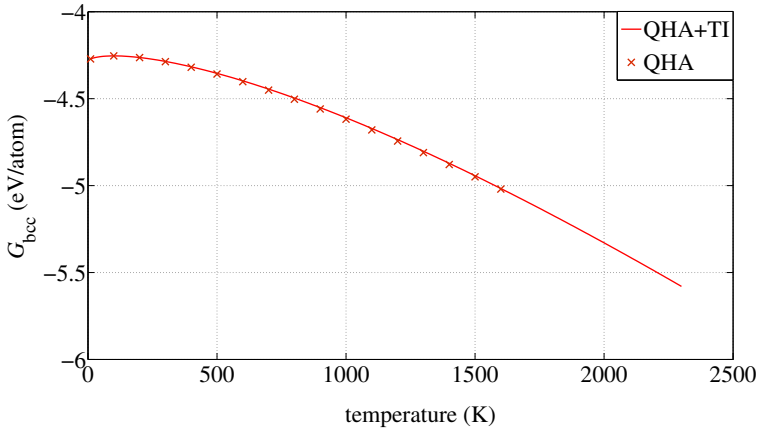


Figure 2.5: Free energy of bcc iron as a function of temperature calculated using QHA and QHA as reference for thermodynamic integration (TI)

As it is seen from Figures 2.4 and 2.5, the energy difference between QHA and QHA together with ther-

modynamic integration is relatively small. However, drawing the difference as function of temperature for two phases reveals the anharmonicity effect on the free energy as shown in Figures 2.6. The anharmonicity at largest is in order of 8 $meV/atom$. However, since the fcc-bcc energy difference at 0 K is about 30 $meV/atom$, this small anharmonicity is important and as we will see, it changes the phase transition behavior of Fe resulting in two phase transition points one at 1030 K for bcc to fcc transition and another one at 2210 K for fcc to bcc transition.

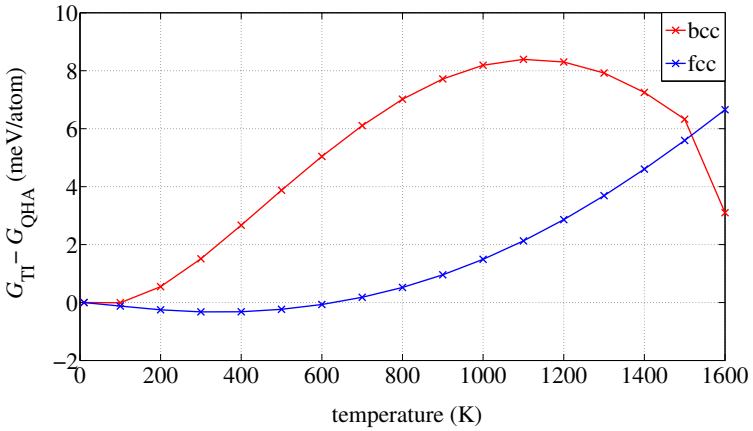


Figure 2.6: Free energy difference due to anharmonicity between QHA method and thermodynamic integration as function of temperature for both fcc and bcc phases of iron

To carry out the integration in (2.3), the MD data for $E(T)$ are fit to splines. Spline fit was necessary since the polynomial fit was not sufficiently accurate, especially for low starting temperatures like $T_0 = 10$ K. As to be expected, calculation of $G(T, \mathbf{0})$ in this way is sensitive to the choice of T_0 and the fit of $E(T)$ to the MD data. This is shown in Figure 2.7 in the case of least-squares-based polynomial fitting and application to the calculation of the fcc-bcc free energy difference for Fe. In most cases, the least-square

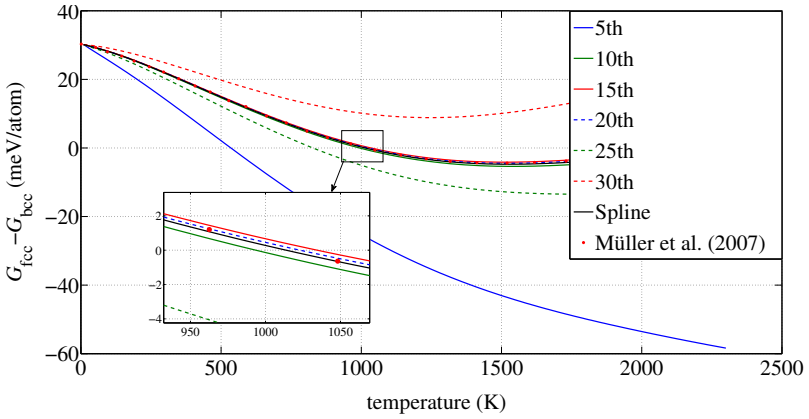


Figure 2.7: Calculated energy difference between the fcc and bcc phases of Fe based on TI and QHA for polynomials of different order fit to the MD data for $E(T)$. The corresponding spline fit and the results from Müller et al. (2007) are shown.

fit results in deviations between the data and the fitted curve $E(T)$; in particular, it does not fit all data points exactly. This in turn leads to errors in the integration. On the other hand, splines always fit the data points exactly, guaranteeing accurate integration results.

The free energy difference between the fcc and bcc phases of Fe calculated as a function of temperature using the QHA alone is compared with the spline-fit-based TI-QHA method just discussed in Figure 2.8. As apparent via the comparison with the results of Müller et al. (2007), the QHA is not accurate for

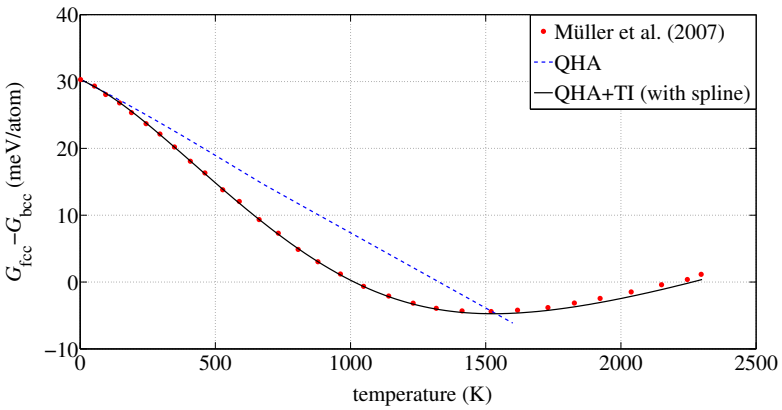


Figure 2.8: Comparison of calculated free energy difference between fcc and bcc phases of Fe as a function of temperature using different methods. These include (i) the QHA alone (blue dashed curve), (ii) the QHA coupled with TI (solid black curve), and (iii) the results of Müller et al. (2007) (red dots).

temperatures above 100K. On the other hand, the QHA of the free energy at $T_0 = 10$ K combined with spline fitting of the MD data for $E(T)$ and TI results in very good agreement with the results of Müller et al. (2007). As such, this model for $G(T, \mathbf{0})$ is employed for the SFFE calculations, to which we now turn.

2.5 Results for stacking fault free energy

To begin, consider the SFE for Al, Cu and Fe at 0 K. Mishin EA potential (Mishin et al. 2001, 1999) and ABOP of Müller et al. (2007) are used for Cu, Al and Fe, respectively. Values for the relaxed and unrelaxed SFEs for these are listed in Table 2.1. The relaxed and unrelaxed energy pathways for these materials are also displayed in Figures 2.9, 2.10 and 2.11.

As it is seen in Table 2.1, the calculated relaxed SFEs are in good agreement with previously reported values (e.g., Wei & Wei 2012). However, the unrelaxed SFEs are a bit different from the results of Wei & Wei (2012). The difference is more clear in the case of unstable SFEs (γ_{USF} and γ_{UTF}). As shown by Zimmerman et al. (2000), in the most cases, unrelaxed calculation gives the same stable SFE and slightly higher unstable SFE in comparison to relaxed calculation.

In the case of Fe, the relaxation in z direction changes the shape of the unstable SFE pathway as it is seen in Figure 2.11. Considering this figure, a new stable stacking fault region is clearly visible at $b = \frac{1}{2}$ with 27 mJ/m^2 depth of its energy well. However, since the value of SFE is relatively high at this point, for

	SFE (mJ/m^2)				
Material	γ_{USF}	γ_{ISF}	γ_{UTF}	γ_{ESF}	γ_{TSF}
Al unrelaxed (this study)	188.6	155.5	239.1	156.3	157.1
Al relaxed (this study)	167.3	145.4	220.8	150.9	151.3
Al (Wei & Wei 2012)	168.1	145.9	220.3	150.4	150.6
Cu unrelaxed (this study)	182.1	44.5	203.5	44.5	44.5
Cu relaxed (this study)	162.1	45.8	183.4	44.5	44.2
Cu (Wei & Wei 2012)	162.0	44.3	183.3	44.4	44.4
fcc Fe unrelaxed (this study)	244.6	-19.7	231.0	-19.7	-19.6
fcc Fe relaxed (this study)	245.8	-19.5	232.0	-19.9	-20.7

Table 2.1: relaxed and unrelaxed stacking fault energies of Al, Cu and fcc Fe at 0 K (see Figure 2.2).

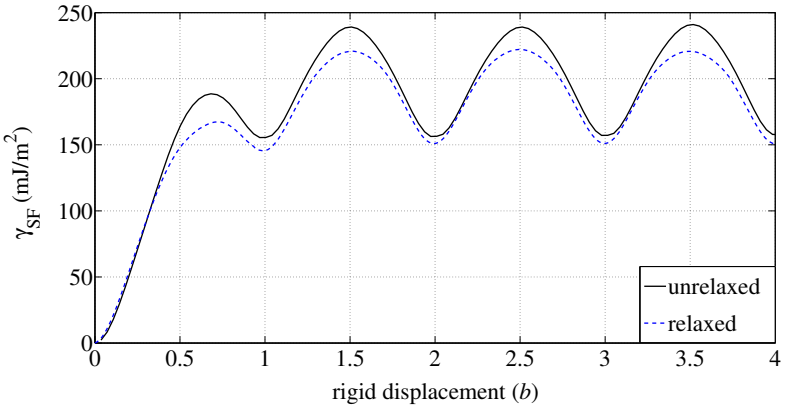


Figure 2.9: γ_{SF} from (2.1) as a function of rigid displacement in the y ($[11\bar{2}]$) direction for Al with and without relaxation in z direction at 0 K.

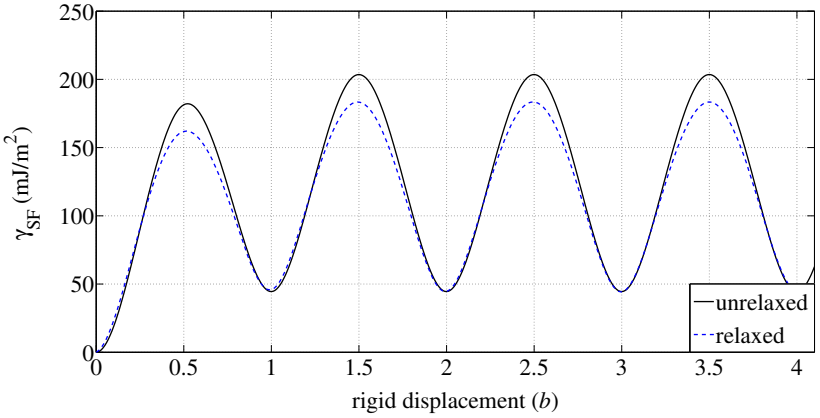


Figure 2.10: γ_{SF} from (2.1) as a function of rigid displacement in the y ($[11\bar{2}]$) direction for Cu with and without relaxation in z direction at 0 K.

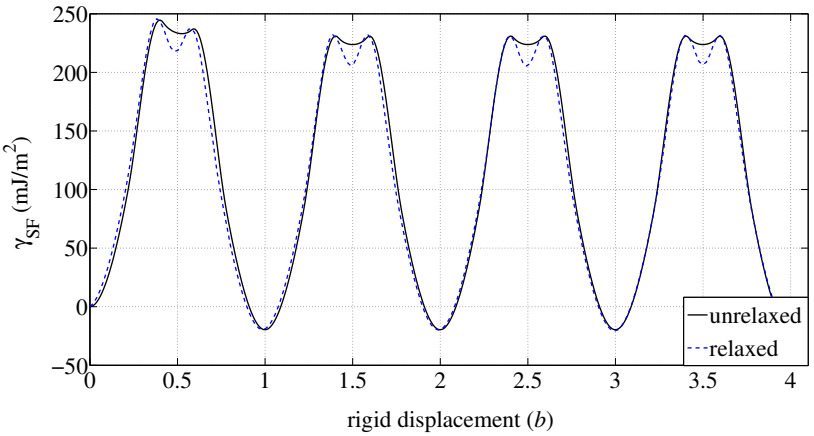


Figure 2.11: γ_{SF} from (2.1) as a function of rigid displacement in the y ($[11\bar{2}]$) direction for fcc Fe with and without relaxation in z direction at 0 K.

free energy calculations, we limit ourself to the intrinsic stacking fault at $b = 1$.

The fact that the stable SFE values (γ_{ISF}, γ_{ESF} and γ_{TSF}) for fcc Fe at 0 K in Table 2.1 are negative is related to the instability of fcc iron at 0 K. In other words, based on the ABOP of Müller et al. (2007), the hcp form of pure Fe is more stable than fcc at 0 K. Negative values for SFE at 0 K are also obtained in DFT calculations for non-magnetic Fe (Körmann et al. (2012)). Magnetic and other effects related to additional electronic contributions to the SFE of Fe are neglected in the current approach. It should also be noted that the small drops in the energy curves in Figure 2.11 at the location of the maximum energy is only restricted to Fe with ABOP. Since this is not seen in DFT calculations, it is most probably due to the potential itself. Such local minima are not seen for cases of Cu and Al with EA potential.

At finite temperature, the relation

$$\gamma_{\mathrm{SF}} = \frac{G_{\mathrm{f}}/N_{\mathrm{f}} - G_{\mathrm{i}}/N_{\mathrm{i}}}{A_{\mathrm{f}}/N_{\mathrm{f}}} \tag{2.6}$$

for the SFFE replaces the internal-energy-based relation in (2.1). Figure 2.12 shows the SFFE of fcc iron as a function of temperature for two different considered sizes. As shown, the SFFE of Fe is negative at low temperature but increases with increasing temperature as the fcc phase becomes more and more stable. Depending on the system size, it becomes positive between 230 K (smaller system) and 200 K (larger system), respectively. At this point, the surrounding fcc lattice of Fe has become more stable than the SF layer. At room temperature (293 K), the SFFE has increased to between 5.5 (smaller system) and 9.1 mJ/m^2 (larger system).

The fact that the SFFE of fcc Fe calculated by ABOP at room temperature is positive and it is in same order of magnitude as most of the austenitic and TWIP steels, makes this potential an excellent choice for dislocation and twinning dynamics simulations at high temperatures in fcc phase of iron.

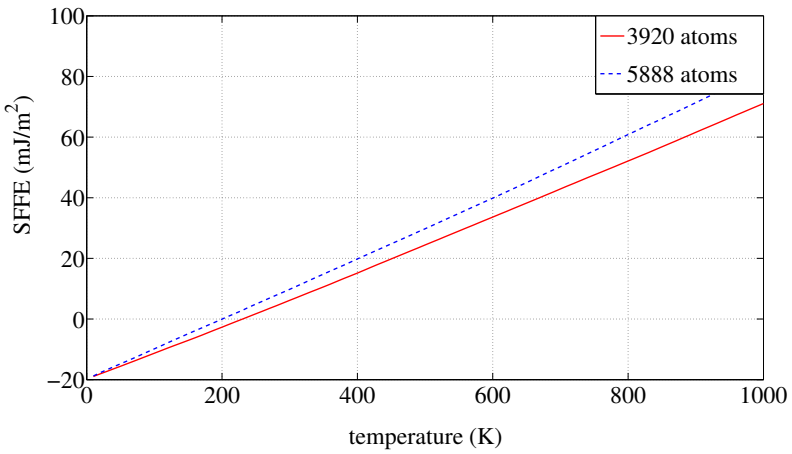


Figure 2.12: γ_{SF} from (2.6) of fcc Fe as a function of temperature.

2.6 Conclusion

Stacking fault energy (SFE) of Al, Cu and fcc Fe are calculated using conventional rigid displacement method. The values resulted for Cu and Al are close to the values reported in the literature. However, for Fe, the SFE is negative which indicates the instability of the fcc Fe phase at zero K. In order to calculate the SFE of iron at higher temperatures, where fcc phase is stable, it is necessary to calculate the stacking fault free energy (SFFE). To reach this goal, quasi-harmonic approximation (QHA) together with thermodynamic integration (TI) is employed. As expected, the results show that by increasing the temperature, the SFFE increases and at around 200 K the value of SFFE become positive. The value of SFFE at room temperature is 5.5 and 9.1 mJ/m^2 for two different system sizes studied in this work.

CHAPTER 3

STRAIGHT DISLOCATION-STACKING FAULT INTERACTION*

"Louis Pasteur's theory of germs is ridiculous fiction."
-Pierre Pachet, professor of physiology at Toulouse, 1872

3.1 Introduction

In a number of fcc materials such as copper or aluminum, as well as more complex materials such as high magnanese steels exhibiting so-called twinning-induced plasticity (i.e., TWIP steels), the interaction between dislocations and other defects such as stacking faults (SFs) or twins plays an important role in their deformation behavior. Depending on the particular material, the process, and the environment conditions, this interaction can lead to twinning or detwining, determining the dominant deformation mechanism. In the case of TWIP materials, for example, dislocation-twin interaction may inhibit dislocation movement and result in significantly higher strength and hardening (e.g., Bouaziz et al. 2011).

Among the methods used to gain insight into the nature of such interactions at the atomic scale, molecular dynamics (MD) is one of the most common. For example, Jin et al. (2006) studied the interaction between screw dislocations and coherent twin boundaries in Al, Cu and Ni. In their partially periodic approach, a perfect screw dislocation is created at the edge of the simulation supercell and driven toward the twin boundary via the imposition of a constant shear strain on the supercell, in the process dissociating into two partial dislocations and a SF. Jin et al. (2006) identified two scenarios for dislocation-twin boundary interaction depending on the material type (stacking fault energy) and the shear strain. In the case of Al,

*This chapter is based on the work in Mianroodi & Svendsen (2016*b*)

for example, regardless of the applied shear strain, the partials reach the twin boundary and are absorbed by it in the sense that they continue their motion along it in opposite directions. On the other hand, in the case of Cu and Ni, the partials penetrate the twin boundary and move into the twinned region of the material, i.e., above a certain critical level of imposed shear strain (1.0-1.1% for Cu and 0.4-0.5% for Ni). In another study, Jin et al. (2008) investigated the interaction between non-screw dislocations and a coherent twin boundary. In this study, the initial dislocation is a 60° mixed edge-screw type which is again driven toward the twin boundary by a constant shear strain.

More recently, Sangid et al. (2011) and Ezaz et al. (2011) investigated energy barriers for slip transmission at different boundaries in Ni and Cu including coherent twin boundaries. In their modeling, dislocations are nucleated from a small void in the simulation supercell and then driven toward the boundary via an imposed tensile load. Since their model is fully periodic, bulk stress state conditions are achieved in the simulation. On the other hand, dislocation nucleation at the void is not controllable; the loading process generates a complex tangle of dislocation loops all moving toward the twin layer. Hence, it is not possible to study individual or single dislocation-dislocation and dislocation-twin interactions independent of other influencing factors in this fashion (this was of course not the purpose of the authors in their study).

In another recent work, Wei & Wei (2012) investigated the interactions between screw dislocation and SFs in different fcc metals using a partially periodic approach similar to that of Jin et al. (2006). As in this earlier work, only one dislocation is interacting with the SF. Depending again on the material and loading conditions, they observed three interaction types: annihilation, penetration, and growth, of the SF. For Al, dislocation-SF interaction always leads to SF annihilation, while for Au this always results in SF growth; for example, the transformation of an intrinsic stacking fault (ISF) to an extrinsic stacking fault (ESF), or an ESF into a twinning stacking fault. Whether or not this interaction results in annihilation or penetration of the SF in Ni, Cu and Ag depends on the magnitude of the imposed shear strain driving dislocation motion.

The models used by Jin et al. (2006) and Wei & Wei (2012) are periodic in one direction and bounded in the other two directions. In addition, (screw) dislocation motion is driven in these models by a constant imposed shear strain, resulting in a variable shear stress and driving force on the dislocation. The purpose of the current work is to develop and apply an alternative, fully periodic MD-based modeling approach to dislocation motion and interactions. Being fully periodic, boundary influences of any kind on the stress state are eliminated, and true bulk conditions are achieved. Given such modeling, dislocation motion can be driven by a controlled stress, and all stress components can be controlled independently. This facilitates the investigation of dislocation interactions under complex loading cases as well as at finite temperatures with respect to a controllable driving force.

3.2 Modeling approaches

The purpose of this section is to introduce and explain the partially and fully periodic modeling approaches to dislocation-stacking fault interaction in detail. As an example of the former, in the first section we focus in particular on the work of Wei & Wei (2012) which is a partially periodic and strain-controlled simulation. In the next two sections, we describe alternative methods for fully periodic and stress controlled modeling of dislocation-SF interaction.

3.2.1 Partially periodic strain-controlled modeling

The supercell for this case is constructed as shown in Figure 3.1. It contains 144000 atoms and has

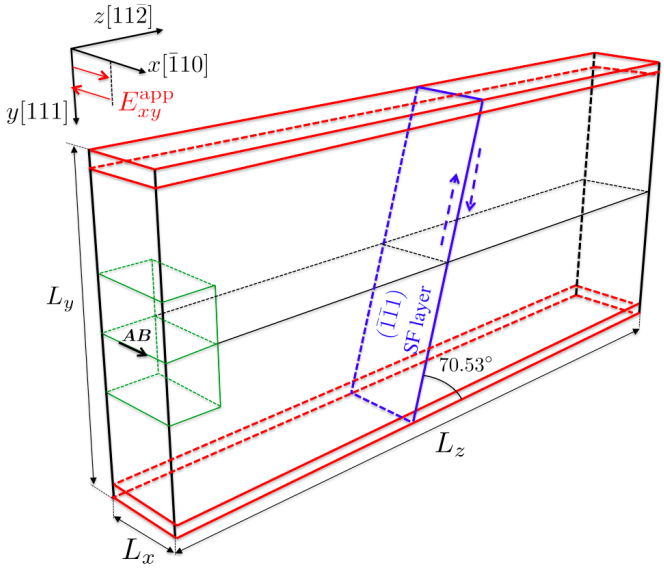


Figure 3.1: Supercell for partially periodic dislocation-SF interaction modeling from Wei & Wei (2012) (see also Jin et al. 2006). This cell is periodic in x direction and bounded in the y and z directions. See text for details.

dimensions $(L_x, L_y, L_z) = (3\sqrt{2}, 40\sqrt{3}, 50\sqrt{6})\, a_0$, where a_0 is the lattice constant ($3.615\mathring{A}$ for Cu and $4.050\mathring{A}$ for Al). The SF (outlined in blue, Figure 3.1) is created via rigid displacement of the two halves of the supercell with respect to each other by an amount $\sqrt{6}\, a_0/6$ parallel to the blue dashed arrows in Figure 3.1. Applying this amount of displacement creates ISF in the simulation box. The same cut and displace method is used to create ESF and twin layers in this work. After SF creation, supercell equilibrium is (re)established via static energy minimization and supercell relaxation in the x direction followed by dynamic relaxation in 5000 MD (time) steps assuming NVE conditions and velocity rescaling to 0.1K. The time step size is 2 fs.

After insertion of the SF and the relaxation, the leading and trailing partials of the screw dislocation are created via displacement of the boundary region of the supercell shown in green on the left side in Figure 3.1. Considering the Thomson tetrahedra (e.g., Hirth & Lothe 1982, Figures 10-9, 10-10), $\mathbf{AB} = \frac{1}{2}[\bar{1}10]$ and

$$\begin{array}{ccccc} \mathbf{AB} & = & \mathbf{A\delta} & + & \boldsymbol{\delta}\mathbf{B} \\ \frac{1}{2}[\bar{1}10] & = & \frac{1}{6}[\bar{1}2\bar{1}] & + & \frac{1}{6}[\bar{2}11] \end{array} \tag{3.1}$$

where $\boldsymbol{A\delta}$ and $\boldsymbol{\delta B}$ are the leading and trailing partials, respectively. To create the leading partial, the lower part of the green region on the left side in Figure 3.1 is displaced parallel to the (x, z) plane by an amount $\frac{1}{4}a_0(\sqrt{2}/2, \sqrt{6}/6)$, and the upper part by the opposite amount, in 5000 MD steps. The trailing partial is created in an analogous fashion during a second 5000 MD steps and the displacement of $\frac{1}{4}a_0(\sqrt{2}/2, -\sqrt{6}/6)$ for the lower part. The total displacement after creation of the leading and trailing partials is then $\frac{1}{2}a_0[\bar{1}10]$, representing the Burgers vector of a perfect screw dislocation, $\boldsymbol{AB}$.

Finally, as shown in Figure 3.1, the shear strain E_{xy} is applied to the whole model using ramp displacement of all atoms. One layer of atoms in the top and the bottom of the model is fixed in x and z directions to maintain this strain; on the other hand, they are free to move in y direction. After applying this shear strain, the main simulation is carried out for 15,000 to 30,000 MD steps, depending on the level of shear strain. Velocity rescaling for temperature control is turned off during this phase since it could affect the interaction.

3.2.2 Fully periodic stress-controlled modeling with finite-length stacking fault

The supercell for this case is shown in Figure 3.2. The system size and lattice orientation are the same

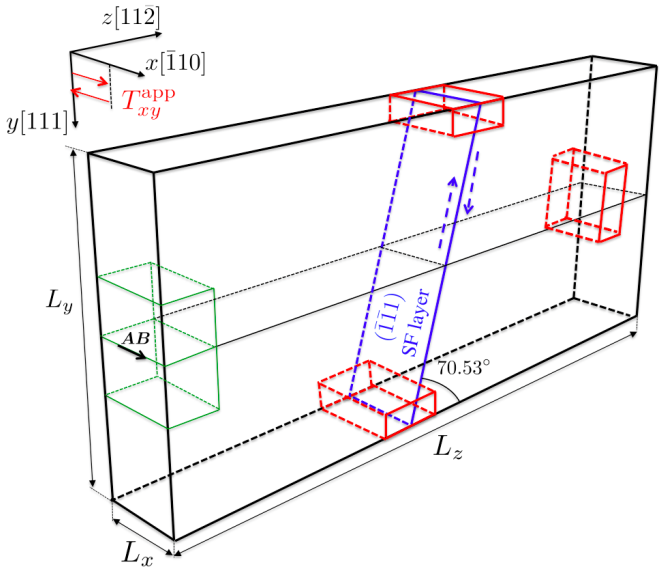


Figure 3.2: Supercell for fully periodic dislocation-SF interaction modeling with finite SF layer size. See text for details.

as in the pervious partially periodic case with the difference that now the box is periodic in all directions. Furthuremore, the simulation box is non-orthogonal in order to compensate for internal stresses produced by dislocations (e.g., Bulatov & Cai 2006, Chapter 5) and also giving the possibility to control the shear stress components during the simulation through Parrinello-Rahman algorithm (Parrinello & Rahman 1981). In addition, since the supercell is now also periodic in the y direction, application of the rigid displacement along the dashed lines shown in Figure 3.2 to create the SF results in some atomic overlap. This is eliminated via static energy minimization together with supercell relaxation in the all directions. After this step, two small regions of atoms at the two ends of the SF (shown in red in Figure 3.2) are fixed in the x and z directions in order to stabiize it. In fact, they act as a type of additional defect keeping the (metastable) SF extended beyond its equilibrium length. Indeed, if this is not done, the SF shortens during dynamic relaxation to its equilibrium length. In the previous partially periodic modeling, stabilization of the SF length in this sense is achieved by its attachment to the free surface. After stabilizing the SF in this fashion, dynamic relaxation is carried out for 5000 MD steps under NPT conditions using a Nose-Hoover chain thermostat and barostat. As before, the damping coefficients for the thermostat and barostat are set

to 200 and 2000 times the time step size, respectively. In particular, all stress components (including the shear components) are set to zero. The resulting SF shown in cross-section in Figure 3.3 is fully periodic and stress-free. It should be noted that, although resulting model is periodic, the length of the SF is not

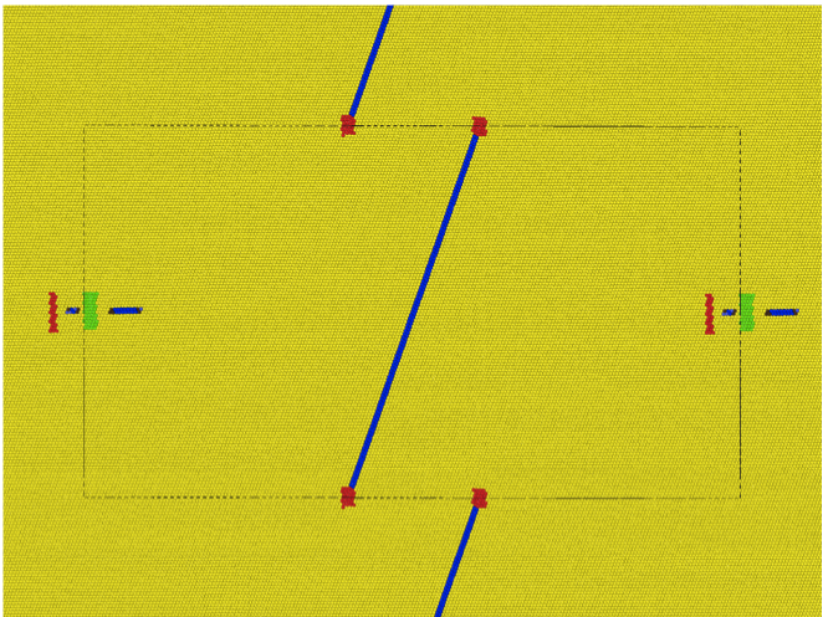


Figure 3.3: Fully periodic model configuration for dislocation-SF interaction modeling with finite SF layer size. Color-coded regions here include (i) fcc (yellow), (ii) stacking fault (blue), (iii) dislocation core (brown), (iv) fixed atoms (red), (v) dislocation nucleation (green). Local atomic coordination is determined via common neighbor analysis using OVITO visualization tool (Stukowski 2010).

infinite. Rather, a periodic array of SFs is obtained. As such, the dislocation interacts with an array of finite-length SFs.

Dislocation partials are created in a same way as discussed above; in the current case, however, this results in a dislocation dipole. To prevent the motion of both monopoles toward the SF upon loading, a barrier (red region to the right of the SF in Figure 3.2) is placed between the one monopole and the SF sufficiently far from the dislocation-SF interaction point to have negligible influence on the interaction. The barrier is a small region of atoms fixed in x and z directions (red region on the right side of the simulation box in Figure 3.3).

The last step involves shear loading of the cell. To this end, the shear strain corresponding to the desired shear stress is applied to the simulation supercell in one step. To obtain better starting values for the stress-controlled simulation, the value of this strain is estimated using the shear modulus and the desired constant shear stress. Given this initial condition, the MD simulation is run under NPT conditions with all stress components set to zero except xy shear stress which is set to the desired value T_{xy}^{app}. Depending on the applied stress and the resulting dislocation velocity, the simulation time required for the interaction varies between 10,000 to 30,000 MD time steps.

As it is seen in Figure 3.3, the two ends of the SF are far away from the dislocation-SF interaction point (i.e., in the middle). However, the long range nature of the stress fields of the dislocations at the two ends of the SF layer could affect the interaction. Based on the system size, the amount of stress generated by

these partials at the interaction point is in order of 200 MPa which is comparable to the lowest applied shear stress T_{xy}^{app}. In order to have a better characterization of interactions, it is useful to make the model as simple as possible and remove all the possible influencing effects. Thus, the next section describes a model in which the SF has an infinite length therefore there is no SF end effect on the interaction.

3.2.3 Fully periodic stress-controlled modeling with infinite stacking fault

In the modeling approach just discussed, the dislocation interacts with an infinite array of finite-length stacking faults. For comparison, it is interesting to compare this with the second approach in which the dislocation interacts a single infinite stacking fault. Figure 3.4 shows the supercell for this case. Compared to the finite-length array of SFs in Figure 3.2, here, the SF plane and dislocation glide place have been replaced with each other, aligning the fault in xz plane resulting an infinitely large SF.

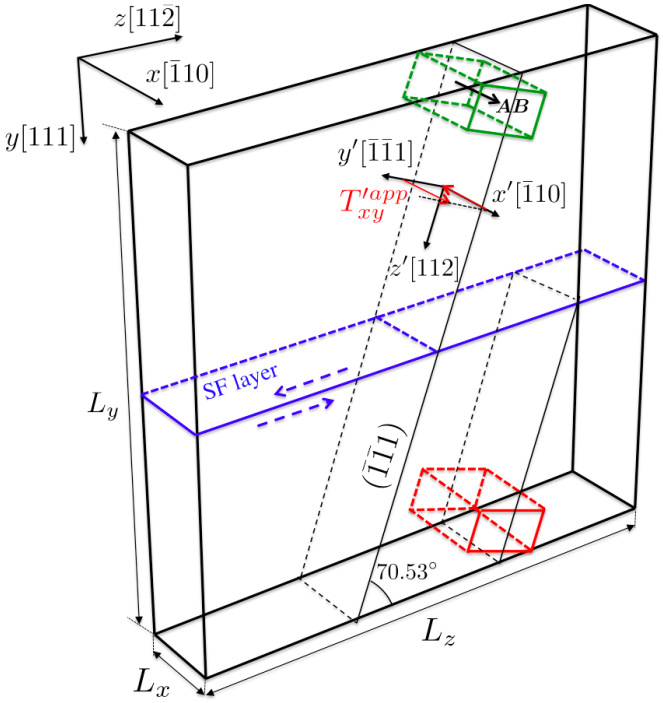


Figure 3.4: Supercell for fully periodic dislocation-SF interaction modeling with infinite SF layer. See text for details.

The advantage of this model is that the SF is infinite and it is not bounded by two fixed partial dislocations at its two ends like the previous modeling case. This will remove any unwanted effect on interaction due to the stress field of the partials at the SF ends. However, since the dislocation glide direction is not aligned with the box axis, simple shear stress on dislocation $T_{xy}^{'app}$ in $x'y'z'$ system should be rotated back to the box coordination system xyz in order to have the same stress state on the dislocation as the previous modeling case. Box dimension in x is same as previous while $(L_y, L_z) = (200\sqrt{3}/3, 30\sqrt{6})\, a_0$. All the other simulation details are the same as the case with infinite array of finite-length stacking faults. Figure 3.5 shows the atomic structure of the discussed model with infinity large stacking fault.

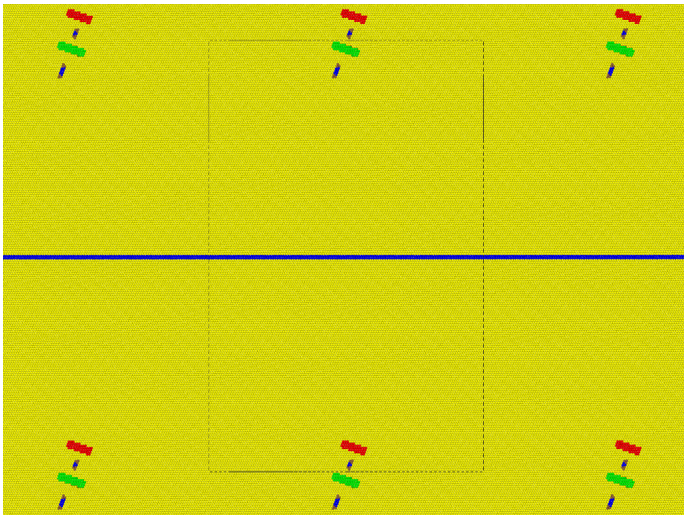


Figure 3.5: Fully periodic model configuration for dislocation-SF interaction modeling with infinite SF layer. Color coding is same as in Figure 3.3

3.3 Periodic continuum & MD modeling of dislocation displacement field

Using continuum theory (e.g., Bulatov & Cai 2006, Chapter 5), the displacement field u_x^{per} around a screw dislocation dipole oriented in the x direction in a periodic supercell can be written as a sum of the displacement field generated by one dipole in infinite medium u_x^{∞} and that generated by all its periodic images, i.e.,

$$u_x^{\text{per}}(\boldsymbol{r}) = u_x^{\infty}(\boldsymbol{r}) + \sum_{a=1}^{\infty} u_x^{\infty}(\boldsymbol{r} - \boldsymbol{r}_a) \,, \tag{3.2}$$

where $\boldsymbol{r}_a$ represents the location of the periodic images. Truncation of this sum to its first N terms results in an error

$$u_x^{\text{per}}(\boldsymbol{r}) = u_x^{\infty}(\boldsymbol{r}) + \sum_{a=1}^{N} u_x^{\infty}(\boldsymbol{r} - \boldsymbol{r}_a) + u_x^{\text{err}}(\boldsymbol{r}) \,, \tag{3.3}$$

where u_x^{err} is linear and can be determined by comparing u_x at three corners of the supercell. Insertion of the dislocation results in a strain with components

$$\begin{array}{rcl} E_{xy} & = & \frac{1}{2\Omega}(b_x a_y + b_y a_x) \,, \\ E_{xz} & = & \frac{1}{2\Omega}(b_x a_z + b_z a_x) \,, \\ E_{yz} & = & \frac{1}{2\Omega}(b_y a_z + b_z a_y) \,, \end{array} \tag{3.4}$$

where Ω is the supercell volume, $\boldsymbol{b} = (b_x \,, b_y \,, b_z)$ is the Burgers vector, and $\boldsymbol{a} = (a_x \,, a_y \,, a_z)$ is the area vector between two dislocations. In the case of finite SF (Figure 3.2), since the Burgers vector is in x direction and the area vector is in y direction, the only non-zero component of strain is E_{xy}.

As discussed by Bulatov & Cai (2006), in order to create a dislocation dipole in a periodic model, one can impose the displacement field (3.3) on the atoms. Since the current approach is based on NPT conditions with zero stress, the strain field it predicts should be comparable to (3.4). To show this, a

periodic supercell similar to the one shown in Figure 3.2 without the SF and the red fixed regions is considered. The dislocation dipole is created using the direct method described in Section 2.2 followed by the same relaxation procedure. At the end of the relaxation, the displacement field and also the shear strain generated by the dislocations are calculated and compared to the resulted ones from (3.3) and (3.4).

The MD- and continuum-based values of E_{xy} are 0.90% and 0.89%, respectively, and so in good agreement. From the point of view of the strain field, then, at least, these results confirm the equivalence of the method used in this work and the continuum-based method (e.g., Bulatov & Cai 2006, Chapter 5).

3.4 Results and discussion

3.4.1 Comparison of strain-controlled and stress-controlled modeling

To compare the partially and fully periodic modeling approaches just discussed, dislocation-SF interaction simulations have been carried out with each for Cu and Al. All simulations are based on Mishin EA potentials (Mishin et al. 1999, 2001) and have been run using the LAMMPS package Plimpton (1995). To begin, selected simulations from the work of Wei & Wei (2012) as based on partially periodic modeling and NVE conditions have been repeated. The corresponding results are compared in Table 3.1. Except

	Shear Strain (%)							
Material	0.5	0.6	0.7	1.2	1.3	1.6	1.7	1.8
Cu (Wei & Wei 2012)	-	-	A	A	A	A	P	P
Cu (this study)	-	A	A	A	P	P	P	P
Al (Wei & Wei 2012)	-	A	A	A	A	A	A	A
Al (this study)	-	A	A	A	A	A	A	A

Table 3.1: Partially periodic modeling results for the type of interaction (i.e., annihilation, penetration) of a screw dislocation with an intrinsic stacking fault under NVE conditions as a function of applied shear strain. A: annihilation mode of interaction, P: penetration mode of interaction See text for details.

for the different critical strain in Cu for the transition from annihilation to penetration, which can be explained by small differences in the realization of the initial conditions, the results are in good agreement. In particular, for Al regardless of the imposed shear strain, the interaction between the SF and the dislocation is always annihilation. Given the relatively large stacking fault energy (SFE) of Al, this is expected; any ISF should be intrinsically unstable. On the other hand, for a material like Cu with a lower SFE, the picture is more complicated. Indeed, below a certain strain (stress) level, the SF is also annihilated; above this, however, penetration takes place.

Consider next the history of shear stress T_{xy} acting on the partial dislocation for two different placements of the SF in the supercell shown in Figure 3.6. Because the stress on the dislocation is not controllable in the partially periodic context, it varies with time as shown. Since the interaction type depends on the magnitude of the driving stress, however, this results in an apparent dependence of interaction type on the initial separation of the dislocation and SF in the supercell. This is clearly shown by the two cases compared in Figure 3.6. The results in Table 3.1 and the stress history depicted by the blue solid curve in Figure 3.6 are for the case that the SF is positioned in the center of the supercell. If the SF is moved farther away from the dislocation starting point, however, the same applied shear strain E_{xy}^{app} of 1.4% results in annihilation and the stress history depicted by the red dashed curve in Figure 3.6. The reason is clear;

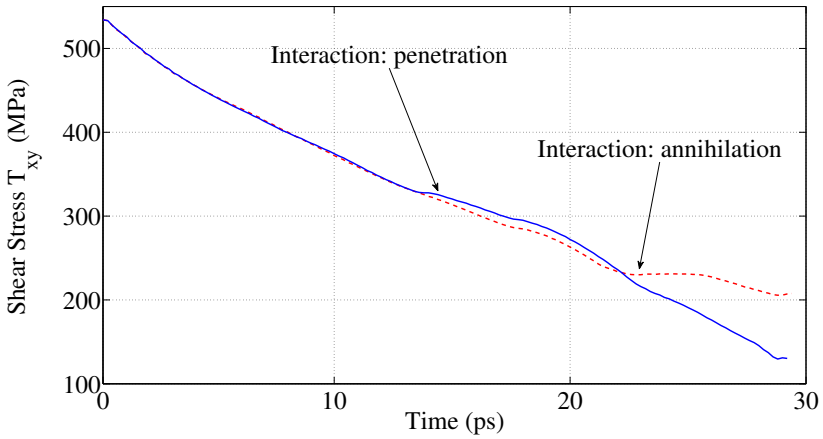


Figure 3.6: Shear stress as a function of time acting on the partial dislocation predicted by partially-periodic modeling under NVE conditions for an imposed shear strain E_{xy}^{app} of 1.4% and two different placements (center: blue solid curve; right: red dashed curve) of the SF in the supercell. The material here is Cu. See text for details.

because T_{xy} decreases with time and dislocation glide, the driving force is different in the two cases, resulting in different interactions. As shown in Figure 3.7, not only T_{xy}, but all other stress components, as well as the temperature, vary in these simulation. As such, these cannot be controlled or be varied

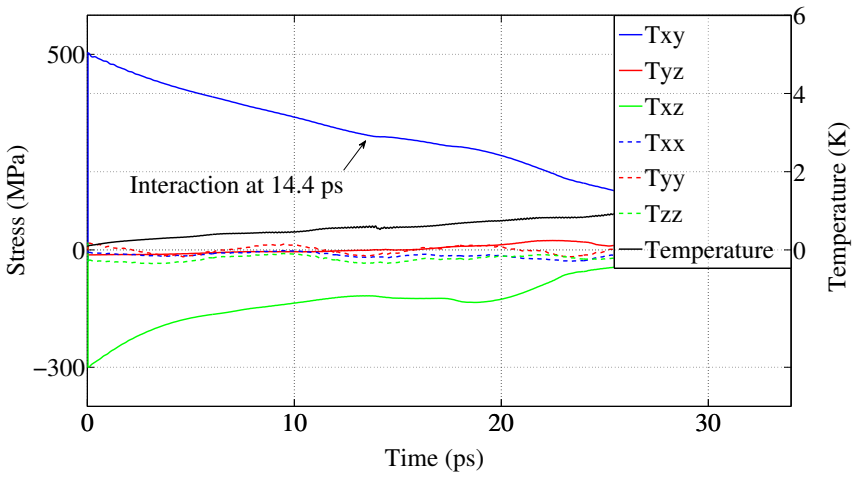


Figure 3.7: History of stress components and temperature in Cu predicted by partially periodic modeling of dislocation-SF interaction under NVE conditions for an imposed shear strain E_{xy}^{app} of 1.3%. The type of interaction here is penetration (Table 3.1).

independent of one another in the partially periodic case. This is in contrast to the current fully periodic modeling.

For the following discussion, the components

$$\begin{aligned} f_x &= 0\,, \\ f_y &= T_{xz}\, b_x\, \xi_x + T_{zz}\, b_z\, \xi_x\,, \\ f_z &= -T_{xy}\, b_x\, \xi_x - T_{yz}\, b_z\, \xi_x\,, \end{aligned} \tag{3.5}$$

of the Peach-Köhler force $\boldsymbol{f} = \boldsymbol{T}^{\mathrm{T}}\boldsymbol{b} \times \boldsymbol{\xi}$ (e.g., Hirth & Lothe 1982, Bulatov & Cai 2006, Chapter 10) for the dislocation configuration in Figure 3.2 are relevant (Peach & Koehler 1950) . Here, $(b_x, 0, b_z)$ and $(\xi_x, 0, 0)$ represent the components of the Burger vector and line orientation, respectively, in the current case. Of these, f_z drives dislocation glide, and f_y is perpendicular to the glide plane (Figure 3.2). Consider for example the case of zero normal stresses and zero normal strains (and so no volume change). In this case,

$$f_y = T_{xz}\, b_x\, \xi_x\,, \quad f_z = -T_{xy}\, b_x\, \xi_x\,, \tag{3.6}$$

are then the non-trivial components of the Peach-Köhler force from (3.5). Note that these imply that $f_y/f_z = -T_{xz}/T_{xy}$ depends only on the remaining shear stresses. With these choices, four of six bulk degrees of freedom have been fixed, and two remain to be controlled for bulk behavior. Again, each of these further choices will lead to different dislocation-SF interactions in general. Although investigating the interaction behavior under different stress states is an interesting topic, here we limit our study to the simplest case where the only non-zero force on the dislocation is the force on the glide direction f_z. Thus, as mentioned before, in the stress controlled simulations, all the stress components are set to zero expect T_{xy} resulting f_z (T'_{xy} and f'_z for infinite SF model in Figure 3.4). In this case for example, one obtains the history of stress and temperature shown in Figure 3.8. Compared to Figure 3.7, this clearly explains the advantage of periodic modeling together with stress controlling in terms of having a simpler stress state. In the next section, the results of two different stress controlled periodic modelings, one with array of finite SF layers and one with infinite SF layer, are compared together.

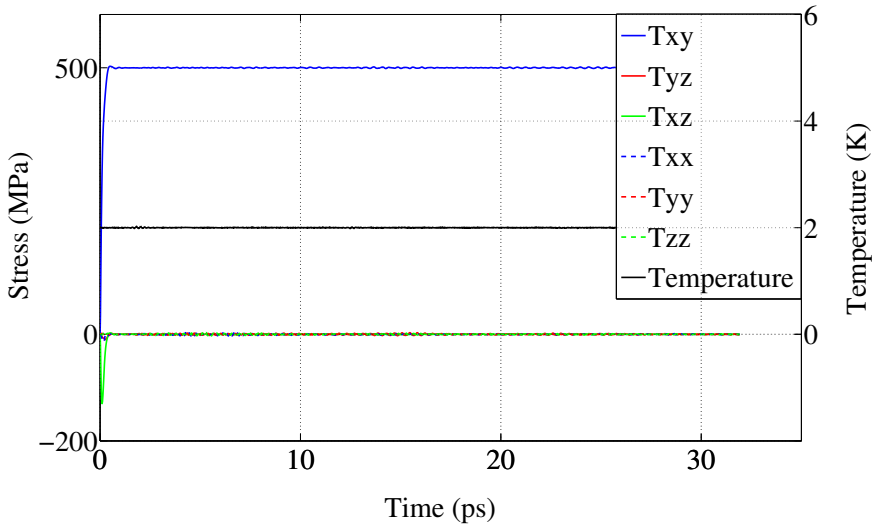


Figure 3.8: History of stress components and temperature in Cu predicted by fully periodic modeling of dislocation-SF array interaction under NPT conditions for an imposed shear stress T_{xy}^{app} of 500 MPa at a temperature of 2 K. The type of interaction here is growth (Table 3.2). See text for details.

3.4.2 Comparison of finite SF and infinite SF modelings

Following the modeling description in sections 2.2 and 2.3, for a range of T_{xy}^{app} values, one obtains the dislocation-ISF interaction result summarized in Table 3.2 for the case of finite and infinite SF layers.

	Shear stress (MPa)						
Material / Case	100	200	300	400	500	600	700
Cu / SF array	-	G	G	G	G	G	G
Cu / Inf. SF	-	A	P	P	P	P	P
Al / SF array	-	A	A	A	A	A	A
Al / Inf. SF	-	A	A	A	A	A	A

Table 3.2: Fully periodic modeling results for the type of interaction between a screw dislocation and an intrinsic stacking fault under NPT conditions as a function of applied shear stress T_{xy}^{app} ($T_{xy}^{'}$ for infinite SF case). The temperature is fixed at 2 K using the Nose-Hoover thermostat. A: annihilation mode of interaction, P: penetration mode of interaction, G: growth mode of interaction

In the case of Al, the interaction for all stress ranges is annihilation, same as the partially periodic modeling in Table 3.1. Although the stress state of the system is different, it seems that for Al, the large SFE (145.9 mJ/m^2 compared to 44.3 mJ/m^2 for Cu) leads to a highly unstable SF which will be annihilated in all cases regardless of the stress state of the system. The difference in the results of infinite array case and the single infinitely large SF shows that the stress field created by the partials at the two ends of SF in the case of finite SF layer indeed has an effect on the interactions. Again, since we want to investigate the simplest case, it is better to focus on the infinite SF case where the internal stress field is simpler than the case of finite SF layer. However, it should be noted that in real materials we always have finite SF layers possibly with the same edge effects here as the case of finite SF layer. However, to gain a better understanding of the underlying interaction mechanism, it is necessary to make the model as simple as possible. Thus, in the next section, the infinite SF model is used for investigating and interpreting the dislocation interaction with other types of SFs.

3.4.3 Dislocation-SF interaction in different SF types

Table 3.3 shows the results of dislocation-SF layer in Cu for different SF layer types using the periodic infinite SF modeling. As it is seen, expect the intrinsic case, the interaction mode is same for all other SF types.

	Shear Stress (MPa)						
SF type	100	200	300	400	500	600	700
ISF	-	A	P	P	P	P	P
ESF	-	P	G	G	G	G	G
3SF	-	P	G	G	G	G	G
4SF	-	P	G	G	G	G	G

Table 3.3: Interaction modes between dislocation and different stacking faults as a function of shear stress $T_{xy}^{'}$ on the dislocation. Other conditions are same as Table 3.2. ISF: intrinsic stacking fault, ESF: extrinsic stacking fault, 3SF: 3 layer stacking fault (twin), 4SF: 4 layer stacking fault (twin)

One common behavior in all the interactions is that the two partials always recombine together at the SF layer to form perfect dislocation and then the interaction will take place. In other words, the partial dislocations will not interact with the SF alone as it is seen in Figure 3.9.

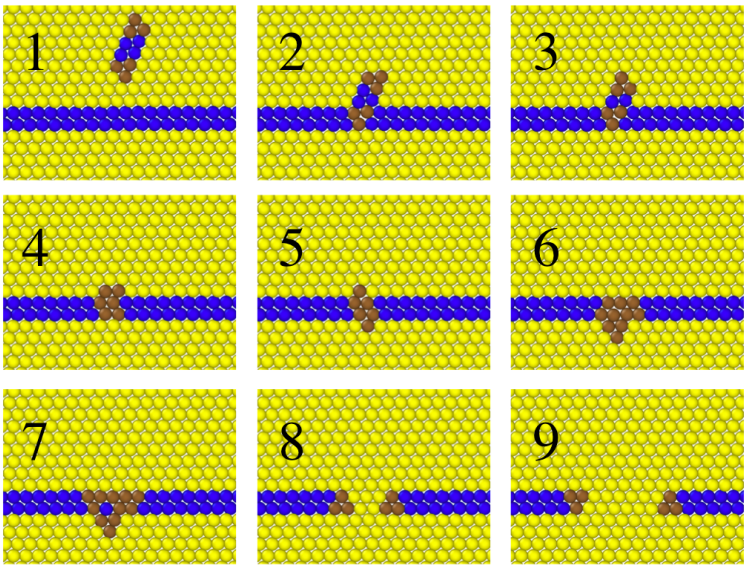


Figure 3.9: Snap shots of annihilation mode of interaction shows recombination of partials at the stacking fault and cross-slip of the perfect dislocation followed by dissociation on new glide plane. Color coding is same as Figure 3.3.

Using crystal analysis tool (CAT) (Stukowski et al. 2012), it is possible to extract the burger vectors and dislocation line during the interaction. The output of such analysis is shown in Figure 3.10.

Considering these burger vector analysis, it is concluded that at first stage of interaction, partials recombine together at the SF layer and form a perfect screw dislocation. Then this perfect dislocation depending on the loading conditions, will either dissociates into two partials at the other side of the SF (penetration) or dissociates in the SF plane (annihilation or growth). The fact that the two partials always form a perfect before the interaction, even in the case of penetration, can be related to the geometrical mismatch between two sides of the SF layer. Due to this mismatch, dislocation needs to undergo one plane shift when it passes through the dislocation. The partials cannot jump to the other side alone since they have both edge and screw components and as we know, cross slip is hard to initiate in edge dislocations. Due to this, the leading partial will be blocked at the SF layer until the trailing one reaches and they form a perfect dislocation. At this point, since the screw dislocation could cross slip more easily, it can jump to the other side and do the one layer shift. If this happens, then the interaction mode is penetration and after the perfect dislocation made it to the other side of the SF, it will again dissociate to partials as they continue the glide. The dislocation reaction for this case is:

$$\boldsymbol{A\delta} + \boldsymbol{\delta B} \xrightarrow{\text{combination at SF}} \boldsymbol{AB} \xrightarrow{\text{dissociation at other side}} \boldsymbol{A\delta} + \boldsymbol{\delta B}\ , \tag{3.7}$$

As we saw in the results, penetration is not always the case. The perfect screw dislocation formed at the SF layer, sometimes decides to change the glide plane to the SF habitat plane. In this case, it will

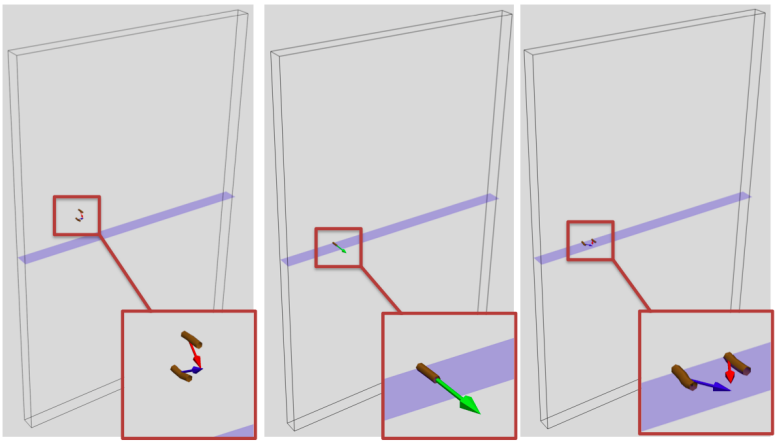


Figure 3.10: Three snapshots of dislocation configuration and Burgers vector during annihilation mode of interaction using CAT analysis tool and ParaView (Henderson 2007). Purple layer is SF, brown is dislocation line segment, blue and red vectors are partial dislocations Burgers vector and green vector is the Burger vector of perfect screw dislocation

dissociate into partials in the SF plane. This is same for both annihilation and growth modes of interaction with the following dislocation reaction:

$$\boldsymbol{A\delta} + \boldsymbol{\delta B} \xrightarrow{\text{combination at SF}} \boldsymbol{AB} \xrightarrow{\text{dissociation on SF plane}} \boldsymbol{A\gamma} + \boldsymbol{\gamma B}\,, \tag{3.8}$$

As it is seen in Figure 3.11, the only difference between annihilation and growth interaction modes is that the dissociation plane is different in these two cases. If the perfect dislocation dissociates in the exactly

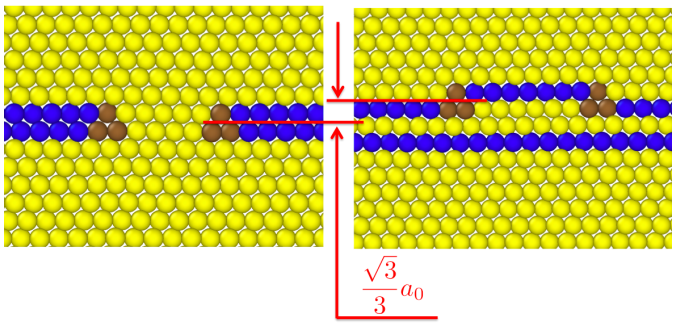


Figure 3.11: Zoomed view of annihilation and growth modes of interaction showing the different planes at which the perfect dislocation has dissociated. The color coding is same as Figure 3.3

same atomic plane as the center of SF layer, then the interaction mode is annihilation. However, if it dissociates in the immediate adjacent plane to the center of SF layer, then the growing will take place. Although these atomic planes are adjacent to each other, due to SF layer, a huge stress concentration is available at these planes. This stress concentration is calculated and shown in Figures 3.12 and 3.13.

Whether the perfect dislocation dissociates in the center on SF layer or in the neighboring layer, depends

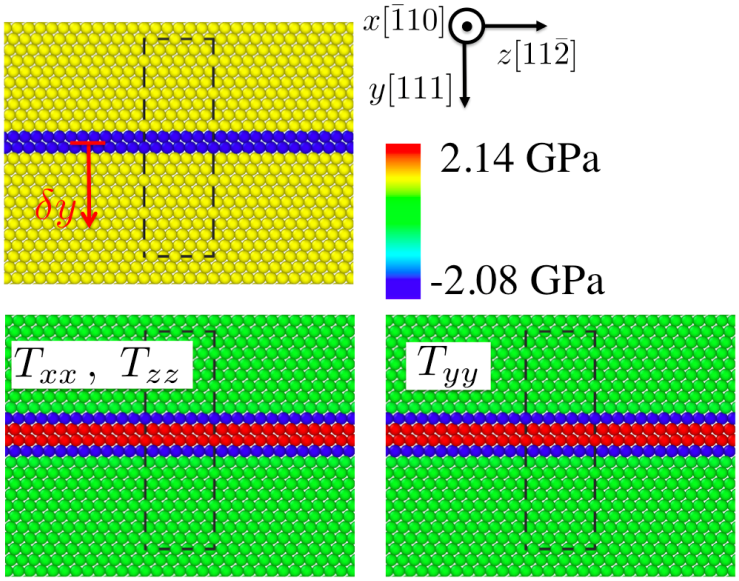


Figure 3.12: Stress contour around an ISF layer with the orientation shown.

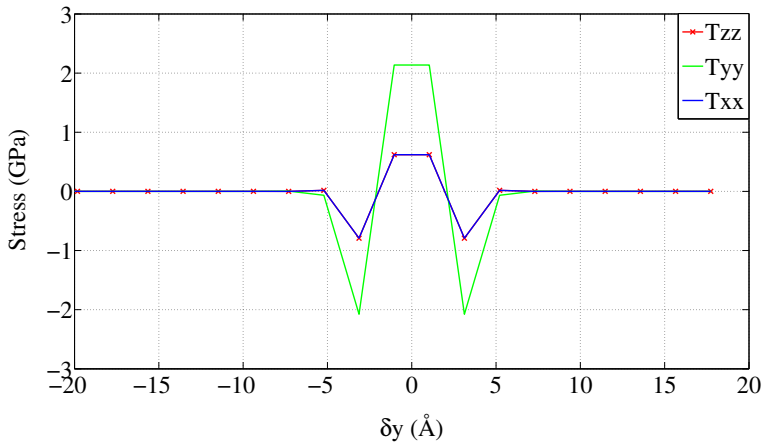


Figure 3.13: Stress jumps around SF layer as function of distance from center of SF layer, δy (see Figure 3.12)

on the external loading as well as the localized stress field of the SF itself resulting the annihilation or growth modes of interactions. Although a clear relation between these localized stress field from SF, external loading and the perfect dislocation core's decision at the SF to dissociate on different planes, leading to different interaction modes, is hard to maintain, it is logical to consider the stress field of SF as one of the influencing factors, especially since the one atomic plane offset between annihilation and growth modes of interactions as shown in Figures 3.11 is closely similar to the huge stress jumps around SF at one atomic layer adjacent to SF (Figure 3.12).

3.4.4 Effect of interaction on material behavior

It is possible to calculate the box deformation during the simulation as a function of time. Doing so for the cases with different interaction modes, it is possible to investigate directly the effect of dislocation-SF interaction on mechanical behavior of the material. For this purpose, strain evolution curves for three different interaction modes (penetration, annihilation and growth) are compared in Figure 3.14. These are calculated using the infinite SF layer model and the strain values are in the global xyz coordination system. As it is seen from this figure, in the case of penetration, due to nearly uninterrupted dislocation

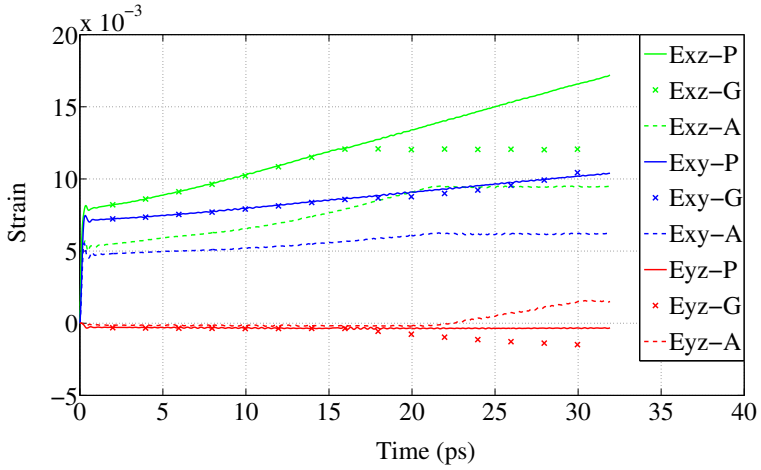


Figure 3.14: Evolution of three non-zero strain components during simulation time for different interaction modes compared together showing the strong effect of interaction on deformation

glide, the stress evolution is same during the whole simulation time. However, when growth or annihilation takes place, we see a sudden change in the curve slope. This is due to dislocation redirection in SF layer. For example, at 15 ps, interaction in one case leads to growing of the SF layer and as it is seen in Figure 3.14, this prevents E_{xz} to further develop as it does in the penetration mode. This could cause hardening in material.

3.5 Conclusion

The purpose of the current work is the development of a method for the modeling of dislocation processes based on 3d-periodicity capable of realizing arbitrary stress states and temperatures in a truly bulk fashion. A detailed comparison with an existing partially periodic approach in the context of the simulation of the dislocation-SF interaction demonstrates clearly the importance of this in the characterization and prediction of the corresponding interaction type. Indeed, as it is shown here, by being able to control the relevant physical quantity, i.e., the driving shear stress, independently in the simulation, interaction types can be more uniquely identified. Comparing two complete periodic models, one with finite length SF and other with infinitely large SF layer, it is concluded that the SF length effect is important and it is necessary to remove these effects by using the second model based on infinite SF. Using this infinite SF model under simple shear conditions, we have also studied the interaction modes for different SF layers including ISF, ESF, three layer and four layer twins. It is concluded that ISF will not grow to ESF under

one shear component loading, while under two shear components it will. for ESF and other types of SF layers, after a certain critical stress, the growing mode of interaction is always favored for Cu.

Studying the interaction with more detail revealed that at first the two partials recombine together at SF layer to form a perfect dislocation. After this, the perfect dislocation either dissociates on the same gliding plane on the other side of the SF (penetration mode) or it will dissociate on SF habitat plane (annihilation or growth modes). The Burgers vector reactions of these interaction scenarios are confirmed by regenerating dislocation lines and Burgers vector using CAT tool. Although the dislocation reaction seems to be same for both growth and annihilation modes of interaction, the reaction happens at two different planes. For annihilation, dissociation happens at the center of SF layer, while in the growth case, it happens at one atomic layer above or below SF.

Using molecular statics, the stress field around SF is calculated to be very localized with values changing between -2 to +2 GPa in just few atomic layers. The fact that the perfect dislocation core would dissociate in the center of SF layer (annihilation) or one layer besides SF (growth) could be related to this huge stress jumps across the SF layer. At this point, more detailed analysis of the interaction requires the dislocation core analysis under these circumstances which is out of scope of this work.

Strain evolution of the simulation box during the interactions, shows clear influence of the interaction type on deformation behavior which in turns shows the importance of such studies for understanding hardening behavior of material. As expected, penetration mode of interaction has a little effect on dislocation motion and facilitates the deformation while growth or annihilation redirects the dislocation into SF plane, preventing the deformation to continue in same way as before.

Since fully periodic modeling facilitates complete control of the stress components, it is also possible to investigate multiple interactions and more complex dislocation-SF configurations under controlled stress and temperature conditions. This represents work in progress to be reported on in the future.

CHAPTER 4

TWIN BOUNDARY MOTION AND JERKY FLOW*

"The Americans have need of the telephone, but we do not. We have plenty of messenger boys."
-Sir William Preece, Chief Engineer, British Post Office, 1878

4.1 Introduction

The existence of the twin boundaries believed to affect the dislocation motion and result in higher strain hardening. There are several molecular dynamic (MD) simulations describing such interactions of dislocations and twin boundaries. For example Jin et al. (2006) and Jin et al. (2008) studied interaction between screw and mixed dislocations with twin boundary in a number of fcc metals such as Al, Cu and Ni. They found that the dislocations either penetrate to the other side of the twin boundary or glide along the twin boundary depending on the details of the loading condition. Ezaz et al. (2011) calculated the energy barrier for slip transmission in dislocation-twin interaction in Cu using MD. Although most of these simulations are interesting and provide a lot of insight into the mechanisms of dislocation-twin interaction, they do not clearly show the effects of such interactions on the stress-strain behavior and the plasticity of the material.

Cheng & Ngan (2013) studied the stress-strain behavior of copper nano particles under collision. Based on their MD simulations, in the case of small particles and especially at higher loading rates, formation of twinning is the dominant plastic deformation mechanism while larger particles usually deform through dislocation glide. Sedlmayr et al. (2012) have investigated the twinning based deformation in Au nanowhiskers both with scanning electron microscopy and MD simulations. They have identified two

*This chapter is based on the work in Mianroodi, Azmi & Svendsen (2016)

types of twin formation in their samples, one with a large number small twins and other with one long twin, resulting two classes of stress-strain curves. The deformation mechanism based on a large number of twin formation results a continuous flow while in the case with one large twin, the stress flow is jerky with pronounced stress drops. According to Hu et al. (2009) migration of the twin boundary (causing twinning or detwinning) under shear loading depends on the angle of the shear direction relative to $[110]$ on (111) planes.

In this work, using MD simulations, we characterize the effect of external loading on the twin behavior as well as the stress-strain curves. To do this, we examine the stress-strain curves of different fcc configurations under all possible single component loading conditions. We report that in the presence of twin, in special loading directions, significant work hardening will be achieved while there is almost no work hardening observed for other loading cases. The stress-strain curve will also becomes jerky under some of the loading cases. The two main goals of this work are explaining the fundamentals of the observed work hardening and the jerky flow caused by the twin.

4.2 Simulation procedure

In order to study the effect of twinning on stress-strain curve, four sets of simulation boxes are setup as shown in Figure 4.1, bottom. First set is an ideal fcc box without any defect (Figure 4.1 bottom, left) which provides the base stress-strain curve and used to single out the effect of twinning in comparison to the second set including a twinned region (Figure 4.1 bottom, middle-left). Any difference in the results between these two boxes should be related to the twinned region in the second configuration. Figure 4.1 top shows the same twinned configuration with the fcc atoms not removed where mirroring feature of twinning is clear. The third and fourth configurations are similar to the first two ones. However, a void of 3 atoms is added in these boxes to facilitate nucleation of dislocations. In the third box (Figure 4.1 bottom, middle-right) the nucleated dislocations from the void will freely glide in the fcc matrix and often interact with each other while in the fourth configuration (Figure 4.1 bottom, right) all the dislocations gliding on planes not parallel to the twin boundaries will eventually interact with twin region. The comparison between third and fourth configurations will give us a picture about the effect of interactions of dislocations with twin boundary on the stress-strain curve.

All the simulation boxes are triclinic providing the freedom of applying six independent strain loadings, three normal and three shear loading cases. The box dimensions are approximately $20.4 \times 17.3 \times 25.0$ nm in x, y and z directions, respectively, containing about 748,800 atoms. Furthermore, x, y and z axis are parallel to $[\bar{1}\bar{1}0]$, $[\bar{1}\bar{1}2]$ and $[111]$ crystallographic orientations, respectively. In addition, periodic boundary condition is imposed in all three directions. The embedded atom (EA) potential for Cu, developed by Mishin et al. (2001) with lattice constant of 3.615 Å, is used for atomic interactions. As it is shown by Ezaz et al. (2011) and Boyer et al. (2004) this interatomic potential produces stacking fault energy (SFE) values close to density functional theory (DFT) calculations, making it a natural choice for twinning and dislocation simulations. We use LAMMPS molecular dynamic package (Plimpton (1995)) for MD simulations and Ovito (Stukowski (2010)) for visualizations and post processing.

Energy minimization is performed with conjugate gradient method, then the simulation box is relaxed at zero stress state (zero stress in all components) and 2 K with NPT ensemble during 5000 MD steps with time step size of 2 fs. Damping coefficients for thermostat and barostat are set to 100 and 1000 times the time step size, respectively. After relaxation, the mechanical loading is applied with constant strain rate of $5 \times 10^9 \mathrm{s}^{-1}$ using box deform command for about 40,000 to 60,000 MD steps under NVT ensemble

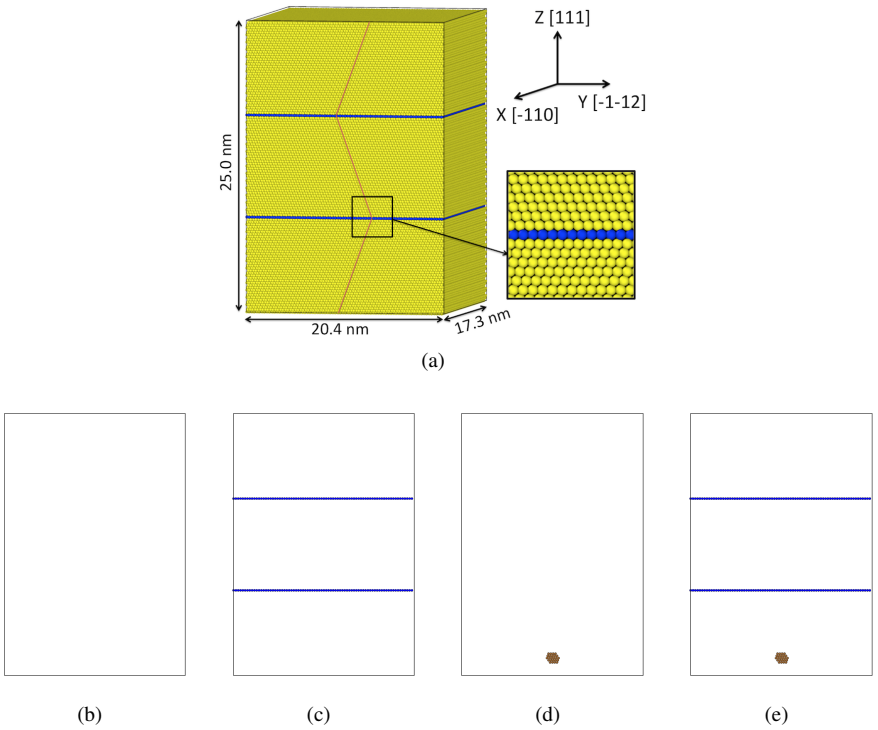


Figure 4.1: Different simulation boxes used to study effect of twinning on stress-strain curve. Color coding is based on CNA in Ovito (Stukowski 2010). Yellow: fcc atoms; blue: hcp stacking sequence corresponding to twin boundary; brown: unknown atomic structure, here corresponding to atoms at the void surface. Simulation box dimensions and orientation with twinned region is shown in top. In bottom row, fcc atoms are removed. Left: simulation box with single fcc crystal used as reference. Middle-Left: simulation box with twinned region in the middle (only twin boundaries are shown here). Middle-right: Sinle fcc crystal box with a void to facilitate discloation nucleation. Right: simulation box with the void and twinned region.

and temperature of 2 K with the same time step size as before. The stress response of the system is read using LAMMPS thermodynamic information and used to analyze and study effect of twinning.

4.3 Results and discussion

In this section, stress-strain curves resulted from the simulations described previously are presented and discussed. We have divided the section into tensile and shear loading cases.

4.3.1 Tensile loading

Figure 4.2 shows the flow curves for first and second configurations (Figure 4.1 bottom, left and middle-left) under uniaxial tensile strain loading in $x = [\bar{1}\bar{1}0]$, $y = [\bar{1}\bar{1}2]$ and $z = [111]$ directions. The rows

correspond to three tensile loading cases while the columns represent the case without and and with the twinned region. At the first glance, the general behavior of twinned fcc and pure fcc under tensile loading is very similar. As expected from the tensile behavior of defect-free perfect fcc crystals in low temperature, we obtain ultra high yield stress up to 20 GPa which are followed by an almost sharp stress relaxation. Since in these loading cases, the coherent twin boundary does not contribute to dislocation nucleation, the yield stress for perfect fcc and twinned crystal is almost the same (Figure 4.2, left column versus right one).

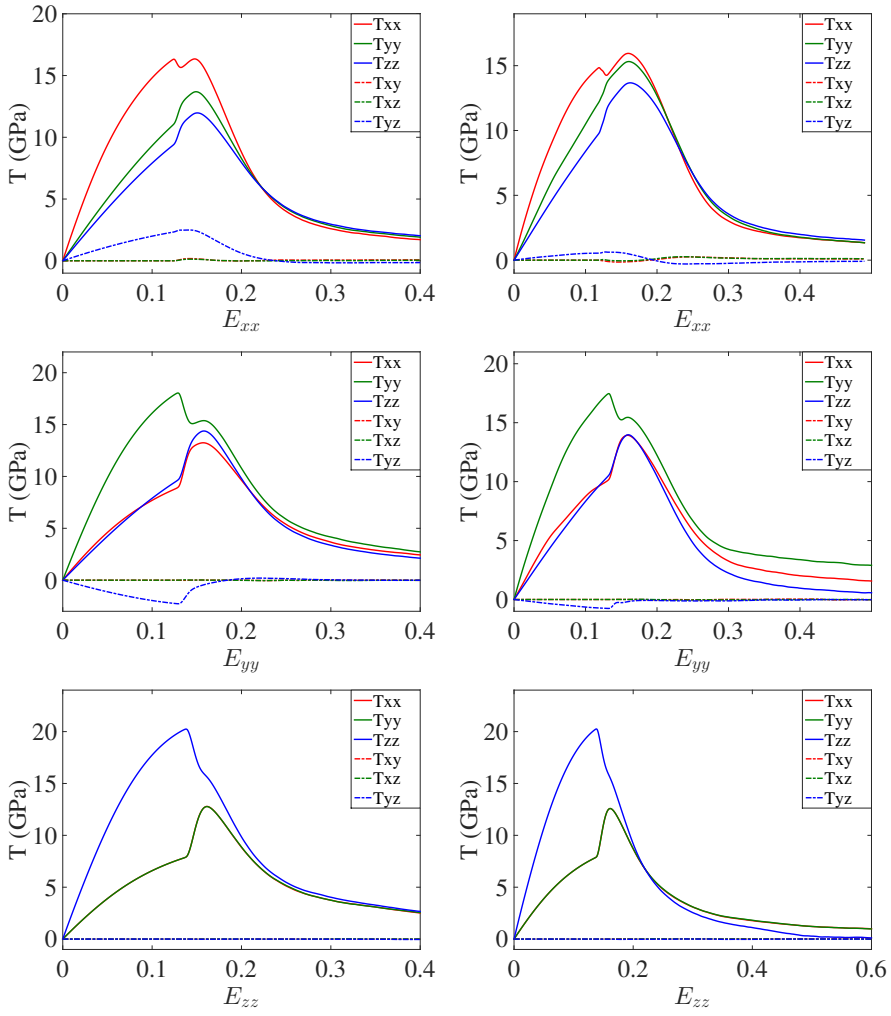


Figure 4.2: Resulted stress-strain curves for perfect fcc and twinned crystal under different tensile strain loading cases. The rows correspond to loading case, i.e. from top to bottom E_{xx}, E_{yy} and E_{zz}, respectively. The left column is the results for perfect fcc (Figure 4.1 bottom, left) and the right column is for the twinned crystal (Figure 4.1 bottom, middle-left).

Considering Figure 4.2 top row, which corresponds to E_{xx} loading in perfect fcc (left) and twinned crystal (right), the elastic part of the stress curve is very similar. The only visible difference in the elastic regime between the two is T_{yz} stress component. As it is seen, in the case of perfect fcc, T_{yz} rises to about 2.5 GPa while in the twinned crystal it is about 1 GPa at highest point before yielding. This is due

to anisotropic elasticity in Cu and the fact that twinned region has different crystallographic orientation compared to parent fcc. Thus, the equivalent elasticity of the whole simulation box in the twinned case is different than the one of perfect fcc leading to different stress-state under same E_{xx} strain loading. This is both visible from T_{yz} and the ratios of T_{xx} to T_{yy} and T_{zz} in two stress curves of Figure 4.2 top row. The plastic regime of these two stress curves seems to be almost isotropic with all normal stress components coinciding on each other and roughly at same stress level for perfect fcc and twinned crystal.

Now, focusing on Figure 4.2 middle row for E_{yy} loading in perfect fcc (left) and twinned crystal (right), the elastic regime is similar to the previous case explained above, with different anisotropy but roughly same yield point. However, in the plastic regime, in the twinned crystal (right) three normal stress components are evolving at different levels compared to the plastic regime in perfect fcc (left). In fact, at the end of the simulation $T_{yy} \approx 3.5$ GPa while $T_{xx} \approx 2.0$ and $T_{zz} \approx 1.0$ GPa for the twinned crystal (right) while for perfect fcc (left) these stress component are all in range of 2 ± 0.2 GPa.

Results of the last tensile loading case, E_{zz}, are shown in Figure 4.2 bottom row. The general behavior is again the same as the two previous cases. However, in this loading case, the yielding point is at about 20 GPa which is much higher compared to the yield point of two other cases at 15 GPa. This implies that dislocation nucleation under this loading (normal to (111) plane) is much harder compared to two other loading directions. In this case, the normal stress components T_{xx} and T_{yy} are exactly the same during the evolution in contrast to slight deviations in the top and middle rows in Figure 4.2. As it is shown in the current case of tensile loading, the different loading directions did not cause any substantial differences in the stress-strain behavior except the relatively higher yield stress in T_{zz} compared to two other loading cases (i.e Figure 4.2 bottom row versus two other rows). Even the presence of twined region or twin boundaries did not cause a significant difference with respect to its perfect fcc counterpart.

Figure 4.3 shows the stress-strain results for configurations with a void in the system (Figure 4.1 bottom, right and middle-right). Again, in these cases we see similar trend as we saw in the previous configurations (i.e. Figure 4.2). The same differences in stress state between fcc crystal and the twinned one due to different anisotropic elasticity is visible. Generally, stress curves in Figure 4.3 for the cases with the void have a smoother transition between elastic and plastic regimes in contrast to sharp stress drop in Figure 4.2 for the cases without the void. This is related to the dislocation nucleation from the void. Since it is much easier to nucleate dislocation from the void than homogeneous dislocation nucleation from perfect fcc lattice, thus, in the cases with the void, dislocations nucleate at much lower stresses, relaxing elastic energy in the simulation box. As the loading continues, the number of dislocations gradually increases and contributes to stress relaxation, resulting in the smooth stress curves seen in Figure 4.3. In contract to this picture, for the cases without the void of Figure 4.2, no dislocation nucleates until stress levels homogeneously reach a critical level and any lattice site in the simulation box has a chance of dislocation nucleation. This leads to sudden nucleation of a large number of dislocations resulting a visible stress drop in the curves in Figure 4.2. The effect of the void is more pronounced in the E_{zz} loading case (Figure 4.3, bottom row) where the ultimate stress is about 17.5 GPa for both perfect fcc and twinned crystals compared to 20 GPa for the same loading without the void. Except the mentioned subtleties in ultimate stress, the general trend for plastic regime in the simulations with the void is similar to ones without the void.

4.3.2 Shear loading

As we saw in the previous section, effect of twinning on the stress-strain curve for the cases of tensile loading is not pronounced. However, for the cases of shear strain loading, a quick glance at Figure 4.4

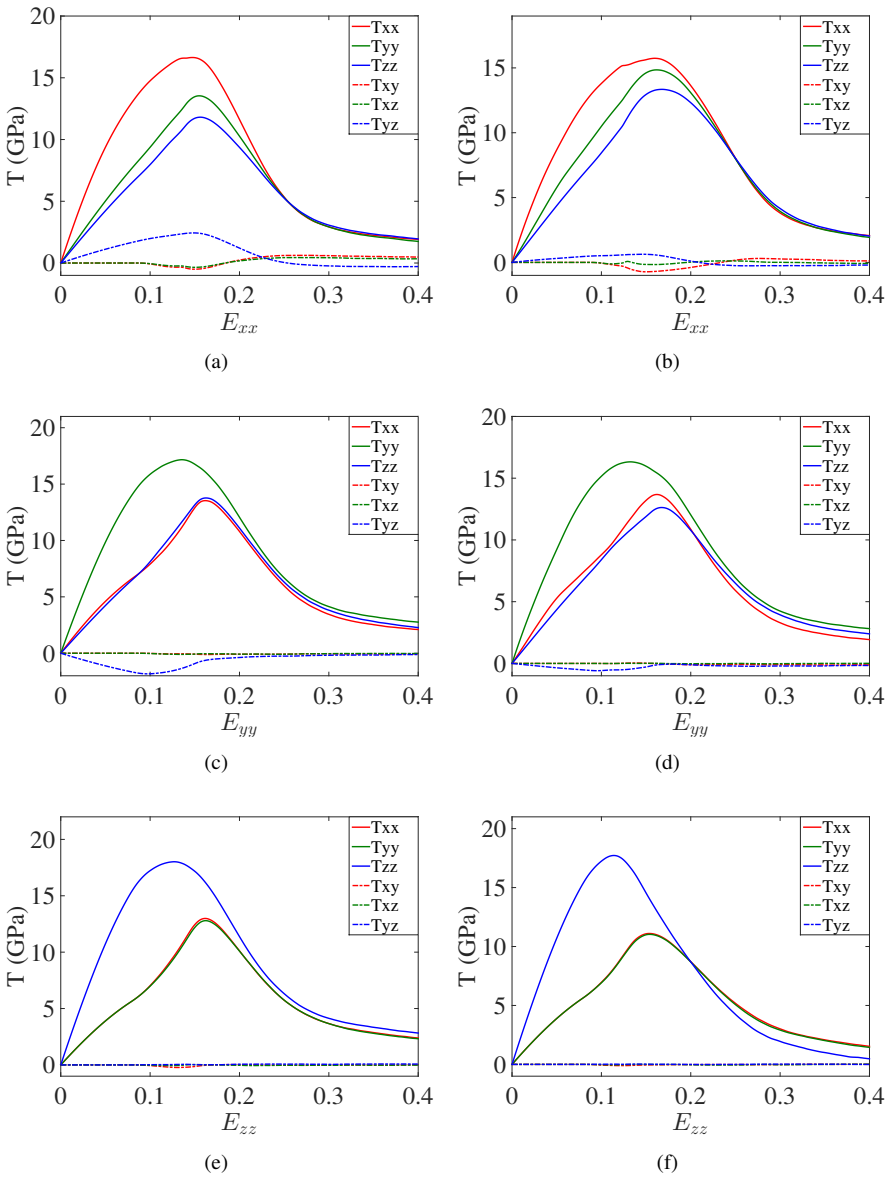


Figure 4.3: Resulted stress-strain curves for fcc and twinned crystals with a void under different tensile strain loading cases. The rows correspond to loading case, i.e. from top to bottom E_{xx}, E_{yy} and E_{zz}, respectively. The left column is the results for fcc crystal with a void (Figure 4.1 bottom, middle-right) and the right column is for the twinned crystal with a void (Figure 4.1 bottom, right).

shows stark differences between stress curves of the perfect fcc and the ones for twinned crystal. These differences and the effect of twinning on the stress flow is discussed in this section.

Considering loading case of E_{yz} (Figure 4.4, top row), the stress curve for the perfect fcc (left) has a clear elastic region followed by sudden yield and stress relaxation as before. Again, due to anisotropic

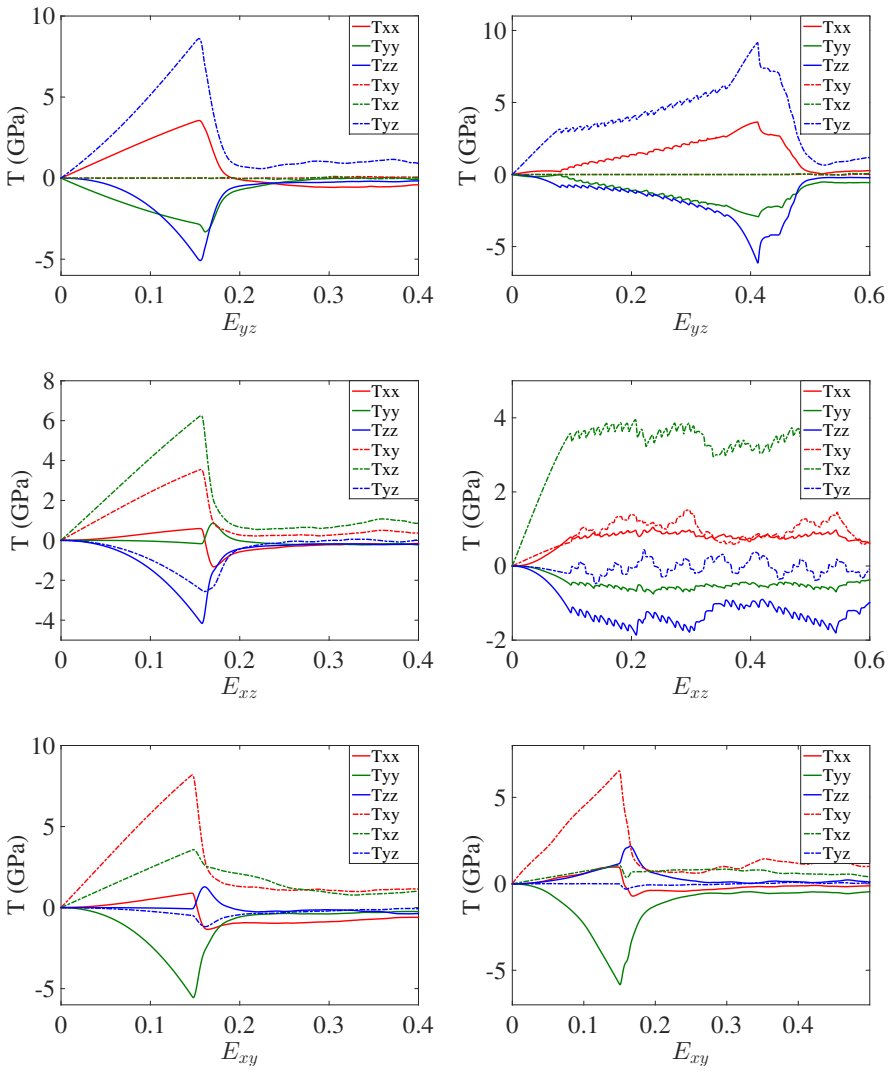


Figure 4.4: Resulted stress-strain curves for perfect fcc and twinned crystal under different shear strain loading cases. The rows correspond to loading case, i.e. from top to bottom E_{yz}, E_{xz} and E_{xy}, respectively. The left column is the results for perfect fcc (Figure 4.1 bottom, left) and the right column is for the twinned crystal (Figure 4.1 bottom, middle-left).

elasticity, several other stress components in addition to the main one T_{yz} are also present. The plastic regime in this case almost behaves like ideal plasticity with zero hardening at stress levels of about $T_{yz} \approx 1$ GPa. However, considering the same loading case for twinned crystal (Figure 4.4, top row, right column), a distinctive jerky-like stress flow with positive hardening is visible. Upon close investigation of the atomic configuration of the system during this jerky flow, it is found that the migration of twin boundary is the cause of this behavior. In fact, each serration in the curve corresponds to one atomic layer movement of the twin boundary. The details of such process are discussed in the next subsection. The jerky part of the stress curve ends at about $E_{yz} = 0.35$ when two twin boundaries reach each other

and, subsequently, the twin region completely vanishes (detwinning). This reduces the twinned crystal box to the perfect fcc case. Since the stress state at this point is not enough for dislocation activity in the perfect fcc, simulation box undergoes a second elastic deformation until the stress level rises up to about $T_{yz} = 9.1$ GPa. Not surprisingly, this value is close to the yield point $T_{yz} = 8.8$ GPa for the perfect fcc in the Figure 4.4, top row left column.

The stress-strain results for E_{xz} loading case are shown in Figure 4.4, middle row. The perfect fcc case (left) is the same as the previous loading case, i.e elastic regime followed by sudden yield and almost ideal plasticity with zero hardening. Of course in this loading case, T_{xz} is the dominant stress component. The stress curve for twinned crystal (Figure 4.4, middle row, right), however, is completely different compared to the perfect fcc. The jerky stress flow as we explained for E_{yz} is again obvious in this case, implying the twin boundary motion. However, in contrast to the jerky flow in the previous loading case, in this case, the jerky behavior does not lead to an average positive hardening. Instead, the stress level remains approximately constant from the beginning of the jerky part to the end of the simulation at $E_{xz} = 0.6$. Again, close investigation of the atomic structure during this oscillating jerky behavior shows that in this loading case, the twin boundary does not move in a certain direction. Instead, the twin boundary moves randomly upward and downward. In other words, there is no preference for twinning or detwinning in this loading case leading to oscillating twin boundary and roughly constant twin thickness during the loading. That is why the twin region will not vanish and there is no second elastic deformation as in E_{yz} loading case. The details of twin boundary motion and oscillation are explained in the next subsection.

The last shear loading case of E_{xy} does not trigger twin boundary movement, thus, there is no jerky stress flow in the Figure 4.4, bottom row. As it is seen from this part of figure, stress-strain curve for both perfect fcc and twinned crystal involves elastic regime, sudden yield and almost ideal plasticity with zero hardening.

Figure 4.5 shows similar shear loading cases as before, this time for the simulation boxes with a void inside. As it is deduced from this figure, the presence of the void does not change the general stress flow and the only visible difference is the smoother yielding region compared to stress curves of the simulations without the void (Figure 4.4). This was already observed and explained for the tensile loading cases in the previous subsection.

4.3.3 Details of twin boundary motion

Among all the loading cases studied in this work, E_{yz} and E_{xz} are the most interesting ones since twin boundary motion is triggered in these cases leading to profoundly different stress-strain curves involving jerky flow. In this subsection, looking more closely at these two cases, we try to understand the twin boundary motion and get insight into the jerky flow.

Snapshots of the simulation box with the twinned region under E_{yz} and E_{xz} are shown in Figures 4.6 and 4.7, respectively. As it was explained for the E_{yz} in previous subsection, the jerky flow part of the stress-strain curve ends due to detwinning after all the twin region is transformed into the parent fcc lattice. This procedure is shown in Figure 4.6 where two twin boundaries are moving toward each other as the loading continues. As we explained before, this eventually leads to annihilation of the twinned region where the second elastic deformation region starts (Figure 4.4 top row, right column).

As it is shown in Figure 4.7 for E_{xz} loading case, although the twin boundaries move during the deformation, this movement is more like an oscillation. As we saw in previous subsection, in this case the

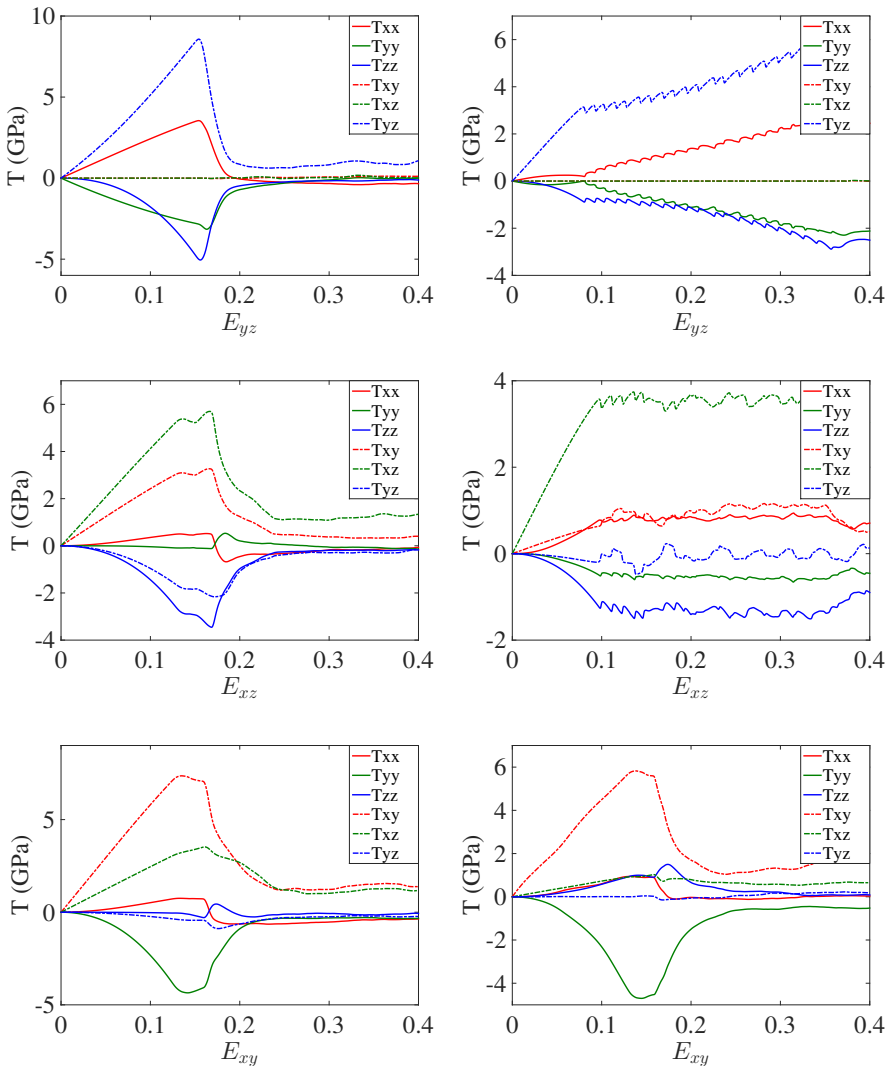


Figure 4.5: Resulted stress-strain curves for fcc and twinned crystals with a void under different shear strain loading cases. The rows correspond to loading case, i.e. from top to bottom E_{yz}, E_{xz} and E_{xy}, respectively. The left column is the results for fcc crystal with a void (Figure 4.1 bottom, middle-right) and the right column is for the twinned crystal with a void (Figure 4.1 bottom, right)

motion of twin boundary still leads to jerk flow (Figure 4.4 middle row, right column). However, since the twinned region will not vanish in this case, theoretically, the plastic deformation could continue infinitely in our periodic simulation box.

Next, we look at the mechanism of twin boundary motion. Figure 4.8 shows a close up of the twin boundary in the middle of its movement. As it is seen from this figure, the twin boundary moves through the formation of partial dislocations on its plane and gliding of those partials along the boundary plane.

The jerky behavior observed in the stress-strain curves is due to the fast motion of the twin boundary.

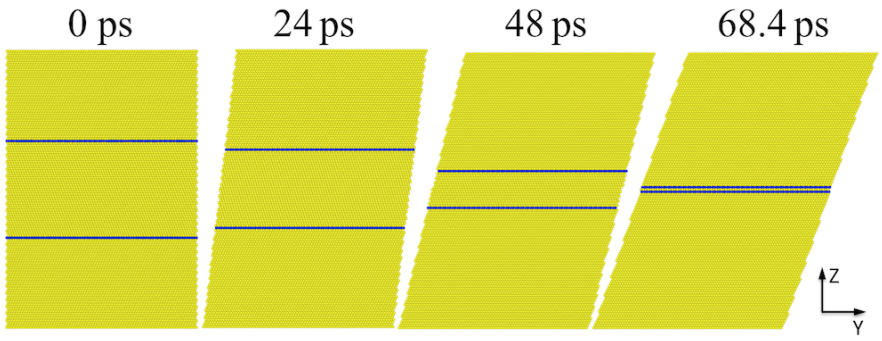


Figure 4.6: Snap shots of simulation box showing detwinning of the middle region under E_{yz} external loading. The resulting stress-strain curve is shown in Figure 4.4 top row, right column.

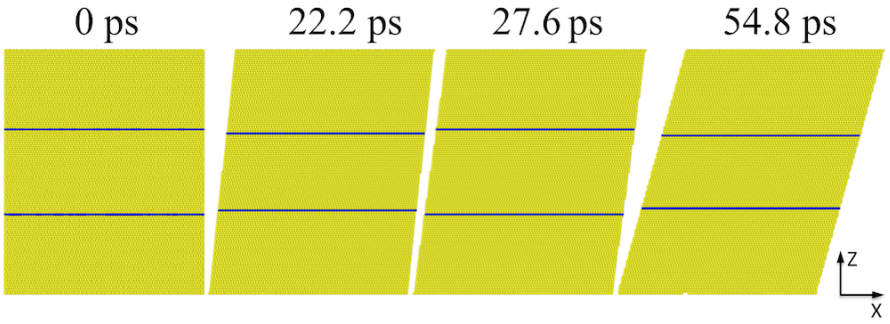


Figure 4.7: Snap shots of simulation box showing twin boundary oscillations under E_{xz} external loading. The resulting stress-strain curve is shown in Figure 4.4 middle row, right column.

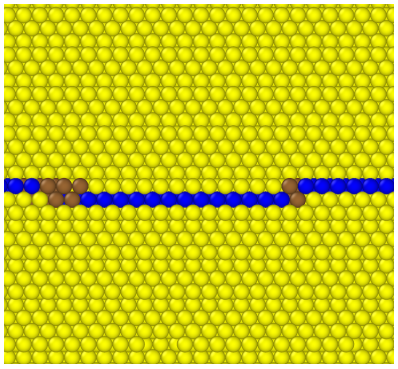


Figure 4.8: Partial dislocation at the twin boundary. The partial dislocation glide shifts the twin boundary one atomic layer.

This fast boundary motion is in turn due to the fact that partial dislocations on the twin boundary move considerably faster that those inside fcc lattice. In fact, as the partial dislocations zip along the twin boundary, the stress relaxation due to their glide is larger than stress rise from the external loading, thus, causing a visible stress relaxation in the curve (i.e in Figure 4.4 top row, right column). After this, the

stress increases again due to external load without any dislocation or twin activity. No dislocation activity in the stress rise in each serration explains why most of them have same slope as the elastic region. The increase of stress continues until the next partial nucleation and subsequent twin boundary motion, resulting in the next stress relaxation.

Now, the next major question remains to discuss is the source of the positive hardening in jerky part of the stress curve for E_{yz} loading case (Figure 4.4 top row, right column) in contrast to almost zero strain hardening in case of E_{xz} (Figure 4.4 middle row, right column). To understand this, we need to look at the homogenous elasticity tensor (or equivalent elasticity tensor) of the whole simulation box with the twinned region. One relevant component of the elasticity tensor is C_{2323} which relates E_{yz} to T_{yz}. Then we see that as the thickness of twinned region decreases, C_{2323} increases. This is clear for the special case where thickness of twin become zero (i.e perfect fcc case). In this case, C_{2323} is the slope of the elastic region for T_{yz} in Figure 4.4 top row, left column, which is about 55.7 GPa. The same parameter for the box with the twinned region (i.e slop of the stress curve for T_{yz} in elastic region in Figure 4.4 top row, right column) is about 40.0 GPa. This is due to the fact that the twinned region have a rotated elasticity tensor compared to parent fcc with lower effective C_{2323}. Keeping this in mind, the strain hardening observed in Figure 4.4 top row, right column is due to the fact that every time twin boundaries move toward each other, the thickness of twinned region reduces by two atomic layers, thus, the effective C_{2323} of the whole box increases and the stress level increases for the same level of strain. There is no strain hardening for E_{xz} loading (Figure 4.4 middle row, right column) since as it is mentioned before, in this case twin boundary oscillates and on average the total volume of the twinned region does not change.

4.4 Conclusion

Different 3D simulation boxes with twinned layers are studied here under all possible strain-based loading conditions. As a reference, simulation boxes without twin are also considered here. Not surprisingly, the pristine fcc crystal has high yield stress followed by an almost sudden drop in stress and zero hardening plasticity afterward. Adding a void into the system reduces the yield stress and also smoothes the stress drop. The twinned crystals behave more or less similar to pristine fcc in the cases of normal strain loadings. However, under shear loading, they behave substantially different. Shear loading E_{yz}, where y is the partial direction in twin plane and z is normal to the twin plane, results in detwinning. Each detwin step creases a serration in stress-strain curve. In addition, reduction in twin volume in this case causes positive hardening. Careful observation of the twin boundary motion revealed that the boundary is translated though fast motion of dislocation at the twin boundary. The jerky flow and the positive hardening is continued in this case until the whole twin layer is transformed back into the parent fcc due to the detwinning. In contrast, the results of E_{xz} loading does not show a net hardening during the simulation. The jerky flow of the stress curve is again due to fast motion of twin boundary. However, in this case, the motion is an oscillation type, thus the volume of the twinned crystal stays the same though out the simulation.

Part II

Continuum-Based Dislocation Modeling

CHAPTER 5

CRITICAL TWINNING STRESS*

"Heavier-than-air flying machines are impossible."
-Lord Kelvin, 1895

5.1 Introduction

As explained in the previous chapter, motion of the twin boundary is related to the partial dislocation activity at the boundary. In this chapter, continuum-based energy formulation for twins consisting of partial dislocations is presented. A simple energy model for twinning including contributions from dislocation interaction, SFs, and external loading was formulated early on by Cooper (1965). More recently, Kibey et al. (2007) formulated an energy model for the critical twinning stress in single-element fcc systems based on Volterra (V) modeling of the dislocation interaction energy (Hirth & Lothe 1982, Chapter 5) and Peierls-Nabarro (PN) (Hirth & Lothe 1982, Chapter 8) modeling of the SF energy. Furthermore, Wang & Sehitoglu (2013, 2014*b*,*a*) applied a similar energy model to fcc shape memory and Ni based alloys with DFT-based SFE calculation. The critical twinning stress is defined in these works as the stress required to sustain and further grow a twin nucleus. Given that the twin has already been nucleated, this stress is referred to as the critical stress for twin growth in this work. In general, this differes from the critical stress for twin nucleation.

A number of studies have looked into the nucleation of the partial dislocations in the context of twin formation. For example, Li et al. (2011) examined the roles played by the unstable SFE, the (intrinsic) SFE, and the unstable twinning fault energy, on the "twinnability" of fcc metals. The effects of dislocation interaction on this, however, are not accounted for in their work. In earlier work, Ogata et al. (2005)

*This chapter is based on the work in Mianroodi & Svendsen (2016*c*)

investigated the energy barriers to nucleation of twin partial dislocations at the boundary of thick twinned regions. Dislocation interaction, anisotropic elasticity, as well as the SFE, are included in their energy model. Hu et al. (2010) developed a phase-field model for stress-induced twinning and detwinning. In particular, their energy model is based on isotropic elastic energy, SFE-based "crystalline" energy, and gradient energy related to the interface between unslipped and slipped regions. Using both atomistic and continuum modeling, Aubry et al. (2011) calculated the energy barriers to homogenous partial dislocation nucleation in Al. On the atomistic side, the nudge elastic band method and the Mishin et al. (2001) interatomic potential for Al were employed to this end. Their continuum model is based on self interaction of partial dislocation loops as well as on the SFE.

With the exception of atomistics and the phase-field work of Hu et al. (2010), all of these studies of twin development are based on the interaction of V dislocations. Likewise, with the exception of atomistics and Kibey et al. (2007), they assume isotropic elasticity. In addition, except for phase-field modeling, all studies are purely energetic-static and assume constant, uniform dislocation spacing; all dynamic or relaxation effects are ignored. One purpose of the current work is the formulation of a bulk twin and twinning model based on PN modeling of both the dislocation interaction and the SFE. In particular, the former is based on the work of Schoeck (1994, 1997, 2014) on PN dislocation interaction. PN- and V-based energy models are compared in detail in the current work in the context of twin nucleation and growth. In addition, the modeling is extended to dynamics in the context of overdamped (relaxational) dislocation motion. Among other things, this facilitates the modeling of (more realistic) variable dislocation separation in the twin. For comparison, the model is applied to bulk nucleation and growth of twins in Al and Cu, characterized by relatively high (Al) and relative low (Cu) SFEs.

This chapter begins in Section 5.2 with a summary of the bulk twin model. On this basis, the energy model for the twin is formulated in Section 5.3. As just discussed, this is based on the PN dislocation model, and for comparison, the V dislocation model. Given these models for energetics, the assumption of constant partial separation in the twin is examined in Section 5.4. The PN model is then applied to formulate critical stress models for twin nucleation and growth. Next, attention is turned to the extension of the model to kinetics and dynamics in Section 5.5 and the modeling of variable dislocation separation.

5.2 Twin model

5.2.1 Geometry

As discussed, the current model formulation is restricted to purely bulk behavior and glide alone (i.e., no climb: Kibey et al. 2007, Wang & Sehitoglu 2013, Schoeck 2014). To this end, as depicted in Figure 5.1, the bulk twin is modeled as an ensemble of N straight parallel partial dislocation dipoles "stacked" on successive (111) glide planes with unit normal $\boldsymbol{i}_y \equiv [111]/\sqrt{3}$. As usual, each partial $\alpha = 1, \ldots, 2N$ is characterized by a line orientation $\boldsymbol{l}_\alpha$ and Burgers vector (BV) $\boldsymbol{b}_\alpha$. In particular, in the current context,

$$\begin{array}{lll} \boldsymbol{l}_\alpha = \boldsymbol{l}\,, & \boldsymbol{b}_\alpha = b\,\boldsymbol{i}_x\,, & \alpha = 1, \ldots, N\,, \\ \boldsymbol{l}_\alpha = \boldsymbol{l}\,, & \boldsymbol{b}_\alpha = -b\,\boldsymbol{i}_x\,, & \alpha = N+1, \ldots, 2N\,, \end{array} \tag{5.1}$$

in terms of $\boldsymbol{i}_x \equiv [11\bar{2}]/\sqrt{6}$ and $b := a_0/\sqrt{6}$. Then $\boldsymbol{i}_z = \boldsymbol{i}_x \times \boldsymbol{i}_y \equiv [1\bar{1}0]/\sqrt{2}$ holds. If $\boldsymbol{l} = \boldsymbol{i}_z$, the the partials are all of edge character. For simplicity, this is assumed here.

Besides line orientation and BV, each partial α is characterized by a location (x_α, y_α) in the (x, y) plane. In particular, the twin structure in Figure 5.1 implies that $y_\alpha = y_{N+\alpha}$ for $\alpha = 1, \ldots, N$. Partials on

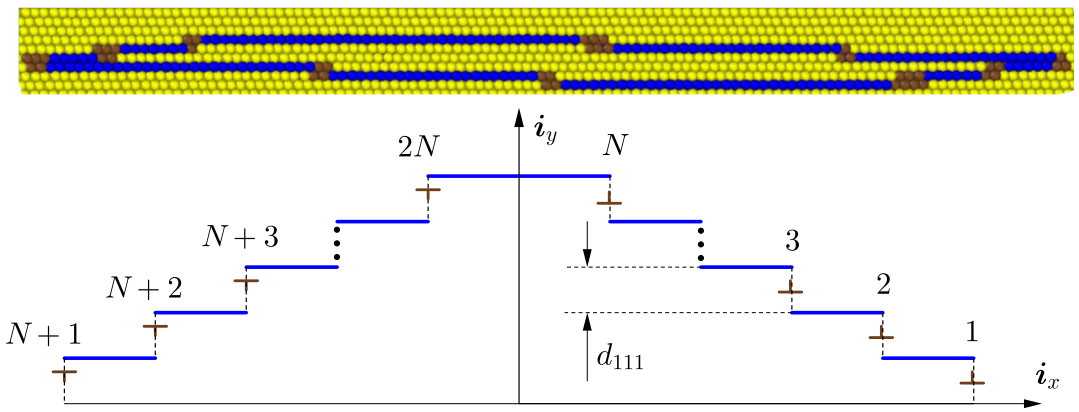


Figure 5.1: Above: results from an MD simulation (using LAMMPS and OVITO: Plimpton 1995, Stukowski 2010) of bulk twin formation in Cu showing the twinned region (yellow; fcc) surrounded by stacking fault surfaces (blue; hcp) separated by dislocation lines (brown; core). Below: idealized (bulk) twin consisting of N straight parallel partial dislocation dipoles (point pairs: $(1, N+1), \ldots, (N, 2N)$) and $2N-1$ stacking faults (blue line segments: $(N+1, N+2), \ldots, (2N, N), \ldots, (2, 1)$). The glide plane of each partial is the (x, z) plane with unit normal $\boldsymbol{i}_y \equiv [111]/\sqrt{3}$ in the current fcc case.

adjacent (111) glide planes are separated in the $\boldsymbol{i}_y$ direction by the glide plane spacing $d = d_{111} = a_0/\sqrt{3}$, where a_0 is the lattice constant. Then $y_\alpha = (\alpha - 1)\, d + d/2 = y_{N+\alpha}$ holds and is constant for $\alpha = 1, \ldots, N$. On the other hand, the x coordinates $\mathbf{x} := (x_1, \ldots, x_{2N})$ of the partials are variable in the current context.

5.2.2 Twin disregistry function

The classic PN model (e.g., Hirth & Lothe 1982, Chapter 8) is based on linear elasticity, isotropy, and a simple Frenkel sinusoidal spatial variation of lattice resistance to dislocation motion. In this case, the mechanical equilibrium problem can be solved analytically (Eshelby 1949) to obtain the corresponding (non-dimensional) disregistry field

$$\phi^{\mathrm{PN}}(x) = \frac{1}{2} - \frac{1}{\pi} \tan^{-1} \frac{x}{c} \tag{5.2}$$

(e.g., Eshelby 1949) across the glide plane $y = 0$ due to a dislocation at $x = 0$ with core size (width) c. The corresponding V field $\phi^{\mathrm{V}}(x)$ is recovered from (5.2) in the limit as c approaches zero, i.e.,

$$\phi^{\mathrm{V}}(x) = \lim_{c \to 0} \phi^{\mathrm{PN}}(x) = \frac{1}{2} - \frac{1}{2} \operatorname{sgn}(x) = h(-x)\,, \tag{5.3}$$

where $\operatorname{sgn}(x)$ is the signum (sign), and $h(x)$ the Heaviside step, function. In the isotropic and fcc cases, for example, c is proportional to the glide-plane spacing d and so to the lattice constant a_0. As has been developed for example by Schoeck (e.g., Schoeck 1994, 2005, 2014), (5.2) can be employed as a "basis" function to construct disregistry fields for more general dislocation configurations (e.g., dipoles).

Relevant to the current work is the disregistry profile

$$\begin{aligned}\phi^{\mathrm{PN}}_{\mathrm{twi}}(x;\mathbf{x}) &= \sum\nolimits_{\alpha=1}^{N} \phi^{\mathrm{PN}}(x-x_\alpha) - \phi^{\mathrm{PN}}(x+x_\alpha) \\ &= \frac{1}{\pi}\sum\nolimits_{\alpha=1}^{N} \tan^{-1}\frac{x+x_\alpha}{c} - \tan^{-1}\frac{x-x_\alpha}{c}\end{aligned} \tag{5.4}$$

for the dipole-based twin model in Figure 5.1. This is shown in Figure 5.2 for the case $N = 3$.

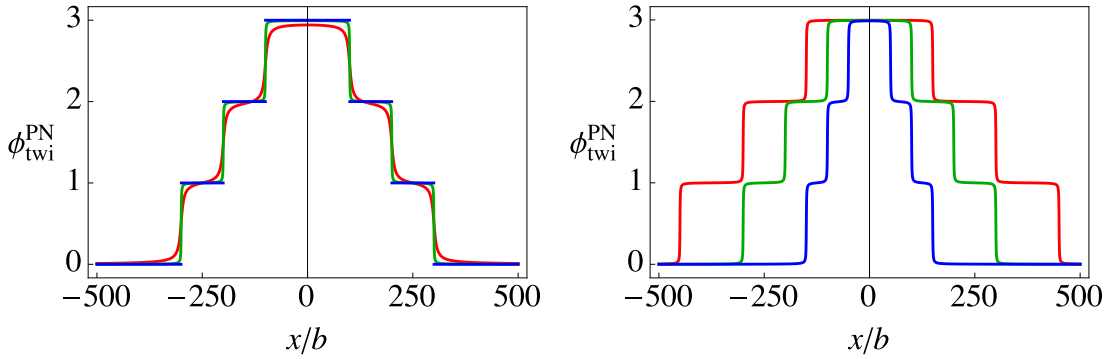


Figure 5.2: PN-based twin disregistry $\phi^{\mathrm{PN}}_{\mathrm{twi}}(x;\mathbf{x})$ from (5.4) for $N = 3$. Left: core sizes $c/b = 5$ (red), $c/b = 0.5$ (green), $c/b = 0$ (blue). Right: uniform dislocation spacings $x_\alpha/b = 150$ (red) $x_\alpha/b = 100$ (green) $x_\alpha/b = 50$ (blue) for $c/b = 0.5$.

Analogous to, and following from, (5.3) is

$$\begin{aligned}\phi^{\mathrm{V}}_{\mathrm{twi}}(x;\mathbf{x}) = \lim_{c\to 0}\phi^{\mathrm{PN}}_{\mathrm{twi}}(x;\mathbf{x}) &= \sum\nolimits_{\alpha=1}^{N} \phi^{\mathrm{V}}(x-x_\alpha) - \phi^{\mathrm{V}}(x+x_\alpha) \\ &= \frac{1}{2}\sum\nolimits_{\alpha=1}^{N} \mathrm{sgn}(x+x_\alpha) - \mathrm{sgn}(x-x_\alpha)\end{aligned} \tag{5.5}$$

for the twin disregistry profile in the V model. As implied by (5.5), and shown in Figure 5.2 (left, blue curve), this is piecewise constant.

5.3 Energy model

The following model formulation is for arbitrary N. Consequently, the vertical twin thickness is not necessarily small compared to horizontal dimension of the system. In the case of the critical stress considered later, unless otherwise stated, the case $N = 3$ is relevant. This is usually regarded as the critical (thinnest) twin nucleus size (e.g., Christian & Mahajan 1995).

5.3.1 Total energy

The model for the total energy $E_{\rm tot}$ (i.e., per unit length of dislocation line) of the twin depicted in Figure 5.1 takes the form

$$E_{\rm tot}(\mathbf{x}) = E_{\rm int}(\mathbf{x}) + E_{\rm sf}(\mathbf{x}) - E_{\rm ext}(\mathbf{x}) + E_0\,. \tag{5.6}$$

In this relation, $E_{\rm int}$ is the contribution from dislocation interaction, $E_{\rm sf}$ is SF contribution, and

$$E_{\rm ext}(\mathbf{x}) = \tau(b/d)\,a(\mathbf{x}) \tag{5.7}$$

represents the "potential" energy of external loading due to the external xy shear stress τ. Here, b/d represents the twin shear strain, and

$$\begin{aligned} a(\mathbf{x}) &= (x_{N+2} - x_{N+1})\,d + \ldots + (N-1)\,(x_{2N} - x_{2N-1})\,d + N\,(x_N - x_{2N})\,d \\ &+ (N-1)\,(x_{N-1} - x_N)\,d + \ldots + (x_1 - x_2)\,d \\ &= \sum\nolimits_{\alpha=1}^{N-1} \alpha\,(x_{N+1+\alpha} - x_{N+\alpha} + x_\alpha - x_{\alpha+1})\,d + N\,(x_N - x_{2N})\,d \end{aligned} \tag{5.8}$$

is the area of the twin region in Figure 5.1. Lastly, E_0 represents all contributions to $E_{\rm tot}$ which are independent of $\mathbf{x}$, e.g., the self energy of individual dislocations or dislocation line energy (e.g. Wang & Sehitoglu 2013) in the twin. For comparison of the PN and V models, the value of E_0 is chosen in such a way that $E_{\rm tot}$ goes to zero as the separation between monopoles in a dipole does (i.e., zero total energy).

5.3.2 Interaction energy

Let $E_{\alpha\beta}$ represent the interaction energy between α and β for $\alpha \neq \beta$. In particular, in the case of the V model, the classic result

$$E^{\rm V}_{\alpha\beta}(\mathbf{x}) = \boldsymbol{b}_\alpha \cdot \boldsymbol{H}\boldsymbol{b}_\beta\, \ln\frac{r_0^2}{r^2_{\alpha\beta}(\mathbf{x})} = H_{xx}\, b_{\alpha x}\, b_{\beta x}\, \ln\frac{r_0^2}{r^2_{\alpha\beta}(\mathbf{x})} \tag{5.9}$$

(e.g., Hirth & Lothe 1982, Equation (13-187)) holds for the change in energy of two parallel straight V dislocations due to a change in separation from r_0 to

$$r^2_{\alpha\beta}(\mathbf{x}) = |\boldsymbol{r}_{\alpha\beta}|^2 = (x_\alpha - x_\beta)^2 + (y_\alpha - y_\beta)^2\,. \tag{5.10}$$

As indicated, in the current context (see Figure 5.1), y_α is a function of d and constant for each dislocation. Here, $\boldsymbol{H}$ represents the symmetric Stroh tensor derived from the elastic stiffness (Stroh 1958). The second expression in (5.9) is based on the fact that, in the current fcc context, the component matrix of $\boldsymbol{H}$ with respect to $(\boldsymbol{i}_x, \boldsymbol{i}_y, \boldsymbol{i}_z)$ (Figure 5.1) is diagonal. For the case of a dipole $\boldsymbol{b}_\beta = -\boldsymbol{b}_\alpha$, (5.9) generalizes to

$$E^{\rm V}_{\alpha\beta}(\mathbf{x}) = 2\,E^{\rm V}_{\rm c}(\theta_{\alpha\beta}) + \boldsymbol{b}_\alpha \cdot \boldsymbol{H}\boldsymbol{b}_\alpha\, \ln\frac{r^2_{\alpha\beta}(\mathbf{x})}{r_c^2} \tag{5.11}$$

(e.g., Clouet 2009) depending on the additional contribution $E^{\rm V}_{\rm c}(\theta_{\alpha\beta})$ due to core tractions at $r = r_c$. As indicated, $E^{\rm V}_{\rm c}$ depends only on the azimuthal angle $\theta_{\alpha\beta}$ between α and β in the (x, y) plane, i.e., explicitly independent of $r_{\alpha\beta}$. Again, for simplicity, any such self contributions which are independent of $r_{\alpha\beta}$ are included in E_0.

Following the recent work of Schoeck (2014), consider next the PN-based model*

$$E^{\mathrm{PN}}_{\alpha\beta}(\mathbf{x}) = H_{xx}\, b_{\alpha x}\, b_{\beta x} \begin{cases} \ln \dfrac{r_0^2/4c^2}{1 + r^2_{\alpha\beta}(\mathbf{x})/4c^2} & \boldsymbol{b}_\beta = \boldsymbol{b}_\alpha \\ \ln \dfrac{1}{1 + r^2_{\alpha\beta}(\mathbf{x})/4c^2} & \boldsymbol{b}_\beta = -\boldsymbol{b}_\alpha \end{cases} \tag{5.12}$$

for $E_{\alpha\beta}(\mathbf{x})$ with $r_0 \gg c$. To derive this relation, Schoeck (2014) assumed that α and β are on the same glide plane, i.e., $y_\alpha = y_\beta$. In the current work, (5.12) is assumed to be (at least approximately) correct as well in the more general case that $r^2_{\alpha\beta}$ is given by (5.10).

Given such relations for $E_{\alpha\beta}$, summation over all distinct dislocation pairs in the twin in Figure 5.1 yields

$$\begin{aligned} E_{\mathrm{int}}(\mathbf{x}) &= \sum_{\alpha=1}^{2N-1} \sum_{\beta=\alpha+1}^{2N} E_{\alpha\beta}(\mathbf{x}) \\ &= \sum_{\alpha=1}^{N} \sum_{\beta=\alpha+1}^{N} E_{\alpha\beta}(\mathbf{x}) + \sum_{\alpha=1}^{N} \sum_{\beta=N+1}^{2N} E_{\alpha\beta}(\mathbf{x}) + \sum_{\alpha=N+1}^{2N-1} \sum_{\beta=\alpha+1}^{2N} E_{\alpha\beta}(\mathbf{x})\,. \end{aligned} \tag{5.13}$$

In particular, this takes the form

$$\frac{E^{\mathrm{V}}_{\mathrm{int}}(\mathbf{x})}{H_{xx}b^2} = \left\{ \sum_{\alpha=1}^{N} \sum_{\beta=\alpha+1}^{N} + \sum_{\alpha=N+1}^{2N-1} \sum_{\beta=\alpha+1}^{2N} \right\} \ln \frac{r_0^2}{r^2_{\alpha\beta}(\mathbf{x})} + \sum_{\alpha=1}^{N} \sum_{\beta=N+1}^{2N} \ln \frac{r^2_{\alpha\beta}(\mathbf{x})}{r_0^2} \tag{5.14}$$

in the V-based model via (5.1) and (5.9). Likewise,

$$\begin{aligned} \frac{E^{\mathrm{PN}}_{\mathrm{int}}(\mathbf{x})}{H_{xx}b^2} &= \left\{ \sum_{\alpha=1}^{N} \sum_{\beta=\alpha+1}^{N} + \sum_{\alpha=N+1}^{2N-1} \sum_{\beta=\alpha+1}^{2N} \right\} \ln \frac{r_0^2/4c^2}{1 + r^2_{\alpha\beta}(\mathbf{x})/4c^2} \\ &+ \sum_{\alpha=1}^{N} \sum_{\beta=N+1}^{2N} \ln \left(1 + \frac{r^2_{\alpha\beta}(\mathbf{x})}{4c^2} \right) \end{aligned} \tag{5.15}$$

follows for the PN-based model via (5.1) and (5.12). As basically already evident in (5.12), note that the last (i.e., dipole) term in $E^{\mathrm{PN}}_{\mathrm{int}}(\mathbf{x})$ is independent of the "system size" r_0.

5.3.3 Stacking fault energy

Following previous works (e.g., Schoeck 1994, 2005, Kibey et al. 2007, Wang & Sehitoglu 2013, Schoeck 2014), the stacking fault energy (SFE) per unit length $E_{\mathrm{sf}}(\mathbf{x})$ can be modeled with the help of a disregistry field ϕ along the energy pathway of interest. For the current twin model, this takes the form

$$E_{\mathrm{sf}}(\mathbf{x}) = \int_{-\infty}^{+\infty} \gamma_{\mathrm{SFE}}(\phi_{\mathrm{twi}}(x;\mathbf{x}))\, dx \tag{5.16}$$

in terms of the (area) density $\gamma_{\mathrm{SFE}}(\phi)$. As indicated, in the current twin context, this is parameterized by a corresponding disregistry function $\phi = \phi_{\mathrm{twi}}(x;\mathbf{x})$. For particular materials, data on γ_{SFE} is generally

*Again, (5.12) represents only the interaction part of Equation (6) from Schoeck (2014).

obtained with the help of either DFT or interatomic potentials. Most commonly, a (Fourier) representation of $\gamma_{\mathrm{SFE}}(\phi)$ in terms of sine and cosine functions is then fit to this data (e.g. Kibey et al. 2007, Wang & Sehitoglu 2013, 2014*b*,*a*). In contrast, in the current work, a direct fit of $\gamma_{\mathrm{SFE}}(\phi)$ to data based on piecewise cubic spline functions is employed. Among other things, this results in improved accuracy of quantitative results.

As shown in Figure 5.3 for Al and Cu, γ_{SFE} is periodic for $\phi > 2$; consequently, γ_{SFE} is determined atomistically for $\phi \in [0, 2]$. In this case, note that the unstable extrinsic SFE γ_{UEF} is approximately equal

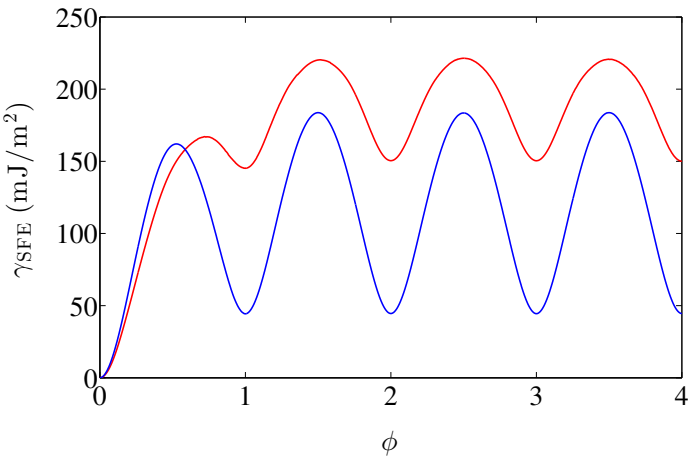


Figure 5.3: SFE curves for Al (red) and Cu (blue) calculated from interatomic potentials. See text for details.

to the unstable twinning SFE γ_{UTF}. Likewise, the extrinsic SFE γ_{ESF} is then approximately equal to the twinning SFE γ_{TSF} (see Table 5.1 below for Al and Cu). With the help of the transformation

$$p(\phi) = \begin{cases} \phi & \phi \leqslant 2 \\ \phi - \lfloor \phi \rfloor + 1 & (2 < \phi) \wedge (\lfloor 2\phi \rfloor = 2k+1) \\ \lfloor \phi \rfloor - \phi + 2 & (2 < \phi) \wedge (\lfloor 2\phi \rfloor = 2k) \end{cases} \tag{5.17}$$

values of $\phi > 2$ can then be accounted for in the model. Given (5.17),

$$E_{\mathrm{sf}}^{\mathrm{PN}}(\mathbf{x}) = \int_{-\infty}^{+\infty} \gamma_{\mathrm{SFE}}(p(\phi_{\mathrm{twi}}^{\mathrm{PN}}(x;\mathbf{x}))) \, dx \tag{5.18}$$

then follows from (5.16) and the PN-dipole-based form $\phi_{\mathrm{twi}}^{\mathrm{PN}}(x;\mathbf{x})$ from (5.4). Likewise,

$$E_{\mathrm{sf}}^{\mathrm{V}}(\mathbf{x}) = \lim_{c\to 0} E_{\mathrm{sf}}^{\mathrm{PN}}(\mathbf{x}) = \int_{-\infty}^{+\infty} \gamma_{\mathrm{SFE}}(p(\phi_{\mathrm{twi}}^{\mathrm{V}}(x;\mathbf{x}))) \, dx \tag{5.19}$$

holds in the V-based model formulation in terms of the corresponding twin disregistry function $\phi_{\mathrm{twi}}^{\mathrm{V}}(x;\mathbf{x})$ from (5.5). In fact, since $\phi_{\mathrm{twi}}^{\mathrm{V}}(x;\mathbf{x})$ is piecewise constant in x, (5.19) reduces to

$$\begin{aligned} E_{\mathrm{sf}}^{\mathrm{V}}(\mathbf{x}) &= \gamma_{\mathrm{ISF}}(x_1 - x_2) + \gamma_{\mathrm{ISF}}(x_{N+2} - x_{N+1}) \\ &+ \gamma_{\mathrm{TSF}}(x_2 - x_{N+2}) \,, \end{aligned} \tag{5.20}$$

consisting of products of stable stacking fault energies and corresponding segment lengths. Here, γ_{ISF} represents the intrinsic SFE. The result (5.20) is consistent for example with the model of Cooper (1965) generalized to the current context.

In contrast to the analytical result (5.20) for $E_{\mathrm{sf}}^{\mathrm{V}}(\mathbf{x})$, the integral relation (5.18) for $E_{\mathrm{sf}}^{\mathrm{PN}}(\mathbf{x})$ must be evaluated numerically for computational purposes. To this end, consider its approximation / discretization as the Riemann sum

$$E_{\mathrm{sf}}^{\mathrm{PN}}(\mathbf{x}) \approx \sum_{i=-n}^{+n} \gamma_{\mathrm{SFE}}(p(\phi_{\mathrm{twi}}^{\mathrm{PN}}(i\Delta x;\mathbf{x}))\,\Delta x \tag{5.21}$$

for "large" n. The most accurate approximation in this sense would be obtained when the numerical resolution is atomic, i.e., $\Delta x = b$. Indeed, in this case, the sum in (5.21) would actually correspond to the atomic positions and the number of atoms. In the actual cases examined below, the difference between the discrete form (5.21) with atomic resolution and the integral form (5.18) of $E_{\mathrm{sf}}^{\mathrm{PN}}(\mathbf{x})$ is very small in the static case. On the other hand, in the dynamic case, these differ substantially. To be more precise, we are comparing (i) the discrete sum in (5.21) with $\Delta x = b$, representing the energy sum over actual atomic positions, and (ii) the same sum with $\Delta x = b/10$, corresponding to an approximate of the continuum integral (5.18). Since the SFE is physically atomic in nature, the discrete relation (5.21) with atomic resolution $\Delta x = b$ is physically "exact", and the PN-based continuum relation (5.18) is a (very good) mathematical approximation (e.g., in the sense of model-order reduction) to (5.21).

5.4 Comparisons for uniform dislocation separation

For the purpose of comparing the above PN- and V-based energy models, material data are calculated with the help of interatomic potentials of Mishin et al. (1999) and Mishin et al. (2001) for Al and Cu, respectively. These interatomic potentials are used in a number of studies related to dislocations (e.g. Tucker et al. 2012, Wei & Wei 2012, Aubry et al. 2011) and have been shown to provide SFE data in agreement with DFT results Zimmerman et al. (2000). The results are shown in Table 5.1.

Basic	Al	Cu
a_0 [Å]	4.05	3.62
d [Å]	2.34	2.09
b [Å]	1.65	1.48
c [Å]	1.76	1.54

Elastic	Al	Cu
C_{11} [GPa]	113.8	169.9
C_{12} [GPa]	61.5	122.6
C_{44} [GPa]	31.6	76.2
H_{xx} [GPa]	2.29	3.38

	γ_{USF}	γ_{ISF}	γ_{UEF}	γ_{ESF}	γ_{UTF}	γ_{TSF}
Al	167.0	145.2	220.3	150.4	221.4	150.4
Cu	162.0	44.3	183.7	44.5	183.5	44.4

Table 5.1: Interatomic-potential-based material data for Al and Cu and derived quantities. The latter include c calculated from d and $\nu_{\mathrm{eff}} = (C_{11} + 4C_{12} - 2C_{44})/(4C_{11} + 6C_{12} - 2C_{44})$ via the Frenkel-based isotropic relation $d/2(1-\nu_{\mathrm{eff}})$ (Hirth & Lothe 1982, Chapter 8). As well, H_{xx} is calculated from C_{11}, C_{12}, C_{44} via the approach of Eshelby et al. (1953) and Forman (1955) as described in detail in Hirth & Lothe (1982, §§13-3, 13-4, 13-6). All SFE data are in mJ/m^2. γ_{USF} represents the unstable SFE.

To begin, assume for simplicity that the horizontal separation between adjacent partials is uniform (e.g., Kibey et al. 2007, Wang & Sehitoglu 2013) and equal to $s\,b$. Then $x_\alpha(s) = (N - \alpha + 1)\,s\,b\,,\ \alpha =$

$1, \ldots, N$, holds, and all functions of $\mathbf{x}$ becomes functions of s via composition. For example, $\phi^{\mathrm{PN}}_{\mathrm{twi}}(x;s)$ and $\gamma_{\mathrm{SFE}}(p(\phi^{\mathrm{PN}}_{\mathrm{twi}}(x;s)))$ for Cu as shown in Figure 5.4.

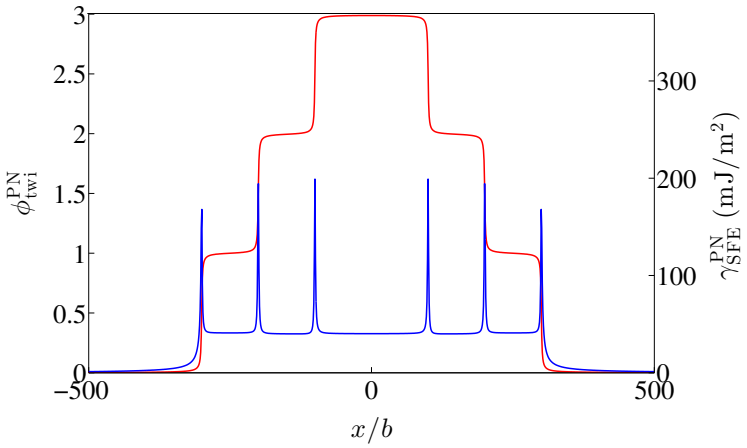


Figure 5.4: $\phi^{\mathrm{PN}}_{\mathrm{twi}}(x;s)$ (red curve) from (5.4) and $\gamma^{\mathrm{PN}}_{\mathrm{SFE}}(x;s) := \gamma_{\mathrm{SFE}}(p(\phi^{\mathrm{PN}}_{\mathrm{twi}}(x;s)))$ (blue curve) from (5.18) for Cu assuming $s = 100$. Value for c from Table 5.1.

As shown, part of the SFE is in the dislocation cores (spikes). Since c remains constant as s increases, this contribution to $E^{\mathrm{PN}}_{\mathrm{sf}}$ remains constant. Consequently, as s, and so the stacking fault area, increases, the shape and the magnitude of the spikes remains constant, and further energy is stored only in the stacking faults. This is the reason that, as shown in Figure 5.5, the difference $E^{\mathrm{PN}}_{\mathrm{sf}}(s) - E^{\mathrm{V}}_{\mathrm{sf}}(s)$ is basically constant after $s > 10$.

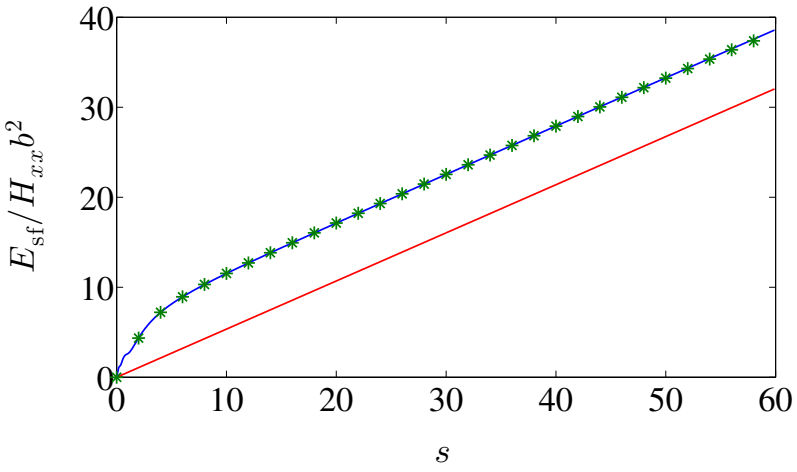


Figure 5.5: Comparison of $E^{\mathrm{V}}_{\mathrm{sf}}(s)$ (red curve) from (5.20) and $E^{\mathrm{PN}}_{\mathrm{sf}}(s)$ (blue curve, green asterisks) from (5.21) for Cu. Blue curve: $\Delta x = b/10$. Green asterisks: $\Delta x = b$. Clearly, $E^{\mathrm{PN}}_{\mathrm{sf}}(s)$ is independent of Δx for $\Delta x \leqslant b$.

Indeed, since it includes energy storage in the cores (energy spikes), $E_{\rm sf}^{\rm PN}(s) > E_{\rm sf}^{\rm V}(s)$. Beyond $s > 10$, the increase in $E_{\rm sf}^{\rm PN}(s)$ is due to growth of SFs and so similar to $E_{\rm sf}^{\rm V}(s)$ from (5.20). As shown in Figure 5.5, in the static case, $E_{\rm sf}^{\rm PN}(s)$ is insensitive to discretization.

Consider next the results for $E_{\rm tot}(s)$ from (5.6) for the two dislocation models shown in Figure 5.6. As shown, $E_{\rm ext}(s)$ and $E_{\rm sf}^{\rm V}(s)$ increase linearly, and $E_{\rm sf}^{\rm PN}(s)$ nearly so, with s. On the other hand, as

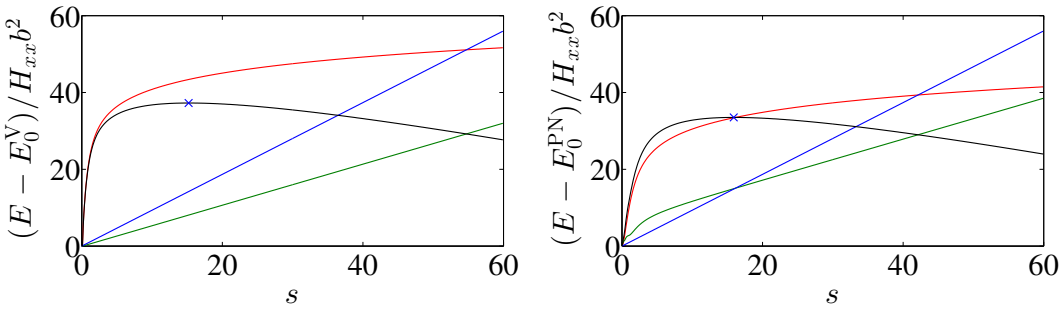


Figure 5.6: V-based (left) and PN-based (right) results for $E_{\rm tot}(s)$ (black), $E_{\rm int}(s)$ (red), $E_{\rm sf}(s)$ (green), and $E_{\rm ext}$ (blue), for a Cu twin nucleus ($N = 3$, Figure 5.1) at $\tau = 400$ MPa. In all cases, $r_0 = 1000\,b$. The blue cross marks the maximum of $E_{\rm tot}(s)$ at $s_{\rm max}^{\rm V} = 15.2$ (left) and $s_{\rm max}^{\rm PN} = 15.9$ (right).

expected from the functional forms (5.14) and (5.15), $E_{\rm int}(s)$ for both models increases logarithmically with s. The corresponding total energy $E_{\rm tot}(s)$ reaches a maximum value at $s = s_{\rm max}$ (blue crosses in Figure 5.6), representing the critical twin size $s_{\rm cri} := s_{\rm max}$ at the corresponding load ($\tau = 400$ MPa in Figure 5.6). Any twin nucleus larger than this is stable and will grow since this results in a reduction of the total energy. On the other hand, all twin nuclei below this size are energetically unfavorable and will vanish.

Figure 5.7 displays the dependence of $\tau_{\rm cri}$ on the initial twin size s predicted by the V- and PN-based models.

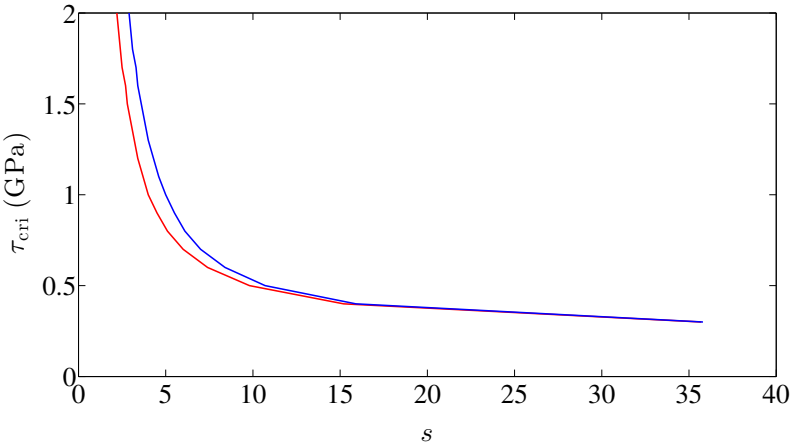


Figure 5.7: Comparison of $\tau_{\rm cri}^{\rm V}(s)$ (red) and $\tau_{\rm cri}^{\rm PN}(s)$ (blue) for Cu with $N = 3$.

As evident, $\tau_{\mathrm{cri}}(s)$ becomes basically independent of s for increasing s and converges to

$$\tau_{\mathrm{gro}} = \lim_{s\to\infty} \tau_{\mathrm{cri}}(s) = \frac{\gamma_{\mathrm{TSF}}}{3b}\,, \tag{5.22}$$

representing the critical stress for twin growth. Since dislocation interaction becomes vanishingly small as $s \to \infty$, only the SFE and external loading contribute to the energy maximum and so to τ_{gro}. Consequently, any finite-size twins subject to loads less that τ_{gro} will shrink and vanish. The factor of 3 in the denominator is due to the assumption $N = 3$; in general, it should be replaced by N.

Necessary and sufficient for the formation of twin nuclei themselves is the corresponding critical stress

$$\tau_{\mathrm{nuc}} = \lim_{s\to 0} \tau_{\mathrm{cri}}(s)\,. \tag{5.23}$$

In particular, the first step in twin nucleation is the nucleation of the first partial dipole. Corresponding critical stress calculations for the case of $N = 1$ are shown in Figure 5.8.

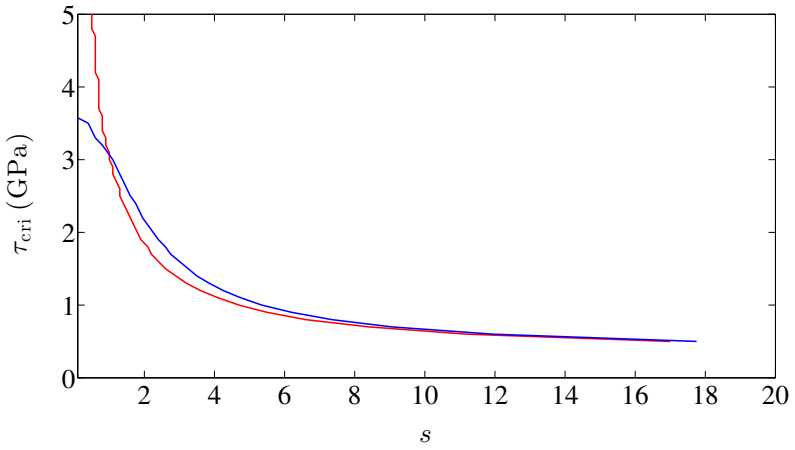


Figure 5.8: Comparison of $\tau^{\mathrm{V}}_{\mathrm{cri}}(s)$ (red) and $\tau^{\mathrm{PN}}_{\mathrm{cri}}(s)$ (blue) for Cu with $N = 1$, i.e. one partial dislocation dipole.

These results show that, as s decreases toward zero, $\tau_{\mathrm{cri}}(s)$ increases almost proportional to $1/s$. This is due to the fact that the attractive force between dipoles increases as they get closer. As a result, the stress required to separate them and enlarge the twin increases. Consequently, $\tau^{\mathrm{V}}_{\mathrm{nuc}} = \infty$. On the other hand, as shown in Figure 5.8, $\tau^{\mathrm{PN}}_{\mathrm{cri}}$ is finite. As such, this is effectively the critical stress for partial dislocation nucleation. As to be expected, calculated nucleation stresses for the twin case ($N = 3$) are much larger than for the partial dislocation case ($N = 1$). Consequently, twin formation will be gradual, and the next partial dipole will nucleate only after the first one has nucleated and moved away from the nucleation site.

Results for τ_{gro} and $\tau^{\mathrm{PN}}_{\mathrm{nuc}}$ for Al and Cu are listed in Table 5.2. Since the homogeneous dislocation nucleation takes place at large applied stress, lattice deformation is also involved. Before nucleation, external loading drives the disregistry state up the first SFE-based energy barrier from $\phi = 0$ to ϕ_0. To account for this, ϕ is set to the constant value ϕ_0 in unslipped parts of the domain. For example, in Figure 5.4, instead of $\phi = 0$ in regions of $300 < x/b$ and $x/b < -300$, $\phi = \phi_0$ is assumed in those regions. ϕ_0 is determined by solving the nonlinear equation $\partial_\phi \gamma_{\mathrm{SFE}}|_{\phi=\phi_0} = b\tau$ for each choice of τ. This procedure is equivalent to Model II in Aubry et al. (2011). Note also that ϕ_0 is comparable to $h\tau/\mu$ from Rice (1992).

	Units	Al	Cu
τ_{gro}	MPa	303	100
$\tau_{\mathrm{nuc}}^{\mathrm{PN}}$	GPa	2.6	3.6
$\tau_{\mathrm{nuc}}^{\mathrm{id}}$	GPa	2.3	3.2

Table 5.2: Comparison of critical stress results for Al and Cu. These are compared with the ideal nucleation stress $\tau_{\mathrm{nuc}}^{\mathrm{id}} = b^{-1} \max \partial_\phi \gamma_{\mathrm{SFE}}$ from Aubry et al. (2011).

As explained above, the direct SFE fit to atomistic data employed in this work is much more accurate than works based on piecewise periodic sine-cosine functions (e.g. Kibey et al. 2007, Wang & Sehitoglu 2013, 2014*b*,*a*). Accurate SFE data especially in the region $0 < \phi < 1$ is crucial for accurate nucleation stress calculation since the derivative of SFE in this region is used to determine ϕ_0 as explained above.

Since τ_{nuc} from (5.23) represents the homogeneous nucleation and formation of partial dislocations in defect-free bulk material, the large values for Al and Cu shown in Table 5.2 are to be expected (see also e.g. Aubry et al. 2011). In the more realistic case of pre-existing dislocations or twins, of course, τ_{gro} becomes relevant.

5.5 Dynamic modeling

5.5.1 Model relations

As discussed in the introduction, a more realistic twin model should include the possibility of variable separation between the partials. Due to interactions, for example, it is known that the partials are closer to each other around the twin tip (e.g., Christian & Mahajan 1995). For simplicity, consider to this end the relaxational "overdamped" equation of motion

$$\dot{x}_\alpha = m\, f_\alpha \tag{5.24}$$

for each partial α in terms of the mobility m (assumed the same for all dislocations) and the corresponding driving force

$$\begin{array}{rcccccccc} f_\alpha & = & -\partial_{x_\alpha} E_{\mathrm{tot}} & = & -\partial_{x_\alpha} E_{\mathrm{int}} & - & \partial_{x_\alpha} E_{\mathrm{sf}} & + & \partial_{x_\alpha} E_{\mathrm{ext}} \\ & & & = & f_{\mathrm{int}\,\alpha} & + & f_{\mathrm{sf}\,\alpha} & - & f_{\mathrm{ext}\,\alpha} \end{array} \tag{5.25}$$

via (5.6). As an example of these forces, consider the results for $f_{\mathrm{int}\,\alpha}^{\mathrm{V}}(s)$ and $f_{\mathrm{int}\,\alpha}^{\mathrm{PN}}(s)$ for one dislocation dipole ($N = 1$) with separation s shown in Figure 5.9.

As shown and expected, $f_{\mathrm{int}\,\alpha}^{\mathrm{V}}(s)$ diverges as $s \to 0$, whereas $f_{\mathrm{int}\,\alpha}^{\mathrm{PN}}(s)$ has a finite maximum attractive force of $f_{\max}^{\mathrm{PN}} = H_{xx} b^2 / 4\pi c$. Assuming for example $c = d/2(1-\nu)$, the maximum attractive force between two monopoles is $f_{\max}^{\mathrm{PN}} = H_{xx} b^2 (1-\nu)/2\pi d$. Also shown in Figure 5.9 is $f_{\mathrm{int}}^{\mathrm{V}}(s) \approx f_{\mathrm{int}}^{\mathrm{PN}}(s)$ for $s > 5$.

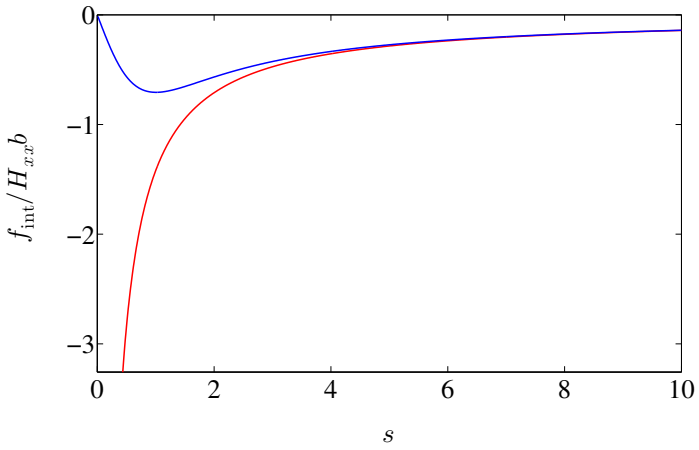


Figure 5.9: Comparison of $f_{\rm int}^{\rm V}(s)$ (red curve) and $f_{\rm int}^{\rm PN}(s)$ (blue curve) for $N = 1$ (one dipole) in Cu.

5.5.2 Variable dislocation separation

Given the above dynamic model, consider now the behaviour of twin nucleus under loading. Assume that all adjacent partials have the same initial separation of $s = 100$. This unstable initial configuration is then allowed to relax via dislocation motion modeled by (5.24)-(5.25), in which case a dislocation distribution with variable separation s along the twin. For simplicity, the system size is kept constant at $r_0 = 10^4 b$ in all cases.

To begin, assume $N = 30$ and $\tau = 800$ MPa. Figure 5.10 (left) displays results for the velocity of two dislocations in the twin as a function of time. As shown, V- and PN-based results are very close to each

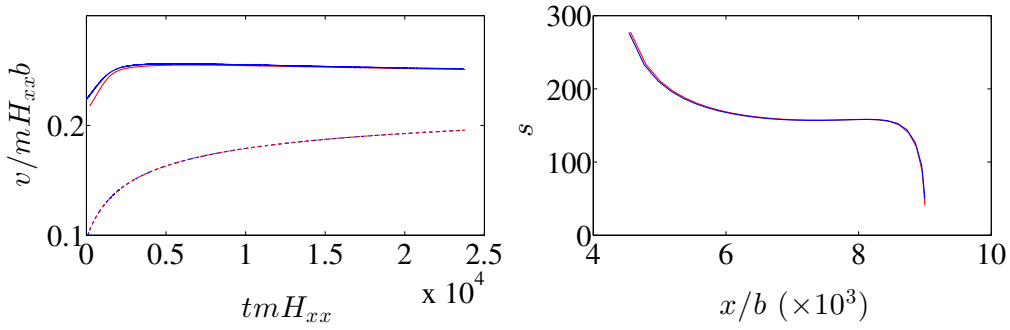


Figure 5.10: Left: non-dimensional velocity $v/m\,H_{xx}b$ of the dislocation at the twin tip (solid lines; $n = 1$ in Figure 5.1) and the center of the twin (dashed lines; $n = N = 30$ in Figure 5.1), as function of non-dimensional time $t\,m\,H_{xx}$. Blue lines are the results based on PN model and the red lines correspond to the V-based model. Right: dislocation separation s as a function of position at "almost" steady-state (i.e. end of the simulation in the left panel).

other, mainly due to large dislocation separations. In both cases, the system evolves toward nearly steady state with almost constant velocities. Because of the dependence of the interaction forces on the position,

the system never achieves full or ideal steady-state. On "long" timescales, however, the change in the velocity become very small. Figure 5.10 (right) displays results for dislocation separation along the twin at the end of the simulation ($t^* = 2.4 \times 10^4$). As expected, the dislocations at the twin tip are much closer together. V- and PN-based results are again in agreement with each other.

5.5.3 Effects of loading and twin thickness

Lastly, consider the dependence of dynamic dislocation separation on external loading and twin thickness. To this end, three loading cases ($\tau = 400$, 600 and 800 MPa) and three twin nucleus sizes ($N = 10$, 20 and 30) are considered. The corresponding simulation results are shown in Figure 5.11. As expected,

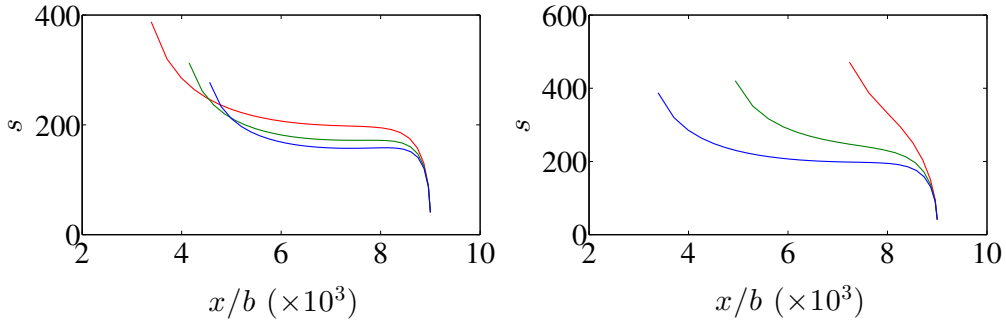


Figure 5.11: Left: effect of external loading on dislocation separation s as a function of dislocation position x/b. All cases with $N = 30$ dislocations. Red, green and blue curves corresponding to $\tau = 400$, 600 and 800 MPa, respectively. Right: effect of twin thickness on dislocation separation. All cases are under same external loading of $\tau = 400$ MPa. Red, green and blue curves correspond to $N = 10$, 20 and 30, respectively.

higher external loading reduces the dislocation separation (left). In addition, the separation at the twin tip is significantly smaller than the middle of the twin. Interestingly, the effect of external loading on the first three dislocation separations (between the first four dislocations) at the twin tip is negligible. All the three cases here are based on $N = 30$.

Figure 5.11 (right) shows the effects of twin thickness on dislocation separation. In this figure, red, green and blue curves correspond to $N = 10$, 20 and 30, respectively, all under same loading of $\tau = 400$ MPa. Again the first few dislocations at the twin tip have the same spacing regardless of N. However, the profile of the separation changes dramatically as N is changed. Increasing N introduces a region of almost uniform spacing (blue curve in Figure 5.11 right) with variable spacing at the two sides of the twin (i.e. the tip and middle of twin). However, this region of almost uniform spacing is non existence in the case of $N = 10$, the red curve.

5.6 Conclusion

The current work is concerned with the formulation of models for the energetics (statics) and kinetics (dynamics) of dislocation-mediated bulk twin nucleation and growth in fcc materials. To this end, both

the Peierls-Nabarro (PN) and Volterra (V) dislocation models are employed; in the process, a detailed comparison of the two is carried out. In particular, the PN-based energy model formulation relies on recent results (Schoeck 2014) for the interaction energy of straight Peierls dislocations and dipoles. In particular, these models are employed to determine the critical stress for bulk twin formation and growth in general fcc systems, and in particular for Al and Cu. Since any influence of the core becomes negligible as the separation between dislocations increases, the V- and PN-based models for the critical growth stress are basically equivalent. On the other hand, the two differ qualitatively in their predictions of the critical stress for partial dislocation (twin) nucleation. Indeed, in the V case, this stress is unphysical (infinity), in contrast to the finite critical stress predicted by the PN model.

The extension of the energy model to dynamics as based on relaxational "overdamped" dislocation motion mediated by mobility in the second part of the work has been applied to the modeling of variable dislocation separation in the twin. As expected, dislocations are closely packed together at the twin tip while the dislocations near the end of twin are farther away from each other. Generally, increasing the external loading, reduces the dislocation separation without altering the qualitative shape of the separation profile. Based on the calculations, changing the twin thickness (i.e. number of partial dislocation) changes the dislocation separation profile substantially. In case of thick twins (more than 30 dislocations), a region with nearly uniform spacing is distinguishable in the middle of the twin while this region is not visible in thin twins (less than 10 dislocations).

CHAPTER 6

PHASE FIELD BASED DISLOCATION MODELING*

"A rocket will never be able to leave the earth's atmosphere."
-The New York Times, 1936

6.1 Introduction

As attested to by theory (e.g., Hirth & Lothe 1982), atomistic simulation (e.g. Swygenhoven et al. 2006), and experiment (e.g., HRTEM), the energetically favored state of a dislocation line or loop in close-packed metals is its dissociated state, consisting of leading and trailing partial dislocations bounding, and separated by, a stacking fault (SF). The details of this configuration are dynamic in nature. In particular, the size of the stacking fault depends on the force balance between the long-range stress-field-based repulsion of the leading and trailing partials, the short-range attraction resulting from the energy cost of increasing the SF size, and any external loading forces. On the material side, then, the energy needed to create an SF in a given material, i.e., the stacking fault energy (SFE), plays a predominant role. In particular, the relation of the SFE to the level of loading is decisive in determining whether or not in a given material SFs shrink to their equilibrium size or continue to grow dynamically during loading. This in turn may influence a number of other dislocation processes such as core reactions, dislocation-based structural transformation (e.g., martensite formation), dislocation-based twinning, cross slip, and network formation (e.g., Hirth & Lothe 1982).

In order to model the energetics and kinetics of such dissociation-based dislocation processes, at least two approaches have been developed in the literature (for a comprehensive review, see Wang & Li 2010). The first approach (e.g., Xiang et al. 2008, Hunter et al. 2011, 2013, Shen et al. 2014) is based on various

*This chapter is based on the work in Mianroodi & Svendsen (2015)

generalizations of the Peierls-Nabarro (PN) dislocation model (e.g., Hirth & Lothe 1982, Mura 1987, Wang & Li 2010). The second approach (e.g., Shen & Wang 2003, 2004), to which the current work belongs, is based on the "interface" energy model and concept of Cahn & Hilliard (1958); for simplicity, it will be referred to here as the phase field[†] (PF) model. In both approaches, the free energy is modeled on contributions from lattice strain (elastic) and from lattice resistance to dislocation motion via homogeneous ("rigid") atomic displacement across the slip plane; in particular, the latter is associated with the (generalized) SFE (e.g., Vitek 1968). The PF model accounts in addition for a "gradient" contribution ("correction") to energy storage due to non-homogeneous atomic displacement across the slip plane, e.g., in the dislocation core. In both approaches, the elastic energy is based on (or at least consistent with) the Khachaturyan-Shalatov approach (e.g., Khachaturyan 1983, Wang et al. 2001) for periodic defective systems in which defects are modeled via their (residual) strain fields. Basically following Schoeck (2001, 2003, 2005), Shen & Wang (2004) modeled the SFE via a truncated Fourier series[*] parameterized by the phase fields. In particular, they fit this to DFT data on the SFE for Al and Pd. The only undetermined material property in their model is the gradient energy coefficient. In contrast, in the current work, the SFE and gradient energy are determined simultaneously and completely in a material-dependent fashion using atomistic energy and core morphology (e.g., size) data; no adjustable parameters remain. To this end, the global energy scaling approach of Cahn & Hilliard (1958) is exploited in this work to connect (discrete) atomistic and (continuum) PF modeling of dislocation processes. For simplicity, this is based here on an atomic potential and molecular statics; alternatively, *ab initio* (i.e., DFT-based) methods can be used.

The work begins in Section 6.2 with a synopsis of basic model relations and in particular the PF free energy model. This is followed in Section 6.3 by the reformulation of this model in a form amenable to atomistic or *ab initio* determination as discussed above via global energy scaling. To demonstrate its use, the resulting approach is applied to the atomistic determination of the PF free energy for Al and Cu in Section 6.4. For simplicity, this is carried out here with the help of an atomic potential in the context of molecular statics (MS); as mentioned above, ab initio DFT data can also be employed. After verification, these atomistically determined PF models for Al and Cu are then applied in Section 6.5 to the modeling of dislocation dissociation, SF formation, dislocation slip, and reactions in these materials the context of the tensile loading of a dislocation loop. In the process, connection is made with the dislocation (line) mechanics as based on Peach-Köhler force (PKF). The work ends in Section 6.6 with a summary and discussion. For completeness, selected details of the algorithm employed for the numerical solution of the current model in the simulations are provided in Appendix 6.A. As well, details concerning the relation between thermodynamic driving forces and the PKF are summarized in Appendix 6.B. For simplicity, attention is restricted to infinite periodic fcc systems and purely bulk behavior in this work.

Before we begin, a word on notation. In this work, (three-dimensional) Euclidean vectors are represented by lower-case bold italic characters $\boldsymbol{a}, \boldsymbol{b}, \ldots$, and second-order Euclidean tensors by upper-case bold italic characters $\boldsymbol{A}, \boldsymbol{B}$, etc.; in particular, $\boldsymbol{I}$ is the second-order identity tensor. Third- and fourth-order Euclidean tensors in this work are denoted by upper-case slanted sans-serif characters A, B, and so on. The notation $\boldsymbol{a} \cdot \boldsymbol{b}$, $\boldsymbol{A} \cdot \boldsymbol{B}$, and so on, is used for the scalar product of the corresponding tensors. Let $(\boldsymbol{a} \otimes \boldsymbol{b})\boldsymbol{c} := (\boldsymbol{b} \cdot \boldsymbol{c})\boldsymbol{a}$ define the tensor or dyadic product of $\boldsymbol{a}, \boldsymbol{b}$ as usual. Further, let $\operatorname{sym} \boldsymbol{A} := \frac{1}{2}(\boldsymbol{A} + \boldsymbol{A}^{\mathrm{T}})$ represent the symmetric part of any second-order tensor $\boldsymbol{A}$. Additional notation will be introduced as needed in what follows.

[†]This terminology is not uniform in the literature; for example, Hunter et al. (2011, 2013) refer to their model as a phase field model.

[*]Such a truncated Fourier-series representation of this energy is also employed by Xiang et al. (2008), Hunter et al. (2011, 2013) and Shen et al. (2014).

6.2 Basic model relations

For simplicity, the current formulation is restricted to single-constituent materials, isothermal conditions, quasi-static loading, and geometric linearity. Again for simplicity, attention is restricted here to single crystals and purely bulk behavior. Under these conditions, consider an inhomogeneous single crystal in which the inhomogeneity results from interacting material defects resulting in residual strain and stress states. Of particular interest in this work is the case of dislocations. Let $\boldsymbol{u}$ represent the displacement field, $\boldsymbol{H} = \nabla \boldsymbol{u}$ the distortion field, and $\boldsymbol{E} = \operatorname{sym} \nabla \boldsymbol{u}$ the strain field. Following many authors (e.g., Kröner 1959, Eshelby 1970, Khachaturyan 1983, Mura 1987, Wang et al. 2001, Li & Wang 2008), let

$$\psi_{\mathrm{E}} = \frac{1}{2} (\boldsymbol{E} - \boldsymbol{E}_{\mathrm{R}}) \cdot \mathsf{C}_{\mathrm{E}} (\boldsymbol{E} - \boldsymbol{E}_{\mathrm{R}}) \tag{6.1}$$

represent the density of stored energy in the single crystal due to lattice deformation determining in particular the corresponding energetic stress

$$\boldsymbol{T} = \partial_{\boldsymbol{E}} \psi_{\mathrm{E}} = \mathsf{C}_{\mathrm{E}} (\boldsymbol{E} - \boldsymbol{E}_{\mathrm{R}}) \, . \tag{6.2}$$

Here, C_{E} is the (constant isothermal) elastic stiffness, and $\boldsymbol{E}_{\mathrm{R}} = \operatorname{sym} \boldsymbol{H}_{\mathrm{R}}$ the residual strain due to defects. Restricting attention to fcc glide dislocations and dislocation slip (i.e., no climb), the corresponding distortion field

$$\boldsymbol{H}_{\mathrm{R}}(\boldsymbol{\phi}) = \sum_{a=1}^{p} \phi_a \, \boldsymbol{H}_a \tag{6.3}$$

is modeled as a sum of p (constant isothermal) elementary contributions

$$\boldsymbol{H}_a = \boldsymbol{b}_a \otimes \boldsymbol{n}_a / d_a = \gamma_a \, \boldsymbol{s}_a \otimes \boldsymbol{n}_a \, , \tag{6.4}$$

each weighted by corresponding phase field ϕ_a. Here, $\gamma_a := b_a / d_a$, $b_a := |\boldsymbol{b}_a|$, $\boldsymbol{s}_a := \boldsymbol{b}_a / b_a$, $\boldsymbol{b}_a$ is the Burgers vector, $d_a = d_{111} = a_0 / \sqrt{3}$ is the $\{111\}$ interplanar spacing, a_0 is the lattice constant, and $\boldsymbol{n}_a$ is the slip plane unit normal. Each ϕ_a models the transition between different states of slip in the energy landscape of the single crystal (more on this below). These fields are modeled such that $\boldsymbol{H}_{\mathrm{R}}$ vanishes everywhere in the material except on slipped surfaces (i.e., has "support" only on such surfaces).

Following Schoeck (2001) and Bulatov & Cai (2006, Chapter 11), the current approach is based on two ϕ_a per plane. Besides being computationally more efficient than three such fields per plane (as done for example by Shen & Wang 2004), this facilitates the model investigation of processes based on perfect $\langle 110 \rangle$ or (Shockley) partial $\langle 112 \rangle$ dislocations alone. As an example of such PFs, consider those ϕ_1 and ϕ_2 for the (111) plane as shown in Figure 6.1. Given two PFs per $\{111\}$ plane, we have $p = 8$ PFs for general octahedral slip in an fcc single crystal. In particular, both straight dislocation lines and dislocation loops (e.g., Eshelby 1961, Bulatov & Cai 2006, Chapter 11) can be modeled in this fashion.

Under quasi-static loading conditions, the timescale for "displacive" deformation of the lattice is assumed to be much shorter than that for "diffusive" deformation due to the motion of defect systems. As such, the lattice is able to react "instantaneously" to such motion and maintain mechanical equilibrium

$$\operatorname{div} \boldsymbol{T} = \boldsymbol{0} \, . \tag{6.5}$$

Idealizing dislocation motion as "overdamped" and relaxational in nature, the evolution or dynamics of each ϕ_a is modeled via the (time-dependent) Ginzburg-Landau relation

$$\dot{\phi}_a = -m_0 \, \delta_{\phi_a} \psi = m_0 \, (\operatorname{div} \partial_{\nabla \phi_a} \psi - \partial_{\phi_a} \psi) \tag{6.6}$$

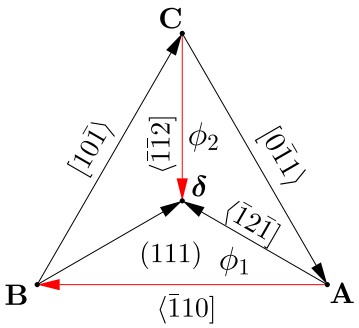


Figure 6.1: Shear directions (red arrows) on the (111) plane associated with the PFs ϕ_1 and ϕ_2 depicted on the (111) side of the Thompson tetrahedron. As shown, ϕ_1 is associated with simple shear strain $\boldsymbol{E}_1 = \gamma_1 \operatorname{sym}(\boldsymbol{s}_1 \otimes \boldsymbol{n}_1)$ for perfect slip $\boldsymbol{s}_1 \equiv [\bar{1}10]/\sqrt{2}$, and ϕ_2 with that $\boldsymbol{E}_2 = \gamma_2 \operatorname{sym}(\boldsymbol{s}_2 \otimes \boldsymbol{n}_2)$ for partial slip $\boldsymbol{s}_2 \equiv [\bar{1}\bar{1}2]/\sqrt{6}$, with $\boldsymbol{n}_1 = \boldsymbol{n}_2 \equiv [111]/\sqrt{3}$. In addition, note that $\gamma_1 = b_1/d_{111} = \sqrt{3}/\sqrt{2}$ and $\gamma_2 = b_2/d_{111} = 1/\sqrt{2}$ via $b_1 = a_0/\sqrt{2}$, $b_2 = a_0/\sqrt{6}$ and $d_{111} = a_0/\sqrt{3}$.

subject to no-flux (periodic) boundary conditions

$$\partial_{\nabla\phi_a}\psi \cdot \boldsymbol{n} = 0 \tag{6.7}$$

for each system a. Non-negative mobility $m_0 \geqslant 0$ (assumed constant and equal for all $a = 1, \ldots, 8$ for simplicity) insures non-negative dissipation and gradient flow of the system toward thermodynamic equilbrium.

The basic model relations are completed by the form

$$\psi(\nabla\boldsymbol{u}, \boldsymbol{\phi}, \nabla\boldsymbol{\phi}) = \psi_{\mathrm{E}}(\nabla\boldsymbol{u}, \boldsymbol{\phi}) + \psi_{\mathrm{C}}(\boldsymbol{\phi}, \nabla\boldsymbol{\phi}) \tag{6.8}$$

for the total free energy density ψ of the single crystal, with ψ_{C} its "chemical" part, and $\boldsymbol{\phi} := (\phi_1, \ldots, \phi_p)$. In particular, in the context of the local gradient, or interface, approximation of Cahn & Hilliard (1958), this latter is modeled as the sum

$$\psi_{\mathrm{C}}(\boldsymbol{\phi}, \nabla\boldsymbol{\phi}) = \psi_{\mathrm{H}}(\boldsymbol{\phi}) + \psi_{\mathrm{G}}(\nabla\boldsymbol{\phi}) \tag{6.9}$$

of "homogeneous" ψ_{H} and "gradient" ψ_{G} parts. As already mentioned above, the current choice of PFs as depicted in Figure 6.1 simplifies the modeling of $\langle 110\rangle$ perfect slip and $\langle 112\rangle$ partial slip on $\{111\}$ planes. From a physical point of view, perfect dislocation slip (on multiple planes) results in no atomic restacking and so preserves lattice orientation. On the other hand, partial dislocation slip is accompanied by SF formation; such slip on successive $\{111\}$ planes results in atomic restacking and lattice reorientation or even transformation (e.g., Hirth & Lothe 1982, Christian & Mahajan 1995). In this way, ψ_{C}, and in particular ψ_{H}, becomes associated with the energy needed to create, or stored in, stacking faults, i.e., the (generalized) SFE (e.g., Vitek 1968). Indeed, as discussed above, ψ_{H} is associated with the homogeneous ("rigid") displacement of atoms across $\{111\}$ planes due to dislocation slip. To account for the fact that such atomic displacement is in fact inhomogeneous, especially in the region around the dislocation core, ψ depends as well on ψ_{G}. More generally, ψ_{G} also accounts for the influence of properties such as bonding type (Schoeck 2005, 2006, Wang & Li 2010). Since the current work is restricted to dislocation slip, the dependence of ψ_{G} on $\nabla\boldsymbol{\phi}$ at the single crystal level is "parameterized" by the Nye measure

$\mathrm{curl}\,\boldsymbol{H}_{\mathrm{R}}$, which projects $\nabla\boldsymbol{\phi}$ onto the slip systems. Indeed, from (6.3) and (6.4),

$$\mathrm{curl}\,\boldsymbol{H}_{\mathrm{R}} = \sum_{a=1}^{p} \gamma_a\, \boldsymbol{s}_a \otimes \nabla\phi_a \times \boldsymbol{n}_a = \sum_{a=1}^{p} \gamma_a \left\{ (\nabla_{\boldsymbol{t}_a}\phi_a)\, \boldsymbol{s}_a \otimes \boldsymbol{s}_a - (\nabla_{\boldsymbol{s}_a}\phi_a)\, \boldsymbol{s}_a \otimes \boldsymbol{t}_a \right\} \tag{6.10}$$

depends only on the slip plane "components" $\nabla_{\boldsymbol{s}_a}\phi_a = \nabla\phi_a \cdot \boldsymbol{s}_a$ and $\nabla_{\boldsymbol{t}_a}\phi_a = \nabla\phi_a \cdot \boldsymbol{t}_a$ of $\nabla\phi_a$. Here, $\boldsymbol{t}_a = \boldsymbol{n}_a \times \boldsymbol{s}_a$ and $(\boldsymbol{s}_a, \boldsymbol{t}_a, \boldsymbol{n}_a)$ an orthogonal right-hand system. For example, $\boldsymbol{t}_1 \equiv [111]/\sqrt{3} \times [\bar{1}10]/\sqrt{2} = [\bar{1}\bar{1}2]/\sqrt{6} \equiv \boldsymbol{s}_2$ and $\boldsymbol{t}_2 \equiv [111]/\sqrt{3} \times [\bar{1}\bar{1}2]/\sqrt{6} = [1\bar{1}0]/\sqrt{2} \equiv -\boldsymbol{s}_1$ for the (111) glide plane as discussed above in the context of Figure 6.1. On this basis, ψ_{G} is modeled here for simplicity by the ubiquitous quadratic form

$$\psi_{\mathrm{G}}(\nabla\boldsymbol{\phi}) = \psi_{\mathrm{G}0}\,|\mathrm{curl}\,\boldsymbol{H}_{\mathrm{R}}|^2 = \psi_{\mathrm{G}0} \sum_{a,b=1}^{p} \nabla\phi_a \cdot \boldsymbol{N}^g_{ab} \nabla\phi_b\,, \tag{6.11}$$

with

$$\boldsymbol{N}^g_{ab} := \gamma_a\gamma_b\,(\boldsymbol{s}_a \cdot \boldsymbol{s}_b)\left\{(\boldsymbol{n}_a \cdot \boldsymbol{n}_b)\,\boldsymbol{I} - \boldsymbol{n}_b \otimes \boldsymbol{n}_a\right\}. \tag{6.12}$$

Note that the scaling factor $\psi_{\mathrm{G}0}$ has unit of energy per unit length. If interactions among distinct slip systems ($a \neq b$) are neglected, (6.11) reduces to the relation considered for example by Bulatov & Cai (2006, Equation (11.34)).

Since we are interested in purely bulk behavior of fcc single crystals in this work, attention is restricted to periodic fields and systems, and Fourier transform methods are applicable for solution of initial boundary value problems based on (6.5)-(6.7) as usual (e.g., Khachaturyan 1983, Mura 1987, Suquet 1997, Nemat-Nasser & Hori 1999, Li & Wang 2008). Both general, algorithmic and numerical details in this regard are summarized for completeness in Appendix 6.A.

6.3 Model formulation based on energy scaling

As discussed in the introduction, the determination of the PF free energy with the help of atomistic methods in this work is based on adaptation of the interface energy and scaling approach of Cahn & Hilliard (1958) to the current case. To this end, a characteristic process is chosen which is amenable to both atomistic (here molecular static; MS) and PF modeling. To this end, consider the dissociation

$$\begin{array}{ccccc} \mathbf{AB} & \longrightarrow & \mathbf{A}\boldsymbol{\delta} & + & \boldsymbol{\delta}\mathbf{B} \\ \frac{a_0}{2}[\bar{1}10] & \longrightarrow & \frac{a_0}{6}[\bar{1}2\bar{1}] & + & \frac{a_0}{6}[\bar{2}11] \end{array} \tag{6.13}$$

of a single perfect screw dislocation in the (111) plane with Burgers vector $\mathbf{AB} = \frac{a_0}{2}[\bar{1}10]$, a_0 being the lattice constant. In terms of (ϕ_1, ϕ_2) in Figure 6.1, note that $\mathbf{AB} \equiv (1, 0)$, $\mathbf{A}\boldsymbol{\delta} \equiv (\frac{1}{2}, -\frac{1}{2})$, and $\boldsymbol{\delta}\mathbf{B} \equiv (\frac{1}{2}, \frac{1}{2})$. For the formulation to follow, it proves useful to work with the related Cartesian basis system

$$\boldsymbol{i}_x \equiv [\bar{1}\bar{1}2]/\sqrt{6}\,, \quad \boldsymbol{i}_y \equiv [111]/\sqrt{3}\,, \quad \boldsymbol{i}_z \equiv [\bar{1}10]/\sqrt{2}\,. \tag{6.14}$$

Being a screw dislocation, $\mathbf{AB}$ then has line direction $\boldsymbol{i}_z$. Further, $\mathbf{A}\boldsymbol{\delta} = -\frac{1}{2}\,b_{112}\,\boldsymbol{i}_x + \frac{1}{2}\,b_{110}\,\boldsymbol{i}_z$ and $\boldsymbol{\delta}\mathbf{B} = \frac{1}{2}\,b_{112}\,\boldsymbol{i}_x + \frac{1}{2}\,b_{110}\,\boldsymbol{i}_z$ then hold relative to (6.14), with $b_{110} = a_0/\sqrt{2}$ and $b_{112} = a_0/\sqrt{6}$. Likewise, $\boldsymbol{n}_1 = \boldsymbol{n}_2 = \boldsymbol{i}_y$, $\boldsymbol{s}_1 = \boldsymbol{i}_z$, $\boldsymbol{s}_2 = \boldsymbol{i}_x$, $\boldsymbol{t}_1 = \boldsymbol{s}_2 = \boldsymbol{i}_x$, and $\boldsymbol{t}_2 = -\boldsymbol{s}_1 = -\boldsymbol{i}_z$. In addition, ϕ_2 is then associated with $\boldsymbol{i}_x$, and ϕ_1 with $\boldsymbol{i}_z$. So set $\phi_x = \phi_2$ and $\phi_z = \phi_1$ in what follows.

Adapting now the approach of Cahn & Hilliard (1958) to the current case of a single (111) slip plane, the relation

$$\begin{aligned} \psi_{\rm EH}(\phi_x,\phi_z) - \psi_{\rm EH}(0,0) &= \Delta\psi_{\rm EH}(\phi_x,\phi_z) \\ &= \psi_{\rm G}(\nabla\phi_x,\nabla\phi_z) \\ &= \tfrac{1}{2}\,\psi_{\rm G0}\,|\nabla_{\boldsymbol{i}_x}\phi_x|^2 + \tfrac{3}{2}\,\psi_{\rm G0}\,|\nabla_{\boldsymbol{i}_x}\phi_z|^2 \end{aligned} \tag{6.15}$$

is obtained in equilibrium between the effective homogeneous*

$$\psi_{\rm EH}(\phi_x,\phi_z) := \psi_{\rm E}(\phi_x,\phi_z) + \psi_{\rm H}(\phi_x,\phi_z)\,, \tag{6.16}$$

and gradient $\psi_{\rm G}(\nabla\phi_x,\nabla\phi_z)$, parts of ψ from (6.8) reduced to the current case of a single (111) slip plane. In particular, (6.15) follows from solution of the Ginzburg-Landau relation (6.6) in equilbrium ($\dot{\phi}_a = 0$) for $a = x, z$, taking into account the fact that $\nabla_{\boldsymbol{i}_z}\phi_x$ and $\nabla_{\boldsymbol{i}_z}\phi_z$ along the line direction $\boldsymbol{i}_z$ vanish for straight lines. Given (6.1) and (6.3), note that $\psi_{\rm E}(0,0) = \frac{1}{2}\,\boldsymbol{E}\cdot\boldsymbol{C}_{\rm E}\boldsymbol{E}$ is the free energy density of a crystal without defects. Since $\psi_{\rm H}(0,0) = 0$ can be assumed without loss of physical generality, $\psi_{\rm EH}(0,0) = \psi_{\rm E}(0,0) = \frac{1}{2}\,\boldsymbol{E}\cdot\boldsymbol{C}_{\rm E}\boldsymbol{E}$ holds as well. To proceed further, it is useful to work with the transformations

$$\boldsymbol{i} = \frac{1}{\sqrt{2}}\boldsymbol{i}_x + \frac{1}{\sqrt{2}}\boldsymbol{i}_z\,, \quad \phi\,\boldsymbol{i} = \phi_x\,\boldsymbol{i}_x + \phi_z\,\boldsymbol{i}_z\,, \quad \phi_x(\phi) = \frac{1}{\sqrt{2}}\,\phi\,, \quad \phi_z(\phi) = \frac{1}{\sqrt{2}}\,\phi\,. \tag{6.17}$$

From these follow the reduced form

$$\psi_{\rm H0}\,\Delta f_{\rm EH}(\phi) := \Delta\psi_{\rm EH}(\phi_x(\phi),\phi_z(\phi)) = \psi_{\rm G0}\,|\partial_x\phi|^2 \tag{6.18}$$

of (6.15) with $\partial_x\phi = \nabla_{\boldsymbol{i}_x}\phi$. Here, $\Delta f_{\rm EH}(\phi)$ represents the functional form of $\Delta\psi_{\rm EH}(\phi_x(\phi),\phi_z(\phi))$, and $\psi_{\rm H0}$ is an energy scaling parameter. In turn, (6.18) implies

$$|\partial_x\phi| = \sqrt{\frac{\psi_{\rm H0}}{\psi_{\rm G0}}}\,\sqrt{\Delta f_{\rm EH}(\phi)} \tag{6.19}$$

for the (magnitude of the) equilibrium PF gradient.

Consider next a region P of the single crystal containing the slip plane in the form of a retangular parallelepiped infinitely long in the $\boldsymbol{i}_x$ direction and having finite constant cross section perpendicular to x with area a_P. Let

$$g_0 := \int_{-\infty}^{\infty}\psi\;dx = \frac{1}{a_P}\int_P \psi\;dv \tag{6.20}$$

represent the stored energy per unit cross sectional area. In equilibrium, this takes the form

$$g_0 = \kappa_{\rm H0}\,\sqrt{\psi_{\rm H0}\psi_{\rm G0}}\,, \quad \kappa_{\rm H0} := \int_{\phi(-\infty)}^{\phi(+\infty)} \frac{f_{\rm EH}(\phi) + \Delta f_{\rm EH}(\phi)}{\sqrt{\Delta f_{\rm EH}(\phi)}}\;d\phi \tag{6.21}$$

via (6.18) and (6.19). Again following Cahn & Hilliard (1958), consider next the model relation

$$l_0 := \frac{\phi(+\infty) - \phi(-\infty)}{|\partial_x\phi(0)|} \tag{6.22}$$

for the "width" of the interface region. In the current context, the interface is identified with the dislocation core, and l_0 with the core size. Substitution of $\partial_x\phi(0)$ from (6.19) (assumed positive) into (6.22) yields

$$l_0 = \kappa_{\rm G0}\,\sqrt{\frac{\psi_{\rm G0}}{\psi_{\rm H0}}}\,, \quad \kappa_{\rm G0} := \frac{\phi(+\infty) - \phi(-\infty)}{\sqrt{\Delta f_{\rm EH}(\phi(0))}}\,. \tag{6.23}$$

*For simplicity, $\boldsymbol{E}$ is left out of the notation here.

Lastly, combination of (6.21) and (6.23) results in the forms

$$\psi_{\mathrm{H0}} = \frac{\kappa_{\mathrm{G0}}}{\kappa_{\mathrm{H0}}}\,\frac{g_0}{l_0}\,, \quad \psi_{\mathrm{G0}} = \frac{1}{\kappa_{\mathrm{G0}}\kappa_{\mathrm{H0}}}\,g_0 l_0\,, \tag{6.24}$$

for the material parameters scaling $\psi_{\mathrm{EH}} = \psi_{\mathrm{E}} + \psi_{\mathrm{H}}$ and ψ_{G}, respectively, in ψ from (6.8) and (6.9). As is well-known (e.g., Bulatov & Cai 2006), the mobility m_0 can be determined as well atomistically via molecular dynamics (MD). Since the focus of the current work is on energetics, however, this is not done here. Note that the corresponding scaled form $\dot{\phi}_a = -m_0\psi_{\mathrm{H0}}\,\delta_{\phi_a}\,\psi/\psi_{\mathrm{H0}}$ of (6.6) implies that the mobility m_0 is scaled by ψ_{H0} as well.

In the next section, the elastic stiffness C_{E} and so ψ_{E}, as well as ψ_{H}, g_0, and l_0, are all determined from an atomic potential via MS. In particular, the SFE contribution ψ_{H} is obtained from $\psi_{\mathrm{H}}^{\langle 111\rangle}(\phi_1,\phi_2)$ and material symmetry. These determine in turn $\psi_{\mathrm{EH}} = \psi_{\mathrm{E}} + \psi_{\mathrm{H}}$, and so κ_{H0} from (6.21). Further, since $\phi_{x,z}(-\infty) = 0$ and $\phi_{x,z}(+\infty) = 1/2$, note that $\phi(-\infty) = 0$ and $\phi(+\infty) = 1/\sqrt{2}$ via (6.17) are known for the case of dissociation considered above. Then κ_{G0} follows as well from (6.23). Given all of these, ψ_{H0} and ψ_{G0} follow from (6.24), and ψ is completely determined.

6.4 Atomistic identification of the PF free energy model

For comparison, the fcc materials Al and Cu are considered here. Besides different lattice and elastic properties, these are characterized by having different SFEs. Calculation of all energetic properties of the PF model discussed in the previous sections for these materials is based here on the corresponding embedded atom potentials from Mishin et al. (1999) for Al and Mishin et al. (2001) for Cu, both at zero temperature. These potentials are widely used and in close agreement with DFT and experimental results (e.g., Zimmerman et al. 2000) for the material properties of interest in this work.

6.4.1 Basic properties & ψ_{E}

Values for the lattice constant and elastic stiffnesses of Cu and Al are summarized in Table 6.1. Besides

	a_0 [Å]	C_{11} [GPa]	C_{12} [GPa]	C_{44} [GPa]
Cu	3.615	169.9	122.6	76.2
Al	4.050	113.8	61.5	31.6

Table 6.1: Zero-temperature (isothermal) lattice constant a_0 and fcc elastic constants C_{11}, C_{12}, C_{44}, for Cu and Al calculated from the embedded atom potentials of Mishin et al. (2001) (Cu) and of Mishin et al. (1999) (Al) using the LAMMPS molecular dynamics package (Plimpton 1995).

C_{E}, the material property values in Table 6.1 determine the effective fcc shear modulus $\mu_{\mathrm{fcc}} = (C_{11} - C_{12} + 3C_{44})/5$, the corresponding Poisson's ratio $\nu_{\mathrm{fcc}} = (C_{11} + 4C_{12} - 2C_{44})/(4C_{11} + 6C_{12} + 2C_{44})$, as well as $d_{111} = a_0/\sqrt{3}$, $b_{110} = a_0/\sqrt{2}$ and $b_{112} = a_0/\sqrt{6}$. Consequently, $\boldsymbol{b}_a$, γ_a and so $\boldsymbol{E}_a$ from (6.4), for $a = 1,\ldots,8$, are determined. In summary, all material parameters in ψ_{E} from (6.1), and so in the stress $\boldsymbol{T}$ from (6.2), are then determined atomistically.

6.4.2 Stacking fault energy ψ_{H}

As mentioned above, to model ψ_{H}, Shen & Wang (2004) fit DFT data to the analytical truncated Fourier series representation for this energy from Schoeck (2001, 2003, 2005). In contrast, a simple numerical scheme utilizing MS data is employed for this purpose here. Given this data, values for ψ_{H} and its PF derivatives are calculated in PF space and then used in look-up-table fashion during the PF simulation. This results in a speed-up of the calculation of ψ_{H} by about a factor of 4 in comparison to the Fourier-based approach. In addition, this avoids Fourier-series truncation errors and simplifies energy surface representation up to the desired accuracy.

As usual, calculation of the SFE via MS is based on rigid displacement and relaxation normal to the slip plane. The corresponding energy density $\psi_{\mathrm{H}}(\phi_1, \phi_2)$ with respect to the (111) plane (with ϕ_1 and ϕ_2 as in Figure 6.1) is shown in Figure 6.2 for Al (left) and Cu (middle). Calculation of the SFE surfaces shown

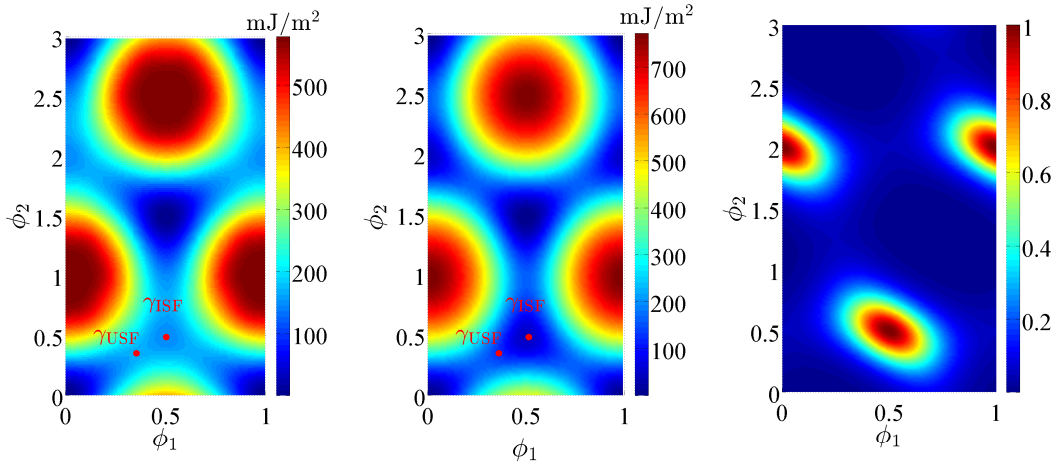


Figure 6.2: Left, middle: zero-temperature (isothermal) SFE surfaces $\psi_{\mathrm{H}}(\phi_1, \phi_2)$ corresponding to Figure 6.1 for Al (left) and Cu (middle) calculated from the corresponding embedded atom potentials of Mishin et al. (1999, 2001). The points γ_{USF} and γ_{ISF} represent the unstable and equilibrium energy states, respectively, of instrinsic SFs. Right: periodic function $f_{\mathrm{SF}}(\phi_1, \phi_2)$ from (6.25) used for detection and visualisation of SFs.

in Figure 6.2 employ PF-based parameterization of MS data using 100 points in the ϕ_1 direction, and 200 points in the ϕ_2 direction. Particular values of interest on the SFE surface include the equilibrium γ_{ISF} and unstable γ_{USF} values. For Cu, $\gamma_{\mathrm{ISF}} = 45.1$ mJ/m^2 and $\gamma_{\mathrm{USF}} = 163.4$ mJ/m^2. For Al, $\gamma_{\mathrm{ISF}} = 145.2$ mJ/m^2 and $\gamma_{\mathrm{USF}} = 168.2$ mJ/m^2. With $\psi_{\mathrm{H}}(\phi_1, \phi_2)$ in hand, $\psi_{\mathrm{H}}(\boldsymbol{\phi})$ is then determined via material symmetry.

In order to visualize SFs in the PF simulation results, it is necessary to define a function capable of detecting partial slip based on values of ϕ_1 and ϕ_2. The periodic function

$$f_{\mathrm{SF}}(\phi_1, \phi_2) = e^{-3\,\sin^2(\phi_1+\phi_2/3-2/3)\pi}\, e^{-3\,\sin^2(2\phi_2/3-1/3)\pi} \tag{6.25}$$

plotted in Figure 6.2 is used for this purpose. As shown, the value of $f_{\mathrm{SF}}(\phi_1, \phi_2)$ is 1 at the points where an intrinsic SF is located (see Figure 6.2, left and middle) and decreases toward zero as (ϕ_1, ϕ_2) deviate from SF states. Since this function is periodic, it works for all values of (ϕ_1, ϕ_2) (both negative and positive).

6.4.3 Energy scaling

With ψ_{E} and ψ_{H} determined as just discussed, κ_{H0} and κ_{G0} follow from (6.21) and (6.23), respectively, via (6.17) and numerical integration (again with $\phi(+\infty) - \phi(-\infty) = 1/\sqrt{2}$ from above). The values of these for Al and Cu are listed in Table 6.2. As discussed above, g_0 and l_0 are determined atomistically via

	$g_0/\mu_{\mathrm{fcc}} d_{111}$	l_0/d_{111}	κ_{H0}	κ_{G0}
Cu	0.055	6.289	0.429	0.479
Al	0.064	6.053	0.303	0.468

Table 6.2: Parameter values for Cu and Al determining the energy scaling relations (6.24). See text for details.

MS simulation of the dissociation (6.13) of 2 straight perfect screw dislocations in a dipole configuration. This results in the formation of 4 partial monopoles (i.e., 2 per perfect monopole). The corresponding simulation is carried out in a box with basis (6.14) and dimensions $(L_x, L_y, L_z) = (70\sqrt{6}, 60\sqrt{3}, 3\sqrt{2})\, a_0 = (420\, b_{112}, 180\, d_{111}, 6\, b_{110})$. The initial configuration is a perfect straight screw dipole on the (111) plane with line parallel to $\boldsymbol{i}_z$ centered at $(y, z) = (L_y/2, 0)$; the monopoles are located initially at $x = L_x/4$ and $x = 3L_x/4$. The displacement field of this dipole is imposed on the atoms using the method for periodic systems described by Bulatov & Cai (2006, Chapter 5). Relaxation to dissociation is carried out via the FIRE algorithm (Bitzek et al. 2006). Since the current implementation of this algorithm in LAMMPS does not include relaxation of the simulation box, this is followed by conjugate-gradient-based relaxation to equilibrium.

The atomic calculation of g_0 is based on the difference in energy between the equilibrium states of an fcc crystal containing (i) a single dissociated dipole and (ii) no dipole. To this end, consider the rectangular parallelepiped P of length $l_P = L_x$, width $w_P = L_z$, and height $h_P = 2\, d_{111}$ formed by the (111) planes at $y = L_y/2 \pm d_{111}$ enclosing the plane containing the cores of the 4 partial dislocations. Then $v_P = l_P\, w_P\, h_P = 2\, d_{111} L_x L_z$ and $a_P = w_P\, h_P = 2\, d_{111} L_z$. Let N represent the number of atoms in P, and ΔE_i the energy difference between the states of atom i in P with and without the dissociated dipole. Then

$$g_0 \equiv \frac{1}{a_P} \sum_{i=1}^{N} \tfrac{1}{4}\, \Delta E_i \tag{6.26}$$

determines the interface energy consistent with (6.20) for the current case. The factor of 4 in (6.26) due to the fact that P contains 4 dislocation cores (two partial pairs). Formally at least, $\frac{1}{4} \sum_{i=1}^{N} \Delta E_i / v_P$ is analogous to $\Delta\psi_{\mathrm{EH}}$ from (6.15) in the PF context.

The effective core size l_0 is calculated atomistically via the displacement of the atoms relative to their ideal fcc positions. In the current case of dipole dissociation in the (x, z) plane spanned by $\boldsymbol{i}_x \equiv [\bar{1}\bar{1}2]/\sqrt{6}$ and $\boldsymbol{i}_z \equiv [\bar{1}10]/\sqrt{2}$, the 4 partial dislocation cores are geometrically equivalent, and attention can be restricted to just one. Let u_x and u_z represent the displacement components of the atoms in the core region of interest relative to the ideal fcc lattice. These are used to calculate the corresponding disregistries $\phi_x = u_x/b_x$ and $\phi_z = u_z/b_z$. In turn, these determine ϕ from (6.17). Finally, this function and its derivative $\partial_x \phi(0)$ at $x = 0$ are used in (6.22) to calculate l_0.

To verify the results in Table 6.2, the entire dipole dissociation process is simulated for screw dislocations. The simulation box and initial dislocation configuration are the same as above. Figure 6.3 displays the resulting disregistry profiles for the screw case. The values of g_0 and l_0 obtained from the PF simulation results are respectively within 1% and 4% of the corresponding values from the MS simulation. To

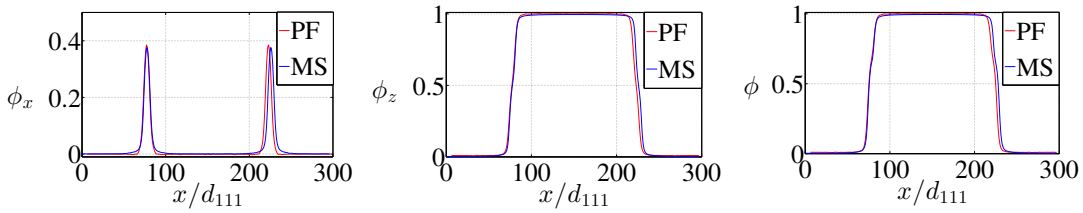


Figure 6.3: Disregistry profiles for a dissociated screw dipole in Cu along $\boldsymbol{i}_x \equiv [\bar{1}\bar{1}2]/\sqrt{6}$. Please note that the x-axis in these figures refers to the simulation box and not the dislocation line. In particular, $x = 0$ on this axis is different that the center of the dislocation $x = 0$ in (6.22) at which $\partial_x \phi(x)$ is evaluated.

validate the identified PF free energy model based on Table 6.2, edge dipole dissociation has also been simulated. In this case, the simulation box is defined by $\boldsymbol{i}_x \equiv [\bar{1}10]/\sqrt{2}$ and $\boldsymbol{i}_z \equiv [\bar{1}\bar{1}2]/\sqrt{6}$ instead of (6.14), and dimensions $(L_x, L_y, L_z) = (120\sqrt{2}, 60\sqrt{3}, 3\sqrt{6}/2)\, a_0 = (240\, b_{110}, 180\, d_{111}, 9\, b_{112})$. Corresponding results for Cu and Al in the case of edge dissociation are depicted in Figure 6.4. A further

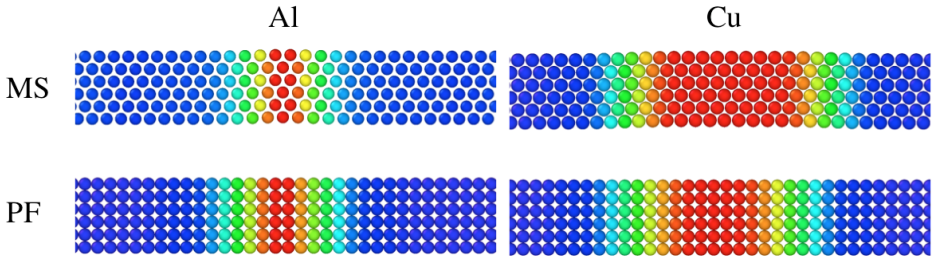


Figure 6.4: Disregistry fields associated with dissociated straight edge dislocations in Al (left) and Cu (right). Displayed is the displacement or disregistry component along the line, analogous to the disregistry profile in Figure 6.3 (middle). The MS results shown are superposed on the atomic lattice, and the PF results on the numerical grid. Ovito (Stukowski 2010) is used for both visualisations.

measure of comparison is the equilibrium SF width (Shen & Wang 2004, Xiang et al. 2008, Hunter et al. 2011). The equilibrium partial dislocation separation and SF width is given by the distance between the two peaks in the gradient of the disregistry (i.e., density) profiles, corresponding to the core positions of the two partials (see Figure 6.3). Selected results for Al and Cu are given in Table 6.3.

	edge [$\mathring{A}$]	screw [$\mathring{A}$]	source
Al	14.0	9.3	PF (this work)
	9.0	6.0	Hunter et al. (2011, 2013)
	12.1	7.4	MS (this work)
Cu	29.2	14.6	PF (this work)
	23.0	10.0	Hunter et al. (2011, 2013)
	37.5	13.4	MS (this work)

Table 6.3: Equilibrium SF widths for Al and Cu obtained from the current PF model and MS results compared with corresponding results from the PN model of Hunter et al. (2011, 2013). Because of its lower (intrinsic) SFE, the SF width in Cu is larger than that in Al. See text for details.

6.5 Application to tensile loading of a dislocation loop

As a simple application of the atomistically determined PF model developed in the previous sections, consider the simulation of tensile loading of a (initially) perfect dislocation loop on the (111) plane as shown in Figure 6.5 (left). The simulation box has dimensions of $120\, d_{111}$ in all directions. The

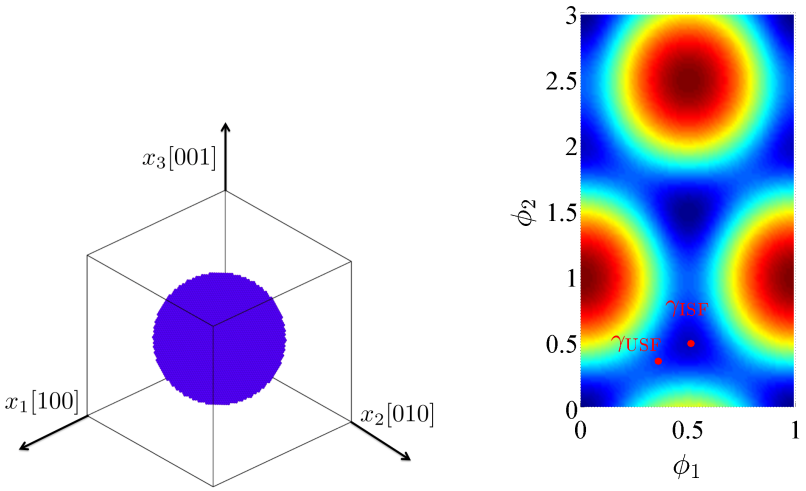


Figure 6.5: Left: initially perfect dislocation loop $(\phi_1, \phi_2) = (1, 0)$ of radius $r = 30\sqrt{2}\, d_{111}$ on (111). Right: SFE surface $\psi_{\mathrm{H}}(\phi_1, \phi_2)$ of Cu from Figure 6.2 (middle). The initial loop state $(\phi_1, \phi_2) = (1, 0)$ corresponds to $\mathbf{AB}$ in Figure 6.1 and in (6.13). See text for details.

corresponding results for the final state (ϕ_1, ϕ_2) of the loop after loading are shown in Table 6.4.

To interpret and understand these results, it is useful to examine the corresponding energy pathways traversed by the loop state in the corresponding (SF) energy landscape shown Figure 6.5 (right). As well, it is interesting to compare this energetic / thermodynamic picture with the classical purely mechanical force-based one in terms of the corresponding Peach-Köhler force (PKF). To do this in a meaningful fashion, it is necessary to establish the relation between the models for the Burgers vector tacitly assumed in the PF model via the residual distortion relation (6.3)-(6.4) and that in the PKF. This is done in Appendix 6.B and summarized in Figure 6.B.1. Given this, the glide component of the PKF from (6.37) is calcu-

		Stress magnitude (in units of μ_{fcc})					
		0.02	0.05	0.10	0.15	0.20	0.25
Al	T_{11}	(0,0)	(0,0)	(0,0)	(0,0)	(0,0)	(0,0)
	T_{22}	(0,0)	(1,0)	(1,0)	(1,0)	(1,0)	(1,0)
	T_{33}	(0,0)	(0,0)	(0,0)	(0.5,1.5)	(0.5,1.5)	(0.5,1.5)
Cu	T_{11}	(0,0)	(0,0)	(0,0)	(0,0)	(0,0)	(0,0)
	T_{22}	(0,0)	(1,0)	(1,0)	(1,0)	(1,0)	(1,0)
	T_{33}	(0,0)	(0.5,0.5)	(0.5,0.5)	(0.5,1.5)	(0.5,1.5)	(0.5,1.5)

Table 6.4: Final state (ϕ_1, ϕ_2) of the initially perfect loop (Figure 6.5, left) in Al and Cu subject to tensile loading. Here, T_{11}, T_{22}, and T_{33} are the stress components in the $[100]$, $[010]$, and $[001]$, directions, respectively (see Figure 6.5, left).

lated on each partial dislocation loop for the three loading cases in Table 6.4. The results are shown in Figure 6.6. Consider first the case of T_{11} loading in Table 6.4. As implied in Figure 6.6 (left), this results

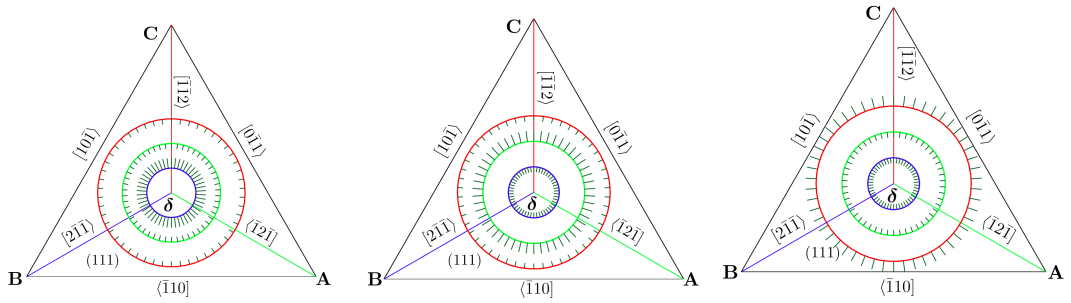


Figure 6.6: PKF on the three (111) partial dislocations depending on loading. Left: T_{11} loading. Middle: T_{22} loading. Right: T_{33} loading. Red: $[\bar{1}\bar{1}2\rangle$ partial. Green: $[\bar{1}2\bar{1}\rangle$ partial. Blue: $[2\bar{1}\bar{1}\rangle$ partial. Outward-directed (inward-directed) tick marks indicate an expansive (contractive) PKF; tick length indicates (relative) magnitude.

in contractive PKFs on the partials in the dissociation (6.13). Note that the PKF associated with $[2\bar{1}\bar{1}\rangle$ (i.e., $\mathbf{B}\boldsymbol{\delta}$: blue in Figure 6.6, left) is expansive; since the negative of this (i.e., $\boldsymbol{\delta}\mathbf{B}$) appears in the dissociation (6.13), however, the force changes sign. Consequently, such loading enhances the (contractive) loop self-stress at any loading level and results in its annihilation in both Cu and Al. The corresponding energy pathway from $(\phi_1, \phi_2) = (1, 0)$ to $(\phi_1, \phi_2) = (0, 0)$ in Figure 6.5 (right) traverses the intermediate state $(\phi_1, \phi_2) = (\frac{1}{2}, \frac{1}{2})$, as implied by (6.13). In contrast to this, T_{22} loading results in a PKF on both partials which is expansive, opposing as such the (contractive) self-stress. As shown in Table 6.4, below a value for T_{22} of $0.05\,\mu_{\text{fcc}}$, this opposing force is insufficient to prevent loop collapse. Above this level, however, T_{22} results in further expansion. In addition, the fact that the PKF is of different magnitude on the leading and trailing partials (see length of tick marks in Figure 6.6, center) leads to a deviation of the SF width from its equilibrium value. As already seen in Table 6.3, because of its lower (intrinsic) SFE, the SF width in Cu is larger than that in Al.

The most interesting of the three loading cases in Table 6.4 is the final case of T_{33} loading. As shown in Figure 6.6 (right), this results in an expansive PKF on $\boldsymbol{\delta}\mathbf{B}$ (blue) and a contractive PKF on $\mathbf{A}\boldsymbol{\delta}$ (green). As before, an expansive PKF works against the self-stress of the loop, and a contractive one enhances it. Consequently, if the level of loading is too low, the expansive PKF is insufficient to prevent loop annihilation. As the PKF on $\mathbf{A}\boldsymbol{\delta}$ and $\boldsymbol{\delta}\mathbf{B}$ is equal and opposite, the net PKF is approximately zero. In

terms of thermodynamic state (ϕ_1, ϕ_2), the results in Table 6.4 show that the initial state $(\phi_1, \phi_2) = (1, 0)$ transforms to $(\phi_1, \phi_2) = (0, 0)$ in both Al and Cu. The loop in Al remains in this state up to $T_{33} = 0.15\,\mu_{\text{fcc}}$, at which point it transforms to $(\phi_1, \phi_2) = (0.5, 1.5)$. On the other hand, the loop in Cu remains in this state up to $T_{33} = 0.05\,\mu_{\text{fcc}}$, where it transforms to $(\phi_1, \phi_2) = (0.5, 0.5)$. Note that this latter state represents an extended SF. Because Al has a relatively high SFE, this state is energetically unfavorable for the loop in Al. As shown by the results in Table 6.4, the next energetically favorable state for this loop is the perfect state $(\phi_1, \phi_2) = (0.5, 1.5)$ at $T_{33} = 0.15\,\mu_{\text{fcc}}$. As depicted in Figure 6.5 (right), from the geometric point of view, this is $\mathbf{CB}$. This can also be understood in terms of the respective PKFs on the partials involved by looking at the possible reaction

$$\mathbf{A}\boldsymbol{\delta} \;+\; \boldsymbol{\delta}\mathbf{B} \;\longrightarrow\; \mathbf{A}\boldsymbol{\delta} \;+\; \boldsymbol{\delta}\mathbf{C} \;+\; \mathbf{C}\boldsymbol{\delta} \;+\; \boldsymbol{\delta}\mathbf{B}\,. \tag{6.27}$$

Indeed, since the PKF on $\mathbf{A}\boldsymbol{\delta}$ and $\boldsymbol{\delta}\mathbf{C}$ is contractive, the sum of these is as well, and $\mathbf{AC}$ vanishes. On the other hand, $\mathbf{C}\boldsymbol{\delta}$ and $\boldsymbol{\delta}\mathbf{B}$ are expansive, resulting in expansion of $\mathbf{CB}$. For the case of Cu, as shown by Table 6.4, the extended SF state $(\phi_1, \phi_2) = (0.5, 0.5)$ at $T_{33} = 0.05\,\mu_{\text{fcc}}$ also transforms to the perfect state $(\phi_1, \phi_2) = (0.5, 1.5)$ at $T_{33} = 0.15\,\mu_{\text{fcc}}$. As in the case of Al, this represents the reaction (6.27). Because the SFE of Cu is lower, this does not result in the formation of perfect dislocations; rather, the partial-SF combinations $\mathbf{A}\boldsymbol{\delta} + \boldsymbol{\delta}\mathbf{C}$ and $\mathbf{C}\boldsymbol{\delta} + \boldsymbol{\delta}\mathbf{B}$ are favored. Since the PKF configuration is the same as in the case of Al, $\mathbf{A}\boldsymbol{\delta} + \boldsymbol{\delta}\mathbf{C}$ vanishes, and $\mathbf{C}\boldsymbol{\delta} + \boldsymbol{\delta}\mathbf{B}$ expands.

The evolution of loop state in both Al and Cu just discussed is displayed in Figure 6.7. The transition

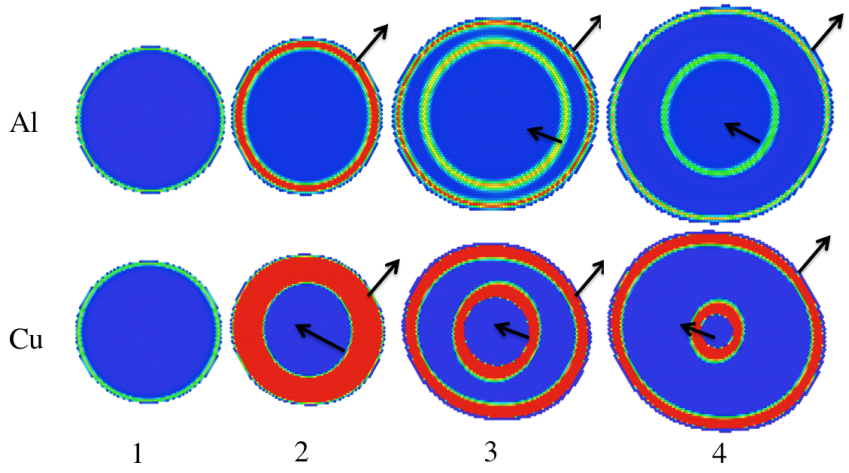


Figure 6.7: Stages of dynamic dislocation loop transformation in Al and Cu on (111) during T_{33} loading. Depicted are 4 intermediate stages during the transformation of the initial state $(\phi_1, \phi_2) = (1, 0)$ (Stage 1) to $(\phi_1, \phi_2) = (0.5, 1.5)$ (Stage 4) at $T_{33} = 0.15\,\mu_{\text{fcc}}$ as in Table 6.4. The black arrows indicate the direction of motion of the line. Blue: perfectly slipped crystal. Red: SF. Green: dislocation line. See text for details.

from Stage 1 (i.e., the intial state $(\phi_1, \phi_2) = (1, 0)$) to Stage 2 is the dissociation (6.13); that from Stage 2 to Stage 3 is the reaction (6.27). In going from Stage 3 to 4, further shrinkage of the inner partial loops, and expansion of the outer partial loops (as shown by the black arrows), takes place in both Al and Cu. The results for this last T_{33} case are also (at least academically) interesting in that they show how external loading can transform a perfect dislocation $\mathbf{AB}$ through the series of core reactions (6.13) and (6.27) into another perfect dislocation $\mathbf{CB}$, resulting in perfect slip. In contrast to dissociation into partials, such

"dissociation" (transformation) into perfect dislocations is energetically unfavourable unless the system is externally loaded *and no other more favorable mechanism is available*. In real systems, of course, such a more favorable mechanism generally exists.

6.6 Conclusion

In the current work, a dynamic phase field (PF) model for dislocation dissociation, stacking fault (SF) formation, slip and reactions in fcc single crystals has been developed and identified with the help of atomistic methods. To this end, periodic microelasticity (e.g., Khachaturyan 1983, Wang et al. 2001, Bulatov & Cai 2006, Chapter 11) has been combined with a PF-based model for residual strain resulting from dislocation lines (cores) and SFs. The energy model is formulated with the help of the interface energy approach of Cahn & Hilliard (1958), representing a type of local or generalized gradient approximation in the context of classical density functional theory (e.g., Evans 1979, Davis 1996). For the current dislocation case, the homogeneous part of this energy is related to homogeneous atomic displacement across the slip plane during dislocation slip and so to the (generalized) SFE (Vitek 1968); the "gradient" part is due to deviations from homogeneity such as occurs in the dislocation core (something also predicted by DFT-based core modeling: Iyer et al. 2015). As shown in this work, interface energy modeling facilitates global energy scaling, which in turn can be exploited to identify the PF model completely using atomistic data. In particular, the resulting gradient energy is material specific and related to the physical core. To demonstrate the application of the current approach, PF models were identified for fcc Al and Cu with the help of atomistic data and applied to the case of dynamic tensile loading of a dislocation loop in these materials. In the process, the thermodynamic PF picture in terms of energetic favorability and thermodynamic driving forces was compared to, and shown to be consistent with, the more standard mechanical picture in terms of the Peach-Köhler force. The example cases of Al and Cu demonstrate the ease of calculating atomistic input data for the current PF model and its predicative capability in the simulation of dislocation processes which are difficult to investigate via MD. The use of an atomic potential and MS in this work to determine this input data was for simplicity *only*; indeed, if available, more exact DFT-based input data can (and should) be used.

As shown in the current work, with the help of basic processes like dissociation, the interface energy model and scaling approach facilitate the atomistic determination of the (continuum) PF free energy as a mininum-difference approximation of the (discrete) atomic energy. Indeed, the PF free energy determined in this fashion represents an optimal continuum approximation of the exact atomistic (physical) energy. In this sense, the resulting atomistically determined PF model represents a type of model-order reduced approximation of more accurate atomistic modeling. As in other analogous cases, such reduction facilitates in particular the modeling of larger systems and longer timescales. Besides this, the pursuit of a PF approach as a continuum approximation or model reduction of more accurate atomistic modeling facilitates as well model generalization in the spirit of computation material design. As is well-known, in this framework, one can account for the effect of chemistry and temperature on the energy landscape, and so on dislocation and related deformation processes whose driving forces are determined by this landscape.

A number of further model developments are currently under investigation. One possibility in this regard is the application of the more general scaling method of Reina et al. (2014) in the current context. Rather than on thermodynamic equilibrium, their method is based on steady state, applies to both energetics and kinetics (i.e., mobility), and can be used to identify PF models using atomistic data from molecular dynamics (MD) simulations. As has been alluded to above, another further development involves the use

of *ab initio* DFT-based methods (e.g., Woodward et al. 2008), instead of an interatomic potential and MS or MD. Going even further, the generalization of such methods to larger systems with the help of coarse-graining methods (e.g., quasi-continuum: Iyer et al. 2015) may offer the possibility of true "concurrent" PF-DFT modeling of dislocation processes in the future.

Finally, it should be noted that the determination of the PF model in atomistic or *ab initio* fashion as developed in this work is almost certainly more subtle than the current treatment would imply. This is related for example to the fact that there exist qualitative differences between atomic modeling of dislocation processes and the current PF modeling. For example, atomic displacements modeled via DFT or an atomic potential and molecular statics are intrinsically non-linear, both geometrically and physically (especially in the core region). Another difference lies in the form of the respective energy models. Indeed, whereas in the atomistic or DFT case the energy is modeled via a single unified form (e.g., an atomic potential), in the PF model the energy is split into parts (i.e., elastic, SF contribution, etc.). That this may not in fact be necessary in a PF-based model is shown for example by the phase-field crystal approach (e.g., Wu et al. 2010). In any case, these and other issues represent work in progress to be reported on in the future.

APPENDIX

6.A Selected algorithmic & numerical details

Given the restriction to periodic fields and boundary conditions in this work, the algorithmic formulation and numerical solution of the corresponding coupled initial-boundary-value problem (IBVP) may be based on discrete Fourier, and more generally spectral, methods (e.g., Gottlieb & Orszag 1977, Canuto et al. 1988). These have a long tradition in periodic microelasticity (e.g., Khachaturyan 1983, Mura 1987, Khachaturyan et al. 1995, Wang et al. 2001, Li & Wang 2008) and geometrically linear solid mechanics (e.g., Moulinec & Suquet 1994, Suquet 1997, Nemat-Nasser & Hori 1999). More recently, they have been extended to the geometrically non-linear realm (e.g., Eisenlohr et al. 2013) as well. For completeness, a brief summary of the spectral algorithmic formulation of the current model is provided here. In a nutshell, this is based on fixed-point iteration (e.g., Suquet 1997, Dreyer & Müller 2000, Brown et al. 2002) for solution of (6.5) in Fourier space combined with semi-implicit time-integration of (6.6) as based on first-order Adams-Bashforth treatment of $\partial_{\phi_a}\psi$ (e.g., Chen & Shen 1998).

Consider first the algorithmic form of quasi-static momentum balance (6.5). The form of this applicable to strain-based fixed-point iteration is obtained from the convolution

$$\boldsymbol{G}_{\mathrm{H}} * \operatorname{div} \boldsymbol{T} = \boldsymbol{0} \tag{6.28}$$

of (6.5) with the Green function $\boldsymbol{G}_{\mathrm{H}}$ for a homogeneous reference medium with elastic stiffness C_{H}. Fourier transform of (6.28) yields $\hat{\boldsymbol{G}}_{\mathrm{H}}\hat{\boldsymbol{T}}\imath\boldsymbol{k} = \boldsymbol{0}$ for all non-zero wavenumbers $\boldsymbol{k} \neq \boldsymbol{0}$ with

$$\boldsymbol{a} \cdot \hat{\boldsymbol{G}}_{\mathrm{H}}^{-1}(\boldsymbol{k})\, \boldsymbol{b} := \boldsymbol{a} \otimes \boldsymbol{k} \cdot \mathsf{C}_{\mathrm{H}}[\boldsymbol{b} \otimes \boldsymbol{k}] \tag{6.29}$$

as usual for $\boldsymbol{k} \neq \boldsymbol{0}$ and all $\boldsymbol{a}, \boldsymbol{b}$. Then $\hat{\boldsymbol{G}}_{\mathrm{H}}\hat{\boldsymbol{T}}\imath\boldsymbol{k} \otimes \imath\boldsymbol{k} = -\hat{\boldsymbol{G}}_{\mathrm{H}}\hat{\boldsymbol{T}}\boldsymbol{k} \otimes \boldsymbol{k} = \boldsymbol{0}$ represents an implicit relation for $\boldsymbol{H} = \nabla\boldsymbol{u}$, and

$$-\hat{\boldsymbol{\Gamma}}_{\mathrm{H}}\hat{\boldsymbol{T}} := -\operatorname{sym}\hat{\boldsymbol{G}}_{\mathrm{H}}\hat{\boldsymbol{T}}\boldsymbol{k} \otimes \boldsymbol{k} = \boldsymbol{0} \tag{6.30}$$

one for $\boldsymbol{E} = \operatorname{sym}\nabla\boldsymbol{u}$, again for $\boldsymbol{k} \neq \boldsymbol{0}$. Here, $\boldsymbol{\Gamma}_{\mathrm{H}}$ is the Lippmann-Schwinger operator (e.g., Suquet 1997) induced by $\boldsymbol{G}_{\mathrm{H}}$. In the fixed-point context, then, $\hat{\boldsymbol{E}}^{(i+1)} = \hat{\boldsymbol{E}}^{(i)} - \hat{\boldsymbol{\Gamma}}_{\mathrm{H}}\hat{\boldsymbol{T}}^{(i)}$ follows from (6.30) for

the i^{th} iterative update step. Since C_{E} is homogeneous and constant in the current single crystal context, C_{H} can in fact be identified with C_{E} here, resulting in a further simplification of (6.30). Indeed, with $\hat{\boldsymbol{\Gamma}}_{\text{H}}\hat{\boldsymbol{T}} = \hat{\boldsymbol{\Gamma}}_{\text{E}}\mathsf{C}_{\text{E}}\hat{\boldsymbol{E}} - \hat{\boldsymbol{\Gamma}}_{\text{E}}\mathsf{C}_{\text{E}}\hat{\boldsymbol{E}}_{\text{R}}$ via the Fourier transform of (6.2), and $\mathsf{C}_{\text{E}}[\hat{\boldsymbol{u}} \otimes \imath\boldsymbol{k}]\boldsymbol{k} = \hat{\boldsymbol{G}}_{\text{E}}^{-1}\hat{\boldsymbol{u}}$ from (6.29), we have $\hat{\boldsymbol{\Gamma}}_{\text{E}}\mathsf{C}_{\text{E}}\hat{\boldsymbol{E}} = \operatorname{sym}\hat{\boldsymbol{G}}_{\text{E}}\mathsf{C}_{\text{E}}[\hat{\boldsymbol{u}} \otimes \imath\boldsymbol{k}]\boldsymbol{k} \otimes \boldsymbol{k} = \operatorname{sym}\hat{\boldsymbol{u}} \otimes \imath\boldsymbol{k} = \hat{\boldsymbol{E}}$. Consequently, (6.30) reduces to

$$\hat{\boldsymbol{E}}(\boldsymbol{k}) = \begin{cases} \hat{\boldsymbol{\Gamma}}_{\text{E}}(\boldsymbol{k})\mathsf{C}_{\text{E}}\hat{\boldsymbol{E}}_{\text{R}}(\boldsymbol{k}) & \boldsymbol{k} \neq \boldsymbol{0} \\ \bar{\boldsymbol{E}} & \boldsymbol{k} = \boldsymbol{0} \end{cases} \tag{6.31}$$

for the equilibrium strain field via (6.3) and (6.4), i.e., when C_{E} is constant. The corresponding stress field

$$\hat{\boldsymbol{T}}(\boldsymbol{k}) = \begin{cases} \mathsf{C}_{\text{E}}[\hat{\boldsymbol{E}}(\boldsymbol{k}) - \hat{\boldsymbol{E}}_{\text{R}}(\boldsymbol{k})] = (\mathsf{C}_{\text{E}}\hat{\boldsymbol{\Gamma}}_{\text{E}}(\boldsymbol{k})\mathsf{C}_{\text{E}} - \mathsf{C}_{\text{E}})\,\hat{\boldsymbol{E}}_{\text{R}}(\boldsymbol{k}) & \boldsymbol{k} \neq \boldsymbol{0} \\ \mathsf{C}_{\text{E}}[\bar{\boldsymbol{E}} - \hat{\boldsymbol{E}}_{\text{R}}(\boldsymbol{0})] & \boldsymbol{k} = \boldsymbol{0} \end{cases} \tag{6.32}$$

is equivalent to the relation obtained for example by Bulatov & Cai (2006, Equation (11.55)). Note that $\hat{\boldsymbol{E}}_{\text{R}}(\boldsymbol{0})$ is determined by $\bar{\boldsymbol{\phi}} = \hat{\boldsymbol{\phi}}(\boldsymbol{0})$ representing the volume average of this over the unit cell.

Consider next the algorithm for numerical solution of the Ginzburg-Landau relation (6.6). As mentioned above, this is based on semi-implicit time integration (e.g., Chen & Shen 1998). More specifically, first-order backward-difference approximation of $\dot{\phi}_a$, and first-order Adams-Bashforth approximation of $\partial_{\phi_a}\psi$, is employed. Let $I = \bigcup_{n=0}[t_n, t_{n+1}]$ represent the discretization of the time interval $I \subset \mathbb{R}$ of interest. For simplicity, assume that each subinterval $[t_n, t_{n+1}]$ of I is of the same duration $\Delta t = t_{n+1} - t_n$. Consider an arbitrary subinterval $[t_n, t_{n+1}]$. Assume as usual that $\boldsymbol{E}_n$, $\boldsymbol{\phi}_n$ ($\boldsymbol{\phi} := (\phi_1, \ldots)$), and so $(\partial_{\boldsymbol{\phi}}\psi)_n := (\partial_{\phi_1}\psi, \ldots)_n$, are known from the the solution obtained at the end of the previous time step. Fourier transformation of (6.6) and rearrangement then results in the linear system

$$\hat{\mathbf{M}}\,\hat{\boldsymbol{\phi}}_{n+1} = \hat{\boldsymbol{\phi}}_n - m_0\,\Delta t\,\widehat{(\partial_{\boldsymbol{\phi}}\psi)_n} \tag{6.33}$$

to solve for $\hat{\boldsymbol{\phi}}_{n+1}$ with $\hat{M}_{ab} := \delta_{ab} + m_0\,\Delta t\,\psi_{\text{G0}}\,\boldsymbol{k} \cdot \boldsymbol{N}_{ab}^g\boldsymbol{k}$ and $\boldsymbol{N}_{ab}^g$ given by (6.12). Note that (6.33) is a direct update; no iteration is required. In addition, note that $\hat{\mathbf{M}}$ depends only on (constant) material data and the chosen discretization in wavenumber space. For a given material and discretization, then, it need be calculated only once at the start as part of the initial data.

As discussed in the text, all material properties ψ_{H0}, ψ_{G0}, m_0, as well as $\boldsymbol{H}_a$ and $\boldsymbol{N}_{ab}^{\phi}$ for $a, b = 1, \ldots, p$, are known and constant. In addition, this holds for C_{E} and so for $\mathsf{C}_{\text{H}} = \mathsf{C}_{\text{E}}$ determining $\boldsymbol{G}_{\text{H}}$ and $\boldsymbol{\Gamma}_{\text{H}}$. All field relations are solved in dimensionless form. The effective shear modulus μ_{fcc} is used as the basic energy density scaling. Together with the (constant isothermal) mobility m_0 from (6.6), this determines the time scaling $1/(\mu_{\text{fcc}}\,m_0)$. Length scaling is based on d_{111}, which also represents the grid point spacing in the numerical simulations. In particular, in this case, the dislocation core is resolved over multiple grid points in the slip plane (see for example Figure 6.4 in the text).

6.B Thermodynamic driving & Peach-Köhler forces

The purpose of this appendix is the relation of the evolution of the dislocation thermodynamic state and the related driving force inherent in the Ginzburg-Landau relation (6.6) to the Peach-Köhler force (PKF) and the results in Figure 6.6. To this end, consider a plane S in the single crystal across which the crystal lattice has been slipped by dislocations. Let S_- represent the unslipped side, and S_+ the slipped side, of S. Assume that the unit normal $\boldsymbol{n}_S$ to S points from S_- to S_+. Let $[\![f]\!]_S := f_+ - f_-$ represent the jump in the limits $f_\pm$ of any field f on $S_\pm$ across S. In particular, for Volterra dislocations (e.g., Landau

& Lifshitz 1970, Hirth & Lothe 1982, Teodosiu 1982, Mura 1987, Li & Wang 2008, Balluffi 2012), we have $[\![\boldsymbol{x}]\!]_S = \boldsymbol{0}$ and $[\![\boldsymbol{u}]\!]_S \neq \boldsymbol{0}$. In addition,

$$[\![\nabla \boldsymbol{u}]\!]_S = \frac{[\![\boldsymbol{u}]\!]_S}{d_S} \otimes \boldsymbol{n}_S \tag{6.34}$$

then holds for the distortion field across S via the Hadamard lemma (e.g., Šilhavý 1997, Proposition 2.1.6), d_S being the "width" or "thickness" of S. Consider next the relation between $[\![\boldsymbol{u}]\!]_S$ and the closure failure around a Burgers circuit. To this end, let D represent a "right-handed" dislocation loop on S as shown in Figure 6.B.1. "Right-handed" here means that, when the unit tangent $\boldsymbol{t}_D$ to D is oriented in the

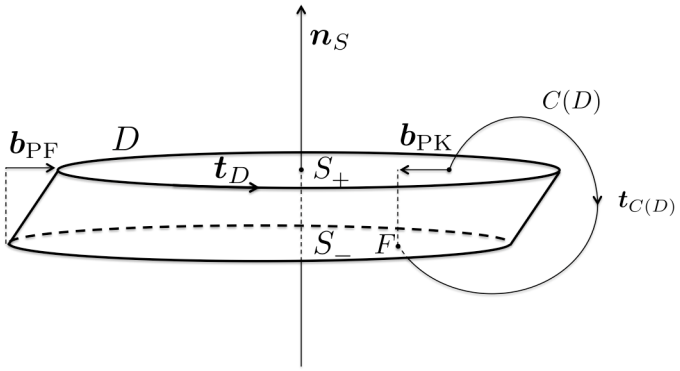


Figure 6.B.1: Relation between the Burgers vector convention $\boldsymbol{b}_{\mathrm{PF}} \equiv [\![\boldsymbol{u}]\!]_S$ inherent in the residual distortion model (6.3)-(6.4) and that $\boldsymbol{b}_{\mathrm{PK}} \equiv -[\![\boldsymbol{u}]\!]_S$ (SF/RH convention) in the definition of Peach-Köhler force. See text for details.

direction of the (fingers of the) right hand, the right-hand thumb is parallel to $\boldsymbol{n}_S$, and $\boldsymbol{t}_D \cdot \boldsymbol{n}_S = 0$. Let $C(D)$ represent a Burgers circuit around D with unit tangent $\boldsymbol{t}_{C(D)}$ (Figure 6.B.1) enclosing a surface $S(C)$ with unit normal $\boldsymbol{n}_{S(C)}$ in a right-handed fashion. In this case, at the point where D intersects $S(C)$, $\boldsymbol{t}_D$ is parallel to $\boldsymbol{n}_{S(C)}$. In this case, $C(D)$ starts on the slipped side $\boldsymbol{x}_+ \in S_+$ of S and ends on the unslipped side $\boldsymbol{x}_- \in S_-$ of S, and

$$\oint_{C(D)} \nabla_{\boldsymbol{t}_{C(D)}} \boldsymbol{u} \, dl = \boldsymbol{u}_- - \boldsymbol{u}_+ = -[\![\boldsymbol{u}]\!]_S \tag{6.35}$$

follows. This corresponds to the concept of "local" Burgers vector and the so-called SF/RH convention ("start-finish / right-hand"; e.g., Hirth & Lothe 1982, Balluffi 2012, Chapter 12). In particular, as shown in Figure 6.B.1, $C(D)$ starts on S_+ ("start" in "SF") and ends on S_- at F ("finish" in "SF").

Next, let $S = S_a$ represent any $\{111\}$ slip plane in the single crystal. Let $\boldsymbol{t}_{Da}$ be the unit tangent field of a (curved) dislocation line on S_a, and $\boldsymbol{m}_{Da} := \boldsymbol{t}_{Da} \times \boldsymbol{n}_a$ the unit normal to D tangent to S_a in the direction of line bow-out (note $\boldsymbol{t}_{Da} \cdot \boldsymbol{n}_a = 0$). Mechanical equilibrium $[\![\boldsymbol{T}]\!]_a \boldsymbol{n}_a = \boldsymbol{0}$ on S_a then results in the form

$$[\![\boldsymbol{T}\boldsymbol{n}_a \cdot \boldsymbol{u}]\!]_a = \boldsymbol{T}^{\mathrm{T}} [\![\boldsymbol{u}]\!]_a \cdot \boldsymbol{n}_a = \boldsymbol{T}^{\mathrm{T}} \boldsymbol{b}_{\mathrm{PK}a} \times \boldsymbol{t}_{Da} \cdot \boldsymbol{m}_{Da} \tag{6.36}$$

for the component of the mechanical force $\boldsymbol{T}^{\mathrm{T}} \boldsymbol{b}_{\mathrm{PK}a} \times \boldsymbol{t}_{Da}$ per unit length in the direction $\boldsymbol{m}_{Da}$ on the dislocation with Burgers vector $\boldsymbol{b}_{\mathrm{PK}a} := -[\![\boldsymbol{u}]\!]_a$ (see Figure 6.B.1), i.e., of the PKF (e.g., Hirth & Lothe 1982, Equation (4-43)). As usual, the PKF splits

$$\boldsymbol{T}^{\mathrm{T}} \boldsymbol{b}_{\mathrm{PK}a} \times \boldsymbol{t}_{Da} = (\boldsymbol{b}_{\mathrm{PK}a} \cdot \boldsymbol{T}\boldsymbol{m}_{Da}) \, \boldsymbol{n}_a - (\boldsymbol{b}_{\mathrm{PK}a} \cdot \boldsymbol{T}\boldsymbol{n}_a) \, \boldsymbol{m}_{Da} \tag{6.37}$$

into glide $-\boldsymbol{b}_{\mathrm{PK}a} \cdot \boldsymbol{T}\boldsymbol{n}_a$ and climb $\boldsymbol{b}_{\mathrm{PK}a} \cdot \boldsymbol{T}\boldsymbol{m}_{Da}$ components. Related to the former is the expression

$$\boldsymbol{T}\boldsymbol{n}_a \cdot [\![\nabla \boldsymbol{u}]\!]_a \boldsymbol{n}_a = ([\![\boldsymbol{u}]\!]_a \cdot \boldsymbol{T}\boldsymbol{n}_a)/d_a = (\boldsymbol{b}_{\mathrm{PF}a} \cdot \boldsymbol{T}\boldsymbol{n}_a)/d_a \tag{6.38}$$

obtained from (6.34) and mechanical equilibrium on S_a for the mechanical work per unit volume performed by $\boldsymbol{T}$ in slipping S_a, with $\boldsymbol{b}_{\mathrm{PF}a} := [\![\boldsymbol{u}]\!]_a$ (see Figure 6.B.1). In turn, (6.38) is comparable to the elastic part

$$-\partial_{\phi_a} \psi_{\mathrm{E}} = \boldsymbol{T} \cdot \boldsymbol{H}_a = (\boldsymbol{b}_a \cdot \boldsymbol{T}\boldsymbol{n}_a)/d_a = (\boldsymbol{b}_{\mathrm{PF}a} \cdot \boldsymbol{T}\boldsymbol{n}_a)/d_a \tag{6.39}$$

via (6.1)-(6.4) of the "local" part $-\partial_{\phi_a} \psi$ of the non-local thermodynamic driving force $-\delta_{\phi_a} \psi$ determining the evolution of $\phi_r a$ in (6.6). Consequently, the thermodynamic driving force $-\partial_{\phi_a} \psi_{\mathrm{E}}$ is comparable to the glide component $-\boldsymbol{b}_{\mathrm{PK}a} \cdot \boldsymbol{T}\boldsymbol{n}_a$ of the mechanical PKF. These are used to obtain the results for the PKF in Figure 6.6 in the text.

CHAPTER 7

TRANSPORT BASED DISLOCATION MODELING*

"Computers in the future may weigh no more than 1.5 tons."
-Popular Mechanics, 1949

7.1 Introduction

The classic Hall-Petch relation between yield stress and grain size has often been attributed in the literature (e.g., Hirth & Lothe 1982) to dislocation pile-up at grain boundaries resulting from dislocation creation and transport under loading. A number of corresponding transport models have been formulated based on dislocation (line) density (and line curvature) (e.g., Groma et al. 2003, Sedláček et al. 2003, Hochrainer et al. 2007). For the most realistic 3D case, such models are extremely complex and sophisticated in nature. In order to gain insight into the basic physics involved, a number of simplified models and cases have been investigated in the literature. Such simplifications include for example restriction to straight edge and screw distributions (e.g., Walgraef & Aifantis 1985, Arsenlis & Parks 2002), or excess edge and screw distributions together with their mean curvature and the total dislocation content (e.g., Sandfeld et al. 2011). In the non-transport context, non-local-, Volterra-based modeling of dislocation interaction and pile-up has been considered more recently by Baskaran et al. (2010), Aghababaei et al. (2011), Schulz et al. (2014). Dogge (Dogge 2014, Chapter 2) considered the transport and pile-up behavior of single- and two-sign continuous distributions of Volterra-based infinite discrete dislocation walls in one dimension based on weakly non-local (WNL) wall interaction modeling. Comparison with discrete Volterra-based modeling of wall pile-up (e.g., Roy et al. 2008, de Geus et al. 2013) showed a strong discrepancy between discrete and WNL-based continuum wall pile-up behavior near the boundary. To investigate the possibility that this discrepancy is due to the assumption of weak non-locality

*This chapter is based on the work in Mianroodi, Peerlings & Svendsen (2016)

in the continuum modeling, a continuum model for transport is developed in the current work in which wall interaction is SNL. As is known from more general considerations (e.g., Mesarovic 2005, Mesarovic et al. 2010, Kooiman et al. 2015), dislocation interaction is intrinsically SNL. In order to work with a non-singular model for SNL dislocation interaction in a continuum setting, the Peierls-Nabarro (PN) model (e.g., Hirth & Lothe 1982, Chapter 8) for the dislocation stress field is employed. Other approaches to the modeling of non-singular stress in the continuum context include numerical regularization (e.g., Cai et al. 2006) or gradient-based elasticity (e.g., Groma et al. 2010, Lazar 2013).

The chapter begins with a brief summary of the basic relations for the transport model in Section 7.2. For simplicity, the focus here is on transport alone; all sources are neglected. As well, a uniform external stress field is assumed. Except for the dislocation mobility, all material properties are also treated as uniform. In this case, the principal spatial inhomogeneity in the force driving dislocation flux and transport in the model is due to the dislocation (wall) interaction stress field. An SNL model for this as based on the stress field of an infinite discrete dislocation wall is formulated with the help of the PN model in Section 7.3. Although not valid in the current case of single-sign dislocation distributions, for completeness and comparison, the WNL approximation of this SNL-based interaction stress model is also considered in Section 7.4. After discussing the algorithmic formulation of the current PN-SNL-based transport model in Section 7.5, the model is then applied to the case of transport and pile-up in Section 7.6. In particular, dependence on the spatial variation of mobility in the pile-up boundary, as well as external loading, are investigated. In addition, the breakdown of the WNL approximation to the SNL wall stress model near the boundary is documented. The chapter ends with a summary and discussion in Section 7.7. For completeness, the connection between selected PN-based model relations and their more familiar Volterra-based counterparts are documented in Appendix 7.A.

7.2 Basic relations

Consider a family of infinite, straight edge dislocation lines in an isotropic linear elastic medium with constant shear modulus G and Poisson's ratio ν. Let the lines be oriented parallel to z with Burgers vector of length b in the x direction. Assume the lines glide only and remain in their glide planes. The glide plane of each line is then parallel to the (x, z) plane, and the glide plane normal is parallel to y. Assume that the dislocations arrangement in the y direction perpendicular to the glide planes takes the form of (straight or tilt) walls with uniform spacing h between adjacent dislocations in each wall. Consequently, each wall itself represents an h-periodic discrete distribution of lines. Given no climb, each such wall is maintained at all times. Since the distribution is then h-periodic in y, we can (without loss of generality) focus attention on a single glide plane, for example at $y = 0$, and the only remaining spatial dependence is in x.

Let $\rho(x, t)$ represent the number* of mobile walls per unit length at (x, t). Then $1/\rho$ represents the wall spacing in x direction. The initial value $\rho(x, 0) = \rho_0(x)$ is assumed to be known and the total number of dislocations, i.e. the integral of ρ over the one-dimensional region under consideration, is constant. Under the influence of external loading and interaction, the walls flow (glide) in x direction, resulting in a change in their number per unit length along x. The corresponding transport relation takes the form

$$\frac{\partial \rho}{\partial t} + \frac{\partial \Phi}{\partial x} = 0 \tag{7.1}$$

* ρ in the current work corresponds to $h\rho^+$ in the work of (Dogge 2014, Chapter 2).

in terms of the dislocation flux (number per unit time)

$$\Phi(x,t) = \rho(x,t)\, v(x,t) \tag{7.2}$$

depending on the wall (line) velocity $v(x,t)$. A positive flux implies that the (positive) walls flow in the $+x$ direction. Restricting attention to quasi-static conditions and overdamped motion,

$$v(x,t) = m(x)\, b\, \{\tau + \sigma(x,t)\} \tag{7.3}$$

holds via Peach-Koehler in terms of the wall (line) mobility $m(x)$, Burgers vector magnitude b, and the shear stress field $\tau + \sigma(x,t)$ on the glide plane $y = 0$. In the current work, this depends on the constant applied external shear stress τ and the contribution $\sigma(x,t)$ resulting from wall interaction in the glide plane. In view of the inherently long-range character of dislocation interaction, the basic model relations are completed by the strongly non-local (SNL) form*

$$\sigma(x,t) = \varsigma * \rho\,(x,t) = \int_{-\infty}^{+\infty} \varsigma(x-\xi)\, \rho(\xi,t)\, d\xi = \int_{-\infty}^{+\infty} \varsigma(\xi)\, \rho(x-\xi,t)\, d\xi \tag{7.4}$$

for $\sigma(x,t)$ as the convolution of the stress field $\varsigma(x)$ of a single dislocation wall with the corresponding distribution $\rho(x,t)$ in the glide plane. Combination of (7.4) with (7.1)-(7.3) results in a partial integro-differential transport relation for ρ. Since τ is assumed constant, it satisfies mechanical equilibrium identically. Then $\gamma = \gamma_{\rm P} + \tau/G$ holds for the shear strain field, with the Orowan relation $\dot\gamma_{\rm P} = b\,\rho\, v$ determining $\gamma_{\rm P}$ as usual.

For notational simplicity, in the rest of this work, all stresses are non-dimensionalized by $G/(1-\nu)$, and all lengths by b. As well, the t-dependence of fields will be suppressed in the notation.

7.3 PN-based model for ς and σ

As discussed in the introduction, the current work is based on Peierls dislocations and the PN model (e.g., Hirth & Lothe 1982, Chapter 8) which accounts for lattice resistance to dislocation-based distortion. In the simplest† case,

$$\sigma_0^{\rm PN}(x,y) = \frac{1}{2\pi}\, \frac{x(c^2 + x^2 - y^2)}{(x^2 + (|y| + c)^2)^2} \tag{7.5}$$

(Hirth & Lothe 1982, Equation (8-13) and footnote, Page 223) holds for the (equilibrium) PN-based xy shear component of the stress field of a single Peierls (edge) dislocation located at $(x,y) = (0,0)$, with $c := d/2(1-\nu)$ in terms of the glide-plane spacing d. For example, in the case of (fcc) aluminum, $d = \sqrt{2/3}$, $\nu = 0.35$ and $c \approx 0.63$. Recall that x and y, as well as all other lengths, are scaled here and in what follows by b. As discussed above, the current work focuses on transport of infinite discrete dislocation walls with respect to a single glide plane at $y = 0$. Figure 7.1 displays $\sigma_0^{\rm PN}(x, y=0)$ for selected values of d.

Given the assumption of uniform spacing h of wall dislocations,

$$\sigma_{\rm w}^{\rm PN}(x) := \sum_{n=-\infty}^{\infty} \sigma_0^{\rm PN}(x, -nh) = \frac{1}{2\pi}\, \frac{x}{x^2 + c^2} + \frac{x}{h^2} \sum_{n=1}^{\infty} \frac{1}{\pi}\, \frac{(c^2/h^2 - n^2 + x^2/h^2)}{((c/h + n)^2 + x^2/h^2)^2} \tag{7.6}$$

* Limits in (7.4) are assumed infinite because the model (7.7) for $\varsigma(\xi)$ has bounded support (see Figure 7.2).

† Assuming an infinite isotropic linear elastic medium and the Frenkel model for lattice resistance.

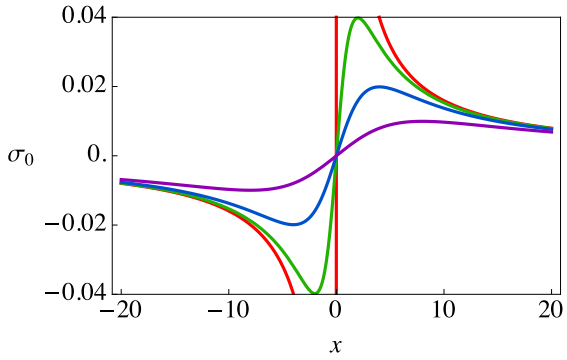


Figure 7.1: $\sigma_0^{\mathrm{PN}}(x, y = 0)$ from (7.5) for $d = 0$ (red; Volterra), $d = 1/2$ (green), $d = \sqrt{2/3}$ (blue), $d = 1$ (violet). Again, x and d are scaled by b.

follows from (7.5) for the wall stress field at $y = 0$. In the current PN context, a lower bound to h is the glide-plane spacing d (e.g., $d = \sqrt{2/3}$ in the fcc case). The second form in (7.6) is based on the fact that $\sigma_0^{\mathrm{PN}}(x, y)$ is even in y. With the help of analytical results on the series representation of the polygamma function (Gradshteyn & Ryzhik 1980, §8.362), (7.6) takes the form

$$\sigma_{\mathrm{w}}^{\mathrm{PN}}(x) = \frac{1}{2\pi}\,\frac{x}{x^2 + c^2} - \frac{x}{\pi h^2}\,\Re\,\psi^{(1)}(\zeta_{h,c}(x)) - \frac{c}{\pi h^2}\,\Im\,\psi^{(1)}(\zeta_{h,c}(x))\,, \tag{7.7}$$

in terms of the real $\Re\,\psi^{(1)}$ and imaginary $\Im\,\psi^{(1)}$ parts of the first-order polygamma function $\psi^{(1)}(z)$, with $\zeta_{h,c}(x) := 1 + c/h + \imath x/h$ and $\imath = \sqrt{-1}$. $\sigma_{\mathrm{w}}^{\mathrm{PN}}(x)$ is depicted in Figure 7.2 for different values of h. As shown, an increase in h results in an increase of $\sigma_{\mathrm{w}}^{\mathrm{PN}}$. In particular, note that $\sigma_0^{\mathrm{PN}}(x, y = 0) =$

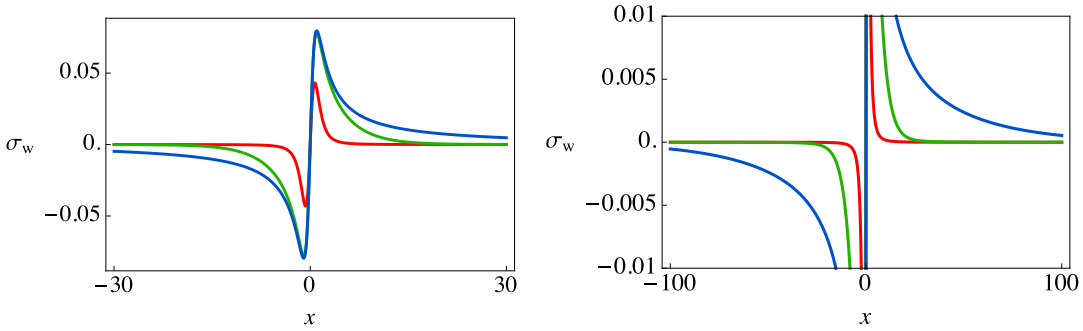


Figure 7.2: $\sigma_{\mathrm{w}}^{\mathrm{PN}}(x)$ showing maxima (left) and decay behavior (right) for $h = 2\,d$ (red), $h = 20\,d$ (green), $h = 200\,d$ (blue), and $d = \sqrt{2/3}$.

$\lim_{h\to\infty} \sigma_{\mathrm{w}}^{\mathrm{PN}}(x)$ from (7.7) corresponds to the stress field of a single PN dislocation at $(x = 0, y = 0)$ on the glide plane $(x, y = 0)$ via (7.5). Given then $\sigma_{\mathrm{w}}^{\mathrm{PN}}$ from (7.7), the choice $\varsigma = \sigma_{\mathrm{w}}^{\mathrm{PN}}$ in (7.4) results in the PN-based model

$$\sigma_{\mathrm{SNL}}^{\mathrm{PN}}(x) := \sigma_{\mathrm{w}}^{\mathrm{PN}} * \rho\,(x) \tag{7.8}$$

for the interaction contribution σ to the stress field driving dislocation flow in the transport model.

7.4 Weakly non-local approximation

The weakly non-local (WNL) approximation to (7.4) is based as usual on the Taylor series expansion

$$\rho(x-\xi) \approx \rho(x) - \frac{\partial\rho}{\partial x}(x)\,\xi + \frac{1}{2}\,\frac{\partial^2\rho}{\partial x^2}(x)\,\xi^2 + \cdots \tag{7.9}$$

of $\rho(x-\xi)$ about $\rho(x)$ assuming $|\xi| \ll 1$, such that

$$\sigma(x) \approx c_0\,\rho(x) + c_1\,\frac{\partial\rho}{\partial x}(x) + c_2\,\frac{\partial^2\rho}{\partial x^2}(x) + \cdots\,, \quad c_k := \frac{(-1)^k}{k!}\int_{-\infty}^{+\infty}\xi^k\varsigma(\xi)\,d\xi\,. \tag{7.10}$$

In particular, if $\varsigma(\xi)$ is odd, c_k with $k = 0$ or k even vanish, and (7.10) contains only odd terms. Note that $\sigma_{\mathrm{w}}^{\mathrm{PN}}(x)$ in (7.7) is odd, as can also be seen from Figure 7.2. In general, (7.9) may diverge, in which case (7.10) does not approximate (7.4). In other contexts than the current one, e.g., interaction of $+$ and $-$ dislocation ensembles where screening plays a role, or (short-range) interaction with obstacles or boundaries, however, (7.10) is relevant. In this context,

$$\sigma_{\mathrm{WNL}}^{\mathrm{PN}}(x) := c_1^{\mathrm{PN}}\,\frac{\partial\rho}{\partial x}(x) = -\tfrac{1}{2}\,(c + \tfrac{1}{3}\,h)\,\frac{\partial\rho}{\partial x}(x) \tag{7.11}$$

represents the lowest-order WNL approximation to $\sigma_{\mathrm{SNL}}^{\mathrm{PN}}(x)$ from (7.8) via (7.10). For completeness, (7.8) and (7.11) are compared with each other and with the Volterra-based WNL interaction stress model*

$$\sigma_{\mathrm{WNL}}^{\mathrm{V}}(x) = \lim_{d\to 0}\sigma_{\mathrm{WNL}}^{\mathrm{PN}}(x) = -\tfrac{1}{6}\,h\,\frac{\partial\rho}{\partial x}(x) \tag{7.12}$$

from (Dogge 2014, Chapter 2) in the next section for different given density distributions. Since $c = d/2(1-\nu)$ and $h \geqslant d$, note that $c \leqslant h$ in general; for larger h, then, c_1^{PN} is dominated by h. Again, although (7.11) is not valid in the current context, for interest's sake, it will be compared with the SNL model (7.8) in what follows.

7.5 Algorithmic formulation

7.5.1 Convolution integral

To evaluate the convolution integral (7.4), a number of possibilities exist. Of these, the simplest of course is direct numerical discretization. To this end, let

$$x_0 = -L,\, x_1 = \Delta x - L,\, \ldots,\, x_{N-1} = (N-1)\Delta x - L,\, x_N = N\Delta x - L, \tag{7.13}$$

represent a regular discretization of the real interval $[-L, L]$ of length $2L$ based on $N+1$ nodes (N even) with separation Δx such that $2L = N\Delta x$. Then

$$\sigma_i = \Delta x\sum_{j=0}^{N}\varsigma_{ij}\,\rho_j =: \Delta x\,\varsigma_{ij}\,\rho_j\,, \quad i = 0, \ldots, N\,, \tag{7.14}$$

*The coefficient in Equation (12) of (Dogge 2014, Chapter 2) differs by a factor of two from that in (7.12) due to different stress scaling.

approximates (7.4) in array-matrix form, with

$$f_i \approx f(x_i) = f(i\Delta x - N\Delta x/2)\,, \quad \varsigma_{ij} \approx \varsigma(x_i - x_j) = \varsigma(i\Delta x - j\Delta x)\,, \tag{7.15}$$

($x_i = (i - N/2)\Delta x$ from (7.13)). As can be seen from Figure 7.2, note that $\varsigma(x) \equiv \sigma_{\rm w}^{\rm PN}(x)$ is odd, and $\varsigma_{ji} = -\varsigma_{ij}$. As shown in Figure 7.2, $\sigma_{\rm w}^{\rm PN}(x)$ decays "quickly" to zero as $x \to \pm\infty$; consequently, for sufficiently large N, (7.14) is a reasonable approximation of (7.4). In particular, the stress peak is well-resolved for $\Delta x \leqslant b$. Issues related to grid size N, numerical resolution, and solution convergence will be investigated and addressed as they arise in what follows.

Calculating the sums explicitly in (7.14) is not very efficient ($O(N^2)$). As is well-known, much more efficient ($O(N \ln N)$) in this regard is convolution via fast Fourier transform (FFT: e.g., Press et al. 2007, Chapter 13). This is based in particular on the result

$$\sigma(x) = \varsigma * \rho(x) = \mathcal{F}^{-1}\{\hat{\varsigma}(k)\,\hat{\rho}(k)\} = \mathcal{F}^{-1}\{\hat{\varsigma}(k)\,\mathcal{F}\{\rho(x)\}\} \tag{7.16}$$

from (7.4) with

$$\hat{\varsigma}(k) \equiv \hat{\sigma}_{\rm w}^{\rm PN}(k) = \imath\,\frac{k}{|k|}\,\frac{e^{h|k|}\,(h|k| - \sinh h|k|)\,(\cosh c|k| - \sinh c|k|)}{(\cosh h|k| + \sinh h|k| - 1)^2} \tag{7.17}$$

from (7.7). Note that $\lim_{k\to 0}\hat{\sigma}_{\rm w}^{\rm PN}(k) = 0$ and $\lim_{k\to\pm\infty}\hat{\sigma}_{\rm w}^{\rm PN}(k) = 0$ ($c > 0, h > 0$). As discussed above, since $\sigma_{\rm w}^{\rm PN}(x)$ is odd, $\hat{\varsigma}(k)$ is purely imaginary. Then $\Re\hat{\varsigma} = 0$ and $\hat{\varsigma}\,\hat{\rho} = \imath\,\Im\hat{\varsigma}\,\Re\hat{\rho} - \Im\hat{\varsigma}\,\Im\hat{\rho}$. In the SNL context, $\sigma = \sigma_{\rm SNL}^{\rm PN}$ based on (7.8) is updated via discrete convolution and FFT based on (7.16) and (7.17) as discussed above. This will be compared with the WNL approximation $\sigma = \sigma_{\rm WNL}^{\rm PN}$ from (7.11) in what follows.

For evenly spaced "data" with spacing Δx, $k_{\rm c} = 1/2\Delta x$ represents the Nyquist critical wavenumber. As is well-known, any wavenumber component outside the range $(-k_{\rm c}, k_{\rm c})$ is aliased into this range by numerical approximation. Trapezoidal approximation of (continuous) Fourier transformation in one dimension and truncation yields as usual the corresponding discrete Fourier transform (DFT) pair

$$\tilde{f}_q = \sum_{p=0}^{N-1} e^{-2\pi\imath pq/N} f_p\,, \quad f_p = \frac{1}{N}\sum_{q=-N/2}^{N/2-1} e^{+2\pi\imath pq/N}\tilde{f}_q\,, \tag{7.18}$$

(e.g., Press et al. 2007, §12.1.2) with $f(x_p) \approx f_p$ and $\hat{f}(k_q) \approx \Delta x\tilde{f}_q$ as usual. Since $\tilde{f}_{-q} = \tilde{f}_{N-q}$ for $q = 0, \ldots, N$ via periodicity, q could also vary from 0 to $N - 1$ in (7.18). This is referred to as "wrap-around" order (e.g., Press et al. 2007, §12.2). In this case, the zero wavenumber is at $q = 0$, $0 < k < k_{\rm c}$ correspond to $0 \leqslant q \leqslant N/2 - 1$, and $-k_{\rm c} < k < 0$ to $N/2 + 1 \leqslant q \leqslant N - 1$. The value at $q = N/2$ corresponds to both $k = \pm k_{\rm c}$.

For computational purposes, the DFT in (7.18) is rearranged as usual into fast Fourier transform (FFT) form (e.g., Press et al. 2007, §12.3). Numerical evaluation of (7.16) via (7.17) is based on the discrete convolution theorem (e.g., Press et al. 2007, §13.1). In this context, $\rho(x)$ represents the "data", and $\varsigma(x)$ the "response", function.

7.5.2 Time discretization

The numerical solution of the basic transport relation (7.1) with (7.3) is based here on simple first-order forward finite difference (FD) approximation in time together with first-order upwind FD approximation

in space, i.e.,

$$\rho_j^{n+1} = \rho_j^n - \frac{\Delta t}{\Delta x} \begin{cases} \rho_{j+1}^n v_{j+1}^n - \rho_j^n v_j^n & \text{if } v_j^n \leqslant 0 \\ \rho_j^n v_j^n - \rho_{j-1}^n v_{j-1}^n & \text{if } v_j^n > 0 \end{cases} . \tag{7.19}$$

As usual, for $v_j^n > 0$, the Courant-Friedrichs-Lewy (CFL) condition $\Delta t \leqslant \Delta x / v_j^n$ is necessary but not sufficient for stability. Central differencing is used to discretize $\partial\rho/\partial x$ in (7.11).

7.6 Results

As already mentioned above, unless otherwise stated, all results to follow are dimensionless. In particular, all lengths are scaled by b, and all stresses by $G/(1-\nu)$. Unless otherwise stated, $d = \sqrt{2/3}$. As well, to be compatible with (Dogge 2014, Chapter 2), $h = 200 = 10\sqrt{6}\, d$ is assumed in all cases.

7.6.1 Mobility and boundary modeling

The effect of a boundary as an obstacle to wall transport is modeled here via a spatially heterogeneous mobility $m(x)$ in (7.3). For simplicity, $m(x)$ is modeled to this end on the regularized unit rectangle or "box-car" function (e.g., Bracewell 2000, Chapter 4), i.e.,

$$f(x; a, p) := \frac{\sinh(2ap)}{\cosh(2ax) + \cosh(2ap)} . \tag{7.20}$$

Here, p the position of the center of the boundary region, and $1/a$ its effective width. Like x, $1/a$ and p are in general scaled by b. In terms of f, the boundary region is then defined by values of x for which $0 \leqslant f(x; a, p) \lessapprox 1$ holds. This is shown in Figure 7.1. In particular, the impenetrable case ($ah = \infty$)

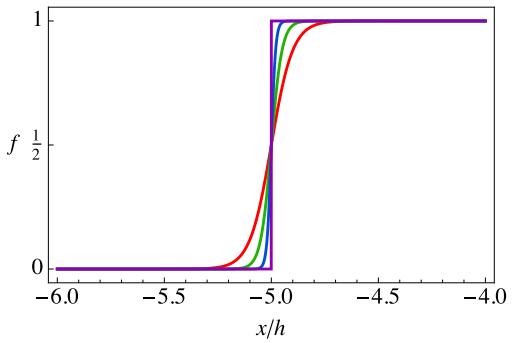


Figure 7.1: Left-half of regularized box-car function $f(x; a, p)$ from (7.20) for $p/h = 5$ and $ah = 10$ (red), $ah = 20$ (green), $ah = 50$ (blue), $ah = \infty$ (violet).

was investigated by (Dogge 2014, Chapter 2). As evident, the effective boundary width and length over which $f(x; a, p)$ reduces to zero is basically controlled by a. The effect of varying boundary width in this sense on pile-up behavior will be investigated in what follows.

7.6.2 Interaction stress for a fixed distribution

To begin, consider the interaction stress resulting from a fixed wall distribution. In particular, using $f(x;a,h)$ from (7.20), "sharp" $\rho(x) = f(x; ah = 4 \times 10^4, p/h = 2.5)$ and "diffuse" $\rho(x) = f(x; ah = 5, p/h = 2.5)$ distributions are compared. The resulting SNL and WNL interaction stress fields in the region $[-L, L]$ with $L = 5h$ are shown in Figure 7.2. Note that $\sigma^{\mathrm{PN}}_{\mathrm{SNL}}$ and $\sigma^{\mathrm{PN}}_{\mathrm{WNL}}$ are in much better

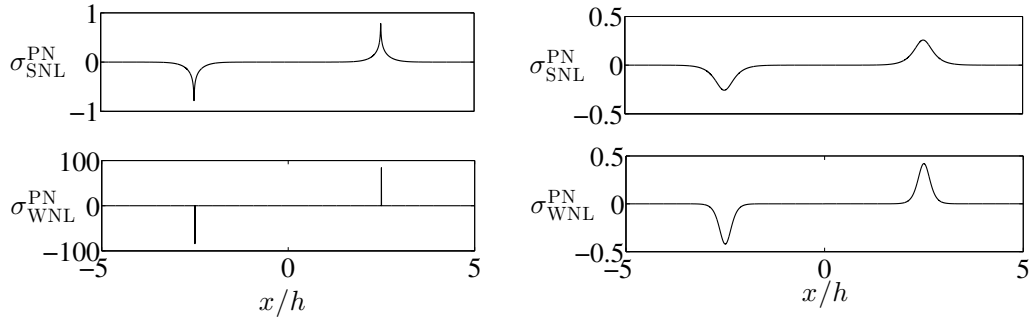


Figure 7.2: Comparison of interaction stress profiles based on $\sigma^{\mathrm{PN}}_{\mathrm{SNL}}$ (top) from (7.8) and $\sigma^{\mathrm{PN}}_{\mathrm{WNL}}$ (bottom) from (7.11) due to "sharp" $\rho(x) = f(x; ah = 4 \times 10^4, p/h = 2.5)$ (left) and "diffuse" $\rho(x) = f(x; ah = 5, p/h = 2.5)$ (right) distributions. For this calculation, $N = 10000$ was assumed.

agreement in the diffuse case (Figure 7.2, right) because the Talyor series approximation (7.9) of $\rho(x)$ in the diffuse case is of course much better. Since the pile-up distribution at an impenetrable boundary (as assumed in basically all pile-up simulations: e.g., Dogge 2014) is in this sense more "sharp" than "diffuse", these results imply that any WNL-based approximation of inherently SNL dislocation interaction at such a boundary will breakdown. Exactly this has basically already been observed in the context of the comparison of Volterra-based discrete SNL and continuous WNL modeling (e.g., Roy et al. 2008, de Geus et al. 2013).

For the numerical simulation of transport and pile-up behavior to follow, the dependence of numerical convolution via (7.16) and (7.18) on grid size N is an issue. This is investigated in Figure 7.3. This

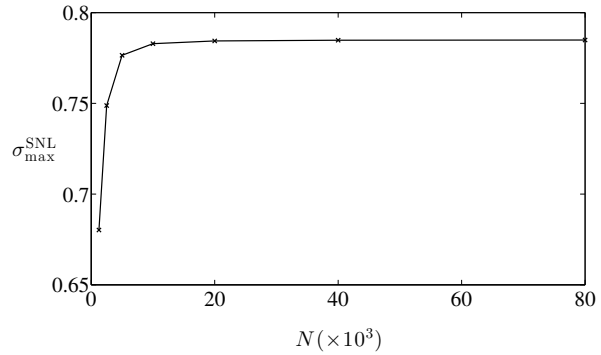


Figure 7.3: Maximum interaction stress $\sigma^{\mathrm{SNL}}_{\mathrm{max}}$ calculated via (7.16) and (7.18) as a function of N for a fixed dislocation density distribution $\rho(x) = f(x; ah = 4 \times 10^4, p/h = 2.5)$.

is based on $\sigma^{\mathrm{PN}}_{\mathrm{SNL}}$ from (7.8) and calculated for the same setup as in Figure 7.2 (top left). Clearly, the

numerical convolution converges; in particular, note that the relative difference between $\sigma_{\max}^{\mathrm{SNL}}(N = 80000)$ and $\sigma_{\max}^{\mathrm{SNL}}(N = 5000)$ is about 1%.

7.6.3 Effect of boundary conditions

All transport simulations to follow are carried out on the interval $[-L, L]$ with $L = 6h$ and $h = 200$ (Dogge 2014, Chapter 2 also assumed $h = 200$). In this case, $\Delta x = 2L/N = 12h/N = 2400b/N$. In comparison to Dogge (2014), the current computational domain $[-L, L]$ is $1h$ wider on either side in order to investigate the effect of different boundary mobility profiles on the pile-up behavior. Following (Dogge 2014, Chapter 2), an initially uniform density $\rho(t = 0, x) = \rho_0$ of $\rho_0 = 0.0635$ is assumed, corresponding to an initial wall spacing of $s_0 = 1/\rho_0 = 15.748$ in the glide plane. Note that s_0 is an order of magnitude smaller than the dislocation spacing $h = 200$ in the walls assumed above, and an order of magnitude larger than $d = \sqrt{2/3}$. The external stress $\tau = -1/40$ (Dogge 2014, §2.4.2) is applied to the system. This shear loading drives wall motion and transport in the direction of the boundary. Loss of mobility in the boundary region as modeled by $m(x) = f(x; a, p = 5h)$ from (7.20) then leads to wall pile-up there and an inhomogeneous distribution.

Given the converged behavior of numerical convolution demonstrated in Figure 7.3, consider the dependence of numerical transport and pile-up results on N shown in Figure 7.4. As can be seen on the left,

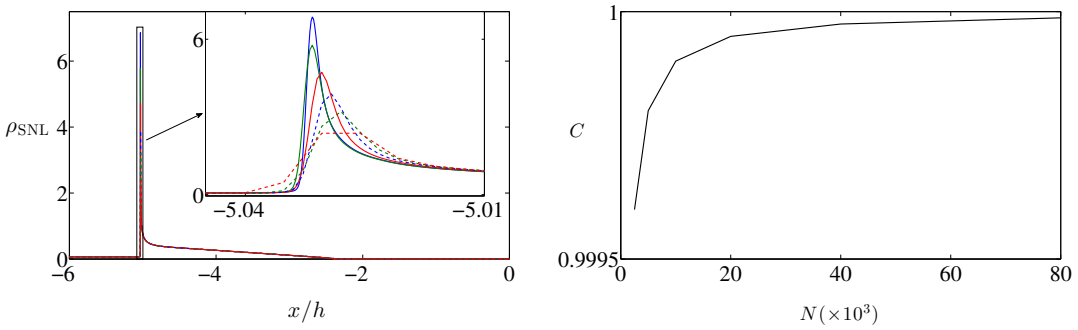


Figure 7.4: Dependence of pile-up distribution and dislocation number conservation on grid size N. Left: dislocation density profiles for $\tau = -1/40$, $m(x) = f(x; ah = 200, p = 5h)$, and variable N. In particular, $N = 2500$ (red dashed line), $N = 5000$ (green dashed line), $N = 10000$ (blue dashed line), $N = 20000$ (red solid line), $N = 40000$ (green solid line), $N = 80000$ (blue solid line). Right: dislocation conservation $C = \langle\rho\rangle/\langle\rho_0\rangle$ as a function of N with $\langle f\rangle := \int_{-L}^{L} f(x)\, dx/2L$ the "volume" average. In particular, since ρ_0 is assumed constant, note that $\langle\rho_0\rangle = 2L\rho_0 = 12h\rho_0$.

in all cases, the dislocation density profiles deviate from each other only near the maximum dislocation density. Figure 7.4 (right) shows the dependence of dislocation conservation on grid size N. Convergence is clearly indicated. Consequently, although convergence of the maximum dislocation density is not clear (as discussed in more detail in 7.B), its effect on conservation appears to be negligible. Based on these results, $N = 5000$ is used for all simulations to follow.

With a converged solution in hand, we are in a position to investigate the effects of various model parameters on transport and pile-up behavior. To begin, however, consider the dynamic model behavior as depicted in Figure 7.5. As shown, redistribution due to interaction and transport results in the successive relaxation of initially sharp pile-up into a steady-state distribution characterized by strong non-linearity

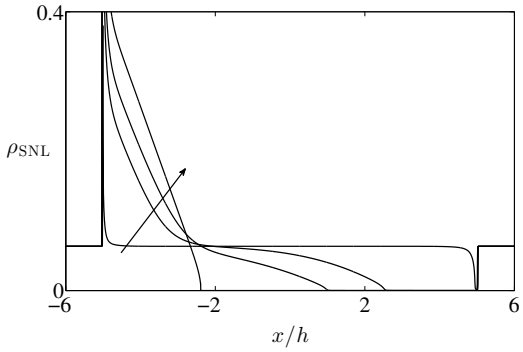


Figure 7.5: Results for the evolution (as indicated by the arrow) of an initially uniform dislocation distribution over $[-6h, 6h]$ during loading as based on $\sigma^{\mathrm{PN}}_{\mathrm{SNL}}$ and $ah = 200$. See text for details.

next to the wall (left) transitioning into an apparently linear region away from the wall in the bulk. As will be shown in more detail in what follows, these can be associated with $1/\sqrt{x}$- and x-based dependencies, respectively, of $\rho(x)$. Next, we turn to the effect of boundary conditions on the pile-up behavior. This is investigated in Figure 7.6. As expected, the dislocation "penetration depth" increases, and the maximum

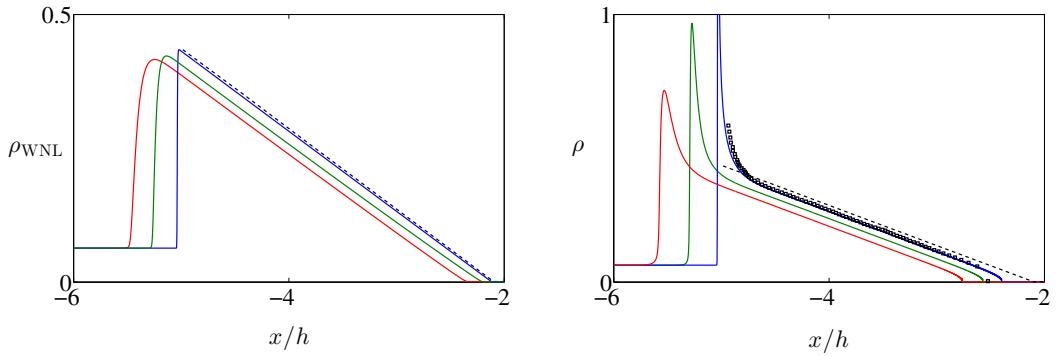


Figure 7.6: Pile-up distribution resulting from wall transport driven by the external stress $\tau = -1/40$ (Dogge 2014, §2.4.2) and wall interaction based on $\sigma^{\mathrm{PN}}_{\mathrm{WNL}}$ (left) and $\sigma^{\mathrm{PN}}_{\mathrm{SNL}}$ (right) for $m(x) = f(x; a, p = 5h)$ with $ah = 10$ (red), $ah = 20$ (green), $ah = 200$ (blue). Shown for comparison is the result (dashed line) of (Dogge 2014, §2.4.2) based on $\sigma^{\mathrm{V}}_{\mathrm{WNL}}$ from (7.12) assuming an impenetrable boundary ($a = \infty$) and the pile-up distribution in *discrete* ensembles of (Volterra-based) walls (e.g., Roy et al. 2008, de Geus et al. 2013) (hollow squares). See text for details.

pile-up density $\rho_{\max}$ decreases, as the boundary width $1/a$ increases. As seen in Figure 7.6 (left), away from the boundary, the PN-WNL density profile for the sharpest boundary (blue curve, $ah = 200$) agrees with Volterra-WNL results of (Dogge 2014, §2.4.2) (dashed line). Analogous results for the PN-SNL case are shown in Figure 7.6 (right). In contrast to the WNL case, $\rho(x)$ is non-linear next to the boundary and in the tail region, and linear in between. Note that the PN (blue curve) and continuous Volterra results (dashed curve) for $\rho(x)$ in Figure 7.6 (right) converge for a spacing of $1/\rho \geqslant 2$ (this compares with $d = \sqrt{2}/\sqrt{3}$). This agrees with a corresponding convergence of the stress profiles. Functional forms $y(x)$ fit to $\rho^{\mathrm{PN}}_{\mathrm{SNL}}(x)$ are shown in Figure 7.7 (right). For comparison, analogous fits to the Volterra-based discrete wall modeling results of Roy et al. (2008) and de Geus et al. (2013) are shown in Figure 7.7 (left).

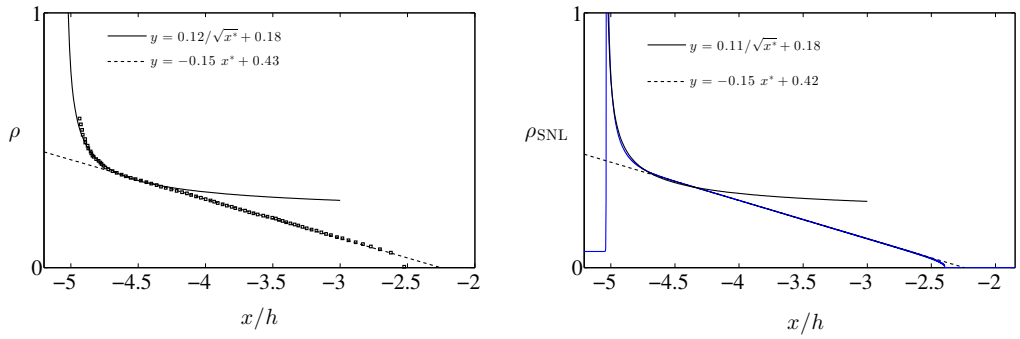


Figure 7.7: Left: best fits to the discrete Volterra-based results of Roy et al. (2008). Right: analogous best fits to the current PN-SNL results. In both cases, note that $x^* = x/h + 5.04$. See text for details.

In particular, the $1/\sqrt{x}$ distribution next to the boundary predicted in both cases agrees well.

7.6.4 Effect of loading and initial distribution

As mentioned in the previous section, the initial dislocation distribution is $\rho_1(t = 0, x) = \rho_0$ everywhere including $x > 5h$ or $x < -5h$. This is different than what is assumed in (Dogge 2014, §2.4.2) where the system is not periodic and basically everything is zero out of the region of interest, $x \in [-5h, 5h]$. To discuss this, the previous case is compared with the case where $\rho_2(t = 0, x) = \rho_0 f(x; ah = 200, p = 5h)$ with $f(x; a, p)$ defined in (7.20) with the same ρ_0 and loading conditions as before. The resulting dislocation distributions are shown in Figure 7.8 (left). The uniform (blue curve) distribution is the same

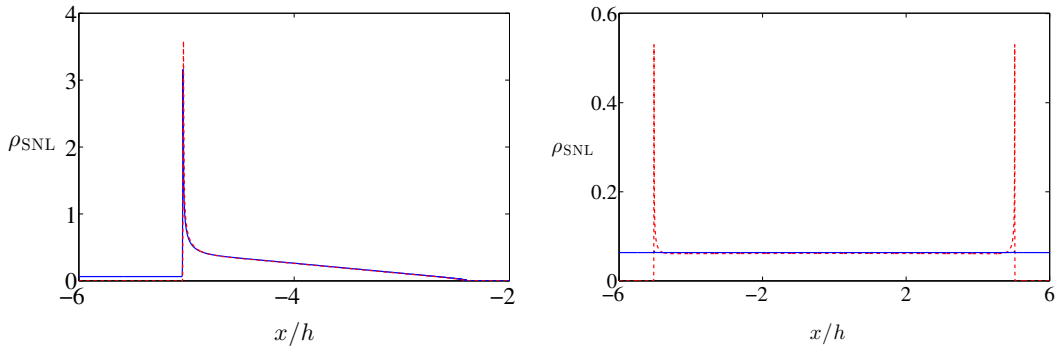


Figure 7.8: Pile-up of interacting dislocations under external loading (left) and without external loading (right) for uniform (blue solid curve) and non-uniform (red dashed curve) initial dislocation densities. See text for details.

as in Figure 7.6 (right). As can be seen, the pile-up profiles in both cases agree well with each other. The only visible difference is the higher peak density value for the non-uniform case (red). To understand this better, consider the case of no external loading (i.e., $\tau = 0$). The results are shown in Figure 7.8 (right). As expected, in the uniform (blue) case, there is no pile-up under zero loading. On the other hand, a non-uniform initial distribution like the red curve is unstable and leads to pile-up. This is due to the fact that a zero dislocation density outside the region of interest acts as a pseudo free surface and

attracts dislocations. This effect is particularly strong in the current case of SNL interactions; dislocations are attracted to the pseudo free-surface beyond $x \in [-5h, 5h]$ even though there is no external loading. This is analogous to the interaction of dislocations and free surfaces via image forces (e.g., Hirth & Lothe 1982, Chapter 5). The extra dislocation pile-up due to the free surface effect in the SNL case (Figure 7.8, right) has roughly the same magnitude as the difference in the dislocation peaks in the pile-up under loading (Figure 7.8, left). In contrast, the WNL-based results comparable to those in Figure 7.8 (right) do not exhibit any pile-up due to the free surface effect, apparently due to the short-range nature of the WNL-based non-zero density gradient and corresponding internal stress. In any case, To eliminate free-surface effects, the uniform (blue) distribution is employed in the rest of this work, facilitating the investigation of purely load driven pile-up of the dislocations.

7.6.5 Comparison of SNL- and WNL-based density and stress fields

Next, consider the internal stress at the boundary predicted by the WNL and SNL models. For completeness, both smooth (i.e., $m(x) = f(x; ah = 10, p = 5h)$) and sharp (i.e., $m(x) = f(x; ah = 200, p = 5h)$) boundaries are considered here. Results for these cases based on the WNL (7.11) and SNL (7.8) models are displayed in Figures 7.9 and 7.10, respectively.

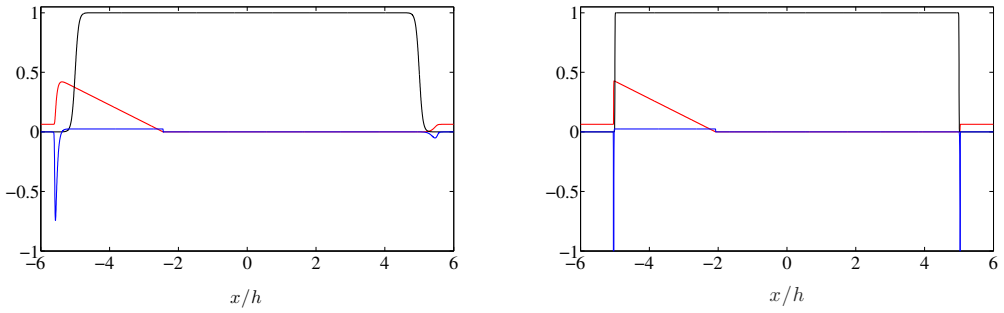


Figure 7.9: Dislocation density (red) and internal stress (blue), profiles based on $\sigma^{\mathrm{PN}}_{\mathrm{WNL}}$ from (7.11) for $\tau = -1/40$ and mobility profiles (black) $ah = 10$ (left) and $ah = 200$ (right). For better visualization, the internal stress curve (blue) on the right is clipped. The internal stress has a "maximum" at about -0.75 (left) in the smooth, and -8.5 (right) in the sharp, case.

Consistent with the results in Figure 7.2, note that the WNL-based model (Figure 7.9) generally predicts more localized stress fields of higher magnitude than the SNL-based model (Figure 7.10). This is in part due to the much greater sensitivity of the WNL-based internal stress to the sharpness of the mobility profile. Again, this is analogous and related to the sensitivity of the stress to the dislocation density profile sharpness already discussed in Section 7.6.2.

Comparing Figures 7.9 and 7.10, one sees that, although the SNL-based density is higher, the corresponding internal stress is lower, than its WNL counterpart. To be more precise, in the case of the smooth boundary (left), the SNL-based maximum density is about 1.7 times higher than that predicted by the WNL model. On the other hand, the SNL-based internal stress is about 0.4 times that of the WNL-based one. Given that SNL-based modeling is more realistic, this would imply that WNL-based modeling overestimates the internal stress at such boundaries. Since they are also of WNL type, this may be the case for models based on strain gradients and gradient plasticity as well.

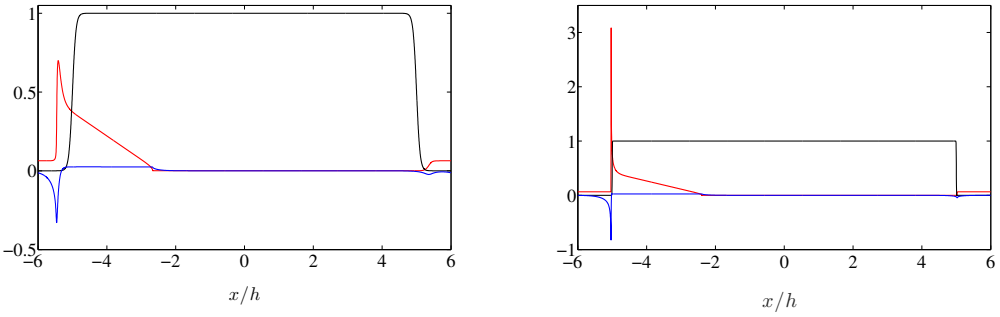


Figure 7.10: Dislocation density (red) and internal stress (blue), profiles based on $\sigma_{\mathrm{SNL}}^{\mathrm{PN}}$ from (7.8) for $\tau = -1/40$ and mobility profiles (black) $ah = 10$ (left) and $ah = 200$ (right).

7.6.6 Effect of glide-plane spacing

Up to this point, all results have been obtained for fixed glide-plane spacing $d = \sqrt{2/3}$ corresponding to Al (fcc). For completeness, we close by briefly examining the effect of varying d on the pile-up behavior. The corresponding results are shown in Figure 7.11.

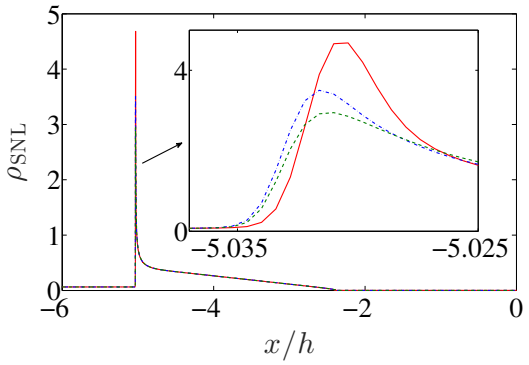


Figure 7.11: Pile-up distribution for $\tau = -1/40$, $m(x) = f(x; ah = 200, p = 5h)$, $N = 20000$, and different glide-plane spacings: $d = \sqrt{2/3}$ (red line), $d = \frac{1}{2}\sqrt{2/3}$ (blue dashed line), $d = \frac{1}{4}\sqrt{2/3}$ (green dashed line). See text for details.

As evident, both the maximum pile-up density $\rho_{\max}$ and shape of the density profile around the maximum are sensitive to d; in particular, $\rho_{\max}$ decreases for decreasing d. (analogous to the effect of increasing boundary width: Figure 7.6). In other words, the minimum spacing $1/\rho_{\max}$ between walls in the pile-up increases with decreasing d. This is explained by the fact that, as shown in Figure 7.1, the dislocation stress field increases for decreasing d, resulting in a more repulsive interaction between adjacent walls in the pile-up. Consequently, in the extreme case $d \to 0$ corresponding to the continuum Volterra model (see Appendix 7.A), $\rho_{\max}$ is minimal, and $1/\rho_{\max}$ maximal.

7.7 Conclusion

A model for transport and strongly non-local interaction of infinite discrete dislocations walls has been developed in this work. In contrast to previous analogous work based on the Volterra model, the current model formulation is based on the more physical Peierls-Nabarro (PN) dislocation model (e.g., Hirth & Lothe 1982, Chapter 8). For simplicity, attention is restricted to walls consisting of single-sign dislocations and continuous wall distributions with respect to a single glide plane. In this context, the influence of strongly non-local (SNL; long-range) interaction, and its approximation as weakly non-local (WNL; short-range), on wall transport and distribution are studied in the context of interaction- and external-loading-driven pile-up at a boundary. The pile-up distribution predicted by the current PN-SNL-based continuous distribution modeling agrees both qualitatively and quantitatively quite well with that predicted by Volterra-based discrete distribution modeling (e.g., Roy et al. 2008, de Geus et al. 2013). In particular, this is true for the non-linear distribution next to the wall and in the tail of $\rho(x)$. Between these two regimes in the linear part of the distribution, the WNL-based results agree well with the corresponding SNL-based ones. The deviation of WNL- and SNL-based results near the boundary and in the tail could be related for example to the breakdown of shielding or screening effects (e.g., Groma et al. 2006) in these regions. As such, it is important to account for the SNL nature of the interaction near the boundary. In any case, it is fair to conclude that the interaction of dislocations in a single-sign discrete distribution is inherently SNL in nature.

APPENDIX

7.A Comparison of selected Peierls-Nabarro- and Volterra-based relations

The purpose of this appendix is to document the connection between selected Peierls-Nabarro (PN) model relations and their counterparts in the generally more familiar Volterra model. For example,

$$\sigma_0^{\mathrm{V}}(x,y) = \lim_{d\to 0} \sigma_0^{\mathrm{PN}}(x,y) = \frac{1}{2\pi}\,\frac{x(x^2-y^2)}{(x^2+y^2)^2}\,, \tag{7.21}$$

(e.g., Hirth & Lothe 1982, Equation (3-43)); these are compared in Figure 7.A.1.

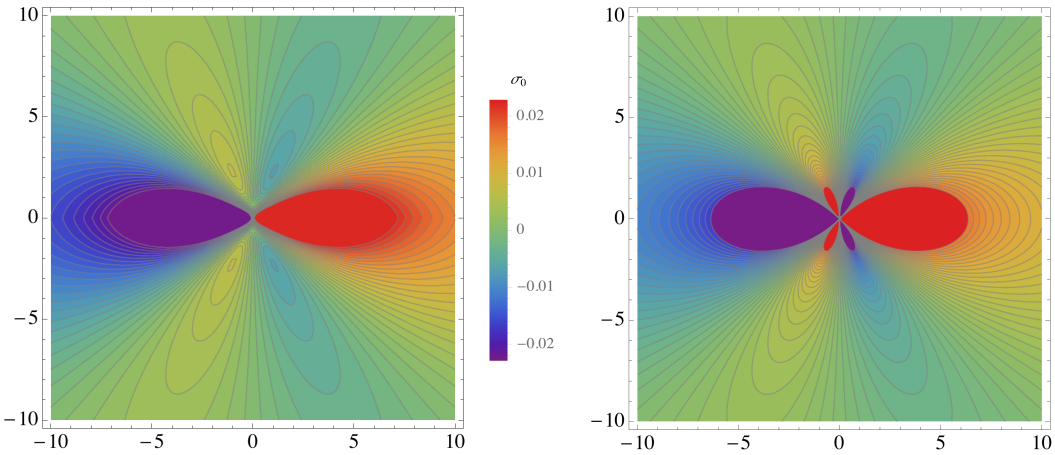


Figure 7.A.1: Shear stress fields $\sigma_0^{\mathrm{PN}}(x,y)$ (left) for $d = \sqrt{2/3}$ and $\sigma_0^{\mathrm{V}}(x,y)$ (right) (x and y are scaled by b). Both fields are clipped for display purposes.

In particular, each of these follow from the corresponding PN relation in the limit $d \to 0$ of zero glide-plane spacing. Likewise, the PN wall stress $\sigma_{\mathrm{w}}^{\mathrm{PN}}(x)$ from (7.7) reduces to the well-known form

$$\sigma_{\mathrm{w}}^{\mathrm{V}}(x) = \lim_{d\to 0} \sigma_{\mathrm{w}}^{\mathrm{PN}}(x) = \frac{1}{2h}\,\frac{\pi x}{h}\,\mathrm{csch}^2\left(\frac{\pi x}{h}\right)\,, \tag{7.22}$$

in the Volterra model. Such stress field models can be expressed in Eshelby stress-like form, i.e., $\sigma_{\mathrm{w}}(x) = -\partial_x E_{\mathrm{w}}(x)$, in terms of a corresponding energy $E_{\mathrm{w}}(x)$. In particular, we have

$$\begin{aligned} E_{\mathrm{w}}^{\mathrm{PN}}(x) &= \frac{1}{2\pi}\left\{1 + \log\frac{h\,|\Gamma(\zeta_{h,c}(x))|^2}{2\pi\sqrt{x^2+c^2}}\right\} \\ &+ \frac{x}{\pi h}\,\Im\,\psi^{(0)}(\zeta_{h,c}(x)) + \frac{c}{\pi h}\{1 - \Re\,\psi^{(0)}(\zeta_{h,c}(x))\}\,, \end{aligned} \tag{7.23}$$

in the context of the PN model, and the more well-known analogous relation

$$E_{\mathrm{w}}^{\mathrm{V}}(x) = \frac{1}{2\pi}\,\Re\left\{\frac{\pi x}{h}\,\coth\left(\frac{\pi x}{h}\right) - \ln\left(2\sinh\left(\frac{\pi x}{h}\right)\right)\right\}\,, \tag{7.24}$$

in the Volterra model (e.g. Scardia et al. 2014). Here, $\Gamma(z)$ is the Gamma function. To obtain (7.23) and (7.24) from the respective stress relations, the integration constant was chosen such that $\lim_{x\to\pm\infty} E_{\mathrm{w}}(x) = 0$. In contrast to the corresponding stresses (7.22), note that $E_{\mathrm{w}}^{\mathrm{V}}(x)$ and $\lim_{d\to 0} E_{\mathrm{w}}^{\mathrm{PN}}(x)$ are not equal, but differ rather by a constant. The Volterra-based energy model $E_{\mathrm{w}}^{\mathrm{V}}$ from (7.24) is the starting point for a number of works, e.g., that Scardia et al. (2014) on energy coarse-graining via Γ-convergence in the continuum limit as the number of walls $n \to \infty$.

7.B Characterization of the SNL-based maximum dislocation density

The purpose of this appendix is to document the dependence of the maximum density $\rho_{\mathrm{SNL}}^{\max}$ on grid size N. This is shown for the same external loading and two different boundary conditions in Figure 7.B.1 and in Figure 7.B.2. In particular, the results for a sharp boundary $m(x) = f(x; ah = 200, p = 5h)$ shown in Figure 7.B.1 fit to a power-law relation of the form $\rho_{\mathrm{SNL}}^{\max} = 0.29N^{0.28}$ (R-squared of 0.9943) for the range of grid sizes investigated. Analogously, those for the softer boundary $m(x) = f(x; ah = 10, p = 5h)$ in Figure 7.B.2 follow $\rho_{\mathrm{SNL}}^{\max} = 0.62N^{0.012}$ (R-squared of 0.94), again in the range of grid sizes N investigated. In this range, then, convergence of $\rho_{\mathrm{SNL}}^{\max} \to \infty$ is not achieved. On the other hand, the results in both figures (left) imply that the curves are converging just to the left (about $0.02h$) of the peak density. Further insight into this issue represents work in progress to be reported on in the future.

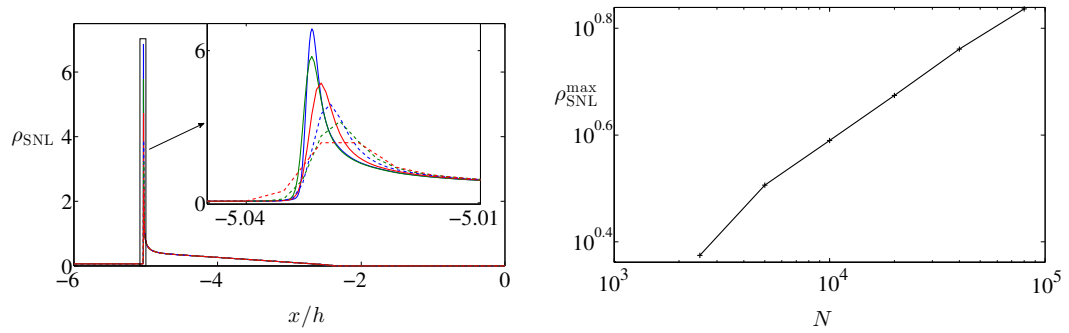


Figure 7.B.1: Effect of numerical resolution on pile-up distribution. Left: dislocation density profile for $N = 2500$ (red dashed line), $N = 5000$ (green dashed line), $N = 10000$ (blue dashed line), $N = 20000$ (red solid line), $N = 40000$ (green solid line), $N = 80000$ (blue solid line). In all cases, $\tau = 1/40$ and $m(x) = f(x; ah = 200, p = 5h)$. Right: log-log plot of maximum density as a function of N.

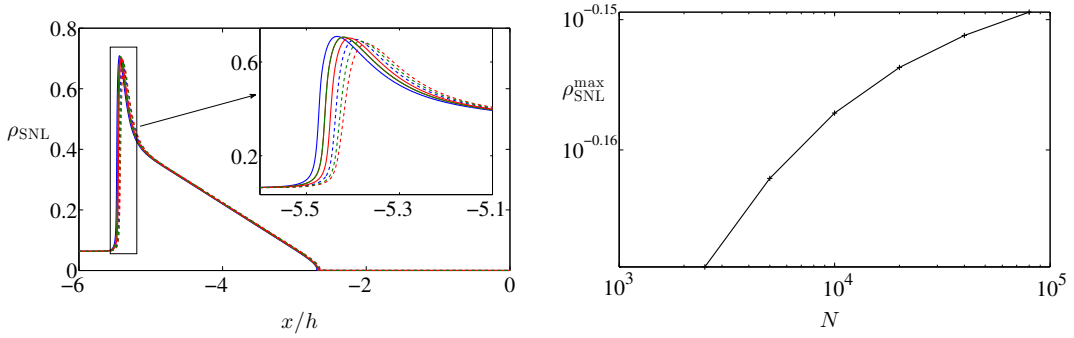


Figure 7.B.2: Same as in Figure 7.B.1 except for the boundary condition $m(x) = f(x; ah = 10, p = 5h)$.

CHAPTER 8

CONCLUSION

Several properties and phenomena involving dislocations in fcc metals are studied in this work. These range from atomistic calculations up to continuum level models. The connection between the atomistic and the continuum model is kept alive. Temperature-dependence of the stacking fault free energy (SFFE) for Fe is calculated with the help of the thermodynamic integration with the quasi-harmonic approximation and molecular dynamics (MD) simulations based on the bond order potential of Müller et al. (2007). The SFFE of Fe at 0 K is calculated to be -20 mJ/m^2, negative due to the fact that the fcc phase is unstable at this temperature. The SFFE increases with temperature and becomes positive at around 200 K. Depending on system size, an SFFE for Fe between 5.5 and 9.1 mJ/m^2 is obtained at 298 K, increasing to between 70 and 80 mJ/m^2 at 1000 K. Next, the interaction between dislocations and stacking faults at low temperatures is studied with the help of MD. Observed interaction types in Cu include annihilation, penetration, and growth. Of particular importance is the mixed screw-edge character of the partial dislocations involved and the fact that the screw part cross slips more easily than its edge counterpart. The interaction of curved dislocations with twinned crystal is also studied with MD. In two of the in-plane shear loading directions, jerky stress flow is observed. Upon closer investigation, the jerky behavior is related to the fast motion of twin boundary. In the continuum part of the dissertation, the Peierls-Nabarro (PN) and Volterra (V) dislocation models are employed for dislocation-mediated bulk twin nucleation and growth. The dynamic model is applied to the modeling of variable dislocation separation in the twin. In this context, dislocations are closest together at the twin tip and increase in separation away from the tip. The phase field model for dislocation is based in particular on periodic microelasticity (Wang et al. 2001, Bulatov & Cai 2006, Wang & Li 2010) to model the strongly non-local elastic interaction of dislocation lines via their (residual) strain fields. The energy storage is modeled here with the help of the ”interface” energy concept and model of Cahn & Hilliard (1958) (see also Allen & Cahn 1979, Wang & Li 2010). The current approach is applied to determine the phase field free energy for Al and Cu. The identified models are then applied to modeling of dislocation dissociation, stacking fault formation, glide and dislocation reactions in these materials. Transport and pile-up of infinite discrete dislocation walls driven by non-local interaction and external loading is also studied. The underlying model for dislocation wall interaction is based on the non-singular PN model. The influence of strongly non-local (SNL; long-range)

interaction, and its approximation as weakly non-local (WNL; short-range), are studied. The pile-up behavior predicted by the current SNL-based continuous wall distribution modeling is consistent with that predicted by discrete wall distribution modeling (e.g., Roy et al. 2008, de Geus et al. 2013). Both deviate substantially from the pile-up behavior predicted by WNL-based continuous wall distribution modeling (e.g., Dogge 2014, Chapter 2).

BIBLIOGRAPHY

Aghababaei, R., Joshi, S. P. & Reddy, J. N. (2011), 'Nonlocal continuum crystal plasticity with internal residual stresses', *Journal of the Mechanics and Physics of Solids* **59**, 713–731.

Allen, S. M. & Cahn, J. W. (1979), 'A macroscopic theory for antiphase boundary motion and its application to antiphase domain coarsening', *Acta Metallurgica* **27**, 1085–1095.

Arsenlis, A. & Parks, D. M. (2002), 'Modeling the evolution of the crystallographic dislocation density in crystal plasticity', *Journal of the Mechanics and Physics of Solids* **50**, 1979–2009.

Aubry, S., Kang, K., Ryu, S. & Cai, W. (2011), 'Energy barrier for homogeneous dislocation nucleation: Comparing atomistic and continuum models', *Scripta Materialia* **64**(11), 1043–1046.

Balluffi, R. W. (2012), *Introduction to Elasticity for Crystal Defects*, Cambridge University Press.

Baskaran, R., Akarapu, S., Mesarovic, S. D. & Zbib, H. M. (2010), 'Energies and distributions of dislocations in stacked pile-ups', *International Journal of Solids and Structures* **47**, 1144–1153.

Beigmohamadi, M., Mayer, J., Mosecker, L., Mianroodi, J. R., Svendsen, B., Pierce, D. & Wittig, J. (2014), Atomic resolution investigation of twin boundaries in Fe-Cr-Mn austenitic TWIP steels with aberration-corrected transmission electron microscopy and real-space strain field calculation, *in* '18th International Microscopy Congress', Prague, Czech Republic.

Bitzek, E., Gahler, F., Koskinen, P., Moseler, M. & Gumbsch, P. (2006), 'Structural relaxation made simple', *Physical Review Letters* **97**, 170201.

Bouaziz, O., Allain, S., Scott, C., Cugy, P. & Barbier, D. (2011), 'High manganese austenitic twinning induced plasticity steels: A review of the microstructure properties relationships', *Current Opinion in Solid State and Materials Science* **15**(4), 141–168.

Boyer, R. D., Li, J., Ogata, S. & Yip, S. (2004), 'Analysis of shear deformations in Al and Cu: empirical potentials versus density functional theory', *Modelling and Simulation in Materials Science and Engineering* **12**(5), 1017–1029.

Bracewell, R. N. (2000), *The Fourier Transform and Its Application*, 3rd edn, McGraw-Hill.

Brown, C. M., Dreyer, W. & Müller, W. (2002), 'Discrete fourier transforms and their application to stress-strain problems in composite mechanics: a convergence study', *Proceedings of the Royal Society of London A* **458**, 1967–1987.

Bulatov, V. & Cai, W. (2006), *Computer simulations of dislocations*, Oxford University Press.

Cahn, J. W. & Hilliard, J. E. (1958), 'Free energy of a non-uniform system. i. interfacial energy.', *Journal of Chemical Physics* **28**, 258–267.

Cai, W., Arsenlis, A., Weinberger, C. R. & Bulatov, V. V. (2006), 'A non-singular continuum theory of dislocations', *Journal of the Mechanics and Physics of Solids* **54**, 561–587.

Canuto, C., Hussaini, M. Y., Quateroni, A. & Zang, T. A. (1988), *Spectral Methods in Fluid Dynamics*, Springer Series in Computational Physics, Springer.

Chen, L. Q. & Shen, J. (1998), 'Applications of semi-implicit fourier-spectral method to phase field equations', *Computer Physics Communications* **108**, 147–158.

Chen, M., Ma, E., Hemker, K. J., Sheng, H., Wang, Y. & Cheng, X. (2003), 'Deformation twinning in nanocrystalline aluminum.', *Science* **300**(5623), 1275–7.

Cheng, B. & Ngan, A. H. (2013), 'Crystal plasticity of Cu nanocrystals during collision', *Materials Science and Engineering: A* **585**, 326–334.

Christian, J. W. & Mahajan, S. (1995), 'Deformation twinning', *Progress in Materials Science* **39**, 1–157.

Clouet, E. (2009), 'Elastic energy of a straight dislocation and contribution from core tractions', *Philosophical Magazine* **89**, 1–17.

Cooper, R. (1965), 'The equilibrium shape of deformation twins', *Acta Metallurgica* **13**(1), 46–48.

Davis, H. T. (1996), *Statistical Mechanics of Phases, Interfaces, and Thin Films*, Advances in Interfacial Engineering Series, Wiley-VCH, New York, chapter 9.1: Calculus of variations and functional derivatives, pp. 425–435.

de Geus, T., Peerlings, R. H. J. & Hirschberger, C. (2013), 'An analysis of the pile-up of infinite periodic walls of edge dislocations', *Mechanical Research Communications* **54**, 7–13.

Dogge, M. M. W. (2014), Mechanics of phase boundaries in multi-phase steels, PhD thesis, TU Eindhoven.

Dreyer, W. & Müller, W. (2000), 'A study of the coarsening of tin/lead solders', *International Journal of Solids and Structures* **37**, 3841–3871.

Eisenlohr, P., Diehl, M., Lebensohn, R. A. & Roters, F. (2013), 'A spectral method solution to crystal elasto viscoplasticity at finite strains', *International Journal of Plasticity* **46**, 37–53.

Eshelby, J. (1961), 'Elastic inclusions and inhomogeneities', *Progress in Solid Mechanics* **2**, 89–140.

Eshelby, J. D. (1949), 'Edge dislocations in anisotropic materials', *Philosophical Magazine* **40**(308), 903–912.

Eshelby, J. D. (1970), Energy relations and the energy-momentum tensor in continuum mechanics, *in* M. Kanninen, W. Alder, A. Rosenfeld & R. Jaffe, eds, 'Inelastic behavior in solids', Academic Press, pp. 77–115.

Eshelby, J. D., Read, W. T. & Shockley, W. (1953), 'Anisotropic elasticity with application to dislocation theory', *Acta Metallurgica* **1**, 251–259.

Evans, R. (1979), 'The nature of the liquid-vapour interface and other topics in the statistical mechanics of non-uniform, classical fluids', *Advances in Physics* **28**, 143–200.

Ezaz, T., Sangid, M. D. & Sehitoglu, H. (2011), 'Energy barriers associated with slip twin interactions', *Philosophical Magazine* **91**(10), 1464–1488.

Forman, A. J. N. (1955), 'Dislocation energies in anisotropic crystals', *Acta Metallurgica* **3**, 322–330.

Frenkel, D., Klein, M., Parrinello, M. & Smit, B. (2002), *Underestanding Molecular Dynamics from Algorithm to Applications*, Academic Press.

Gottlieb, D. & Orszag, S. A. (1977), *Numerical Analysis of Spectral Methods: Theory and Application*, SIAM.

Gradshteyn, I. S. & Ryzhik, I. M. (1980), *Tables of Integrals, Series and Products*, Academic Press.

Groma, I., Csikor, F. F. & Zaiser, M. (2003), 'Spatial correlations and higher-order gradient terms in a continuum description of dislocation dynamics', *Acta Materialia* **51**, 1271–1281.

Groma, I., Györgyi, G. & Ispánovity, P. D. (2010), 'Variational approach in dislocation theory', *Philosophical Magazine* **90**, 3679–3695.

Groma, I., Györgyi, G. & Kocsis, B. (2006), 'Debye screening of dislocations', *Physical Review Letters* **96**, 165503.

Henderson, A. (2007), Paraview guide, a parallel visualization application, Kitware Inc.

Hirth, J. & Lothe, J. (1982), *Theory of dislocations*, John Wiley and Sons, New York.

Hochrainer, T., Zaiser, M. & Gumbsch, P. (2007), 'A three-dimensional continuum theory of dislocation systems: kinematics and mean-field formulation', *Philosophical Magazine* **87**, 1261–1282.

Hu, Q., Li, L. & Ghoniem, N. (2009), 'Stick–slip dynamics of coherent twin boundaries in copper', *Acta Materialia* **57**(16), 4866–4873.

Hu, S., Henager, C. H. & Chen, L. (2010), 'Simulations of stress-induced twinning and de-twinning: A phase field model', *Acta Materialia* **58**(19), 6554–6564.

Hunter, A., Beyerlein, I. J., Germann, T. C. & Koslowski, M. (2011), 'Influence of the stacking fault energy surface on partial dislocations in fcc metals with a three dimensional phase field dynamics model', *Physical Review B* **84**, 144108.

Hunter, A., Zhang, R. F., Beyerlein, I. J., Germann, T. C. & Koslowski, M. (2013), 'Dependence of equilibrium stacking fault width in fcc metals on the gamma-surface', *Modelling and Simulation in Materials Science and Engineering* **21**, 025015 (19pp).

Iyer, M., Radhakrishnan, B. & Gavini, V. (2015), 'Electronic-structure study of an edge dislocation in aluminum and the role of macroscopic deformations on its energetics', *Journal of the Mechanics and Physics of Solids* p. in press.

Jin, Z.-H., Gumbsch, P., Albe, K., Ma, E., Lu, K., Gleiter, H. & Hahn, H. (2008), 'Interactions between non-screw lattice dislocations and coherent twin boundaries in face-centered cubic metals', *Acta Materialia* **56**(5), 1126–1135.

Jin, Z.-H., Gumbsch, P., Ma, E., Albe, K., Lu, K., Hahn, H. & Gleiter, H. (2006), 'The interaction mechanism of screw dislocations with coherent twin boundaries in different face-centred cubic metals', *Scripta Materialia* **54**(6), 1163–1168.

Khachaturyan, A. G. (1983), *Theory of Structural Transformations in Solids*, John Wiley.

Khachaturyan, A. G., Semenovskaya, S. & Tsakalakos, T. (1995), 'Elastic strain energy of inhomogeneous solids', *Physical Review B* **52**(22), 15909–15919.

Kibey, S., Liu, J., Johnson, D. & Sehitoglu, H. (2007), 'Predicting twinning stress in fcc metals: Linking twin-energy pathways to twin nucleation', *Acta Materialia* **55**(20), 6843–6851.

Kooiman, M., Hütter, M. & Geers, M. G. D. (2015), 'Microscopically derived free energy of dislocations', *Journal of the Mechanics and Physics of Solids* **78**, 186–209.

Körmann, F., Dick, A., Grabowski, B., Hickel, T. & Neugebauer, J. (2012), 'Atomic forces at finite magnetic temperatures: Phonons in paramagnetic iron', *Physical Review B - Condensed Matter and Materials Physics* **85**(12), 1–5.

Kröner, E. (1959), 'Allgemeine Theorie der Versetzungen und Eigenspannungen', *Archive for Rational Mechanics and Analysis* **4**((Supplement 1)), 273–334.

Kwon, O. J., Lee, K. Y., Kim, G. S. & Chin, K. G. (2010), 'New Trends in Advanced High Strength Steel Developments for Automotive Application', *Materials Science Forum* **638-642**, 136–141.

Landau, L. D. & Lifshitz, E. M. (1970), *Theory of Elasticity*, second edn, Pergamon.

Lazar, M. (2013), 'The fundamentals of non-singular dislocations in the theory of gradient elasticity: dislocation loops and straight dislocations', *International Journal of Solids and Structures* **50**, 352–362.

Li, B. Q., Sui, M. L. & Mao, S. X. (2011), 'Twinnability prediction for fcc metals', *Journal of Material Science and Technology* **27**, 97–100.

Li, S. & Wang, G. (2008), *Introduction to Micromechanics and Nanomechanics*, World Scientific.

Liang, X. (2014), 'Scaling of stacking fault energy and deformation temperature on strain hardening of fcc metals and alloys', *Philosophical Magazine Letters* **94**, 556–563.

Liu, L., Wang, R., Wu, X., Gan, L. & Wei, Q. (2014), 'Temperature effects on the generalized planar fault energies and twinnabilities of Al, Ni and Cu: First principles calculations', *Computational Materials Science* **88**, 124–130.

Mesarovic, S. (2005), 'Energy, configurational forces and characteristic lengths associated with the continuum of geometrically necessary dislocations', *International Journal of Plasticity* **21**, 1855–1889.

Mesarovic, S., Baskaran, R. & Panchenko, A. (2010), 'Thermodynamic coarsening of dislocation mechanics and the size-dependent continuum crystal plasticity', *Journal of the Mechanics and Physics of Solids* **58**, 311–329.

Mianroodi, J. R., Azmi, R. & Svendsen, B. (2016), 'Effects of twinning on stress-strain behavior and strain hardening in fcc metals', *in prepration* .

Mianroodi, J. R., Peerlings, R. & Svendsen, B. (2016), 'Strongly non-local modeling of dislocation transport and pile-up', *submitted to Philosophical Magazine* .

Mianroodi, J. R. & Svendsen, B. (2015), 'Atomistically determined phase-field modeling of dislocation dissociation, stacking fault formation, dislocation slip, and reactions in fcc systems', *Journal of the Mechanics and Physics of Solids* **77**, 109 – 122.

Mianroodi, J. R. & Svendsen, B. (2016*a*), 'Molecular-dynamics-based modeling of the stacking fault free energy of fe at finite temperature', *in prepration* .

Mianroodi, J. R. & Svendsen, B. (2016*b*), 'Molecular dynamics modeling of dislocation-stacking fault interaction in cu and al', *in prepration* .

Mianroodi, J. R. & Svendsen, B. (2016*c*), 'Peierls-nabarro- and volterra-based modeling of static and dynamic bulk twinning in fcc systems', *in prepration* .

Mishin, Y., Farkas, D., Mehl, M. & Papaconstantopoulos, D. (1999), 'Interatomic potentials for monoatomic metals from experimental data and ab initio calculations', *Physical Review B* **59**(5).

Mishin, Y., Mehl, M., Papaconstantopoulos, D., Voter, A. & Kress, J. (2001), 'Structural stability and lattice defects in copper: Ab initio, tight-binding, and embedded-atom calculations', *Physical Review B* **63**(22), 1–16.

Moulinec, H. & Suquet, P. (1994), 'A fast numerical method for computing the linear and nonlinear mechanical properties of composites', *Comptes Rendus de l'Académie des Sciences Paris* **318**, 1417–1423.

Müller, M., Erhart, P. & Albe, K. (2007), 'Analytic bond-order potential for bcc and fcc iron—comparison with established embedded-atom method potentials', *Journal of Physics: Condensed Matter* **19**(32), 326220.

Mura, T. (1987), *Micromechanics of Defects in Solids*, Martinus Nijhoff.

Nemat-Nasser, S. & Hori, M. (1999), *Micromechanics: Overall Properties of Heterogeneous Materials*, Elsevier.

Neu, R. W. (2013), 'Performance and Characterization of TWIP Steels for automotive Applications', *Materials Performance and Characterization* **2**(1), 244–284.

Ogata, S., Li, J. & Yip, S. (2005), 'Energy landscape of deformation twinning in bcc and fcc metals', *Physical Review B* **71**(22), 224102.

Orowan, E. (1934), 'Zur kristallplastizität. i', *Zeitschrift für Physik* **89**(9-10), 605–613.

Parrinello, M. & Rahman, A. (1981), 'Polymorphic transitions in single crystals: A new molecular dynamics method', *Journal of Applied Physics* **52**(12), 7182.

Peach, M. & Koehler, J. (1950), 'The forces exerted on dislocations and the stress fields produced by them', *Physical Review* **80**, 436.

Plimpton, S. (1995), 'Fast parallel algorithms for short-range molecular dynamics', *Journal of Computational Physics* **117**(June 1994), 1–42.

Polanyi, M. (1934), 'Über eine art gitterstörung, die einen kristall plastisch machen könnte', *Zeitschrift für Physik* **89**(9-10), 660–664.

Porter, L. J., Yip, S., Yamaguchi, M., Kaburaki, H. & Tang, M. (1997), 'Empirical bond-order potential description of thermodynamic properties of crystalline silicon', *Journal of Applied Physics* **81**(1), 96.

Press, W. H., Teukolsky, S. A., Vetterling, W. T. & Flannery, B. P. (2007), *Numerical Recipies: The Art of Scientific Computing*, third edition edn, Cambridge University Press.

Reina, C., Sandoval, L. & Marian, J. (2014), 'Mesoscale computational study of the nanocrystallization of amorphous Ge via a self-consistent atomistic phase-field model', *Acta Materialia* **77**, 335–351.

Rice, J. (1992), 'Dislocation nucleation from a crack tip: an analysis based on Peierls concept', *Journal of the Mechanics and Physics of Solids* **40**(2), 239–271.

Roy, A., Peerlings, R. H. J., Geers, M. G. D. & Kasyanyuk, Y. (2008), 'Continuum modeling of dislocation interactions: why discreteness matters?', *Materials Science and Engineering A* **486**, 653–661.

Sandfeld, S., Hochrainer, T., Zaiser, M. & Gumbsch, P. (2011), 'Continuum modeling of dislocation plasticity: theory, numerical implementation, and validation by discrete dislocation simulations', *Journal of Materials Research* **26**, 623–632.

Sangid, M. D., Ezaz, T., Sehitoglu, H. & Robertson, I. M. (2011), 'Energy of slip transmission and nucleation at grain boundaries', *Acta Materialia* **59**(1), 283–296.

Scardia, L., Peerlings, R. H. J., Peletier, M. A. & Geers, M. G. D. (2014), 'Mechanics of dislocation pile-ups: a unification of scaling regimes', *Journal of the Mechanics and Physics of Solids* **70**, 42–61.

Schoeck, G. (1994), 'The generalized Peierls-Nabarro model', *Philosophical Magazine A* **69**, 1085–1095.

Schoeck, G. (1997), 'The Peierls dislocation: line energy, line tension, dissociation and deviation', *Acta Materialia* **45**(6), 2597—2605.

Schoeck, G. (2001), 'The core structure, recombination energy and Peierls energy for dislocations in Al', *Philosophical Magazine A* **81**, 1161.

Schoeck, G. (2003), 'The emission of dislocations from crack tips – a critical assessment', *Material Science and Engineering A* **356**, 93–101.

Schoeck, G. (2005), 'The peierls model: progress and limitations', *Material Science and Engineering A* **400-401**, 7–17.

Schoeck, G. (2006), 'The core structure of dislocations: peierls model versus atomic simulations', *Acta Materialia* **54**, 4865–4870.

Schoeck, G. (2014), 'The energy of dislocation dipoles', *Philosophical Magazine* **94**(14), 1–10.

Schulz, K., Dickel, D., Schmitt, S., Sandfeld, S., Weygand, D. & Gumbsch, P. (2014), 'Analysis of dislocation pile-ups using a dislocation-based continuum theory', *Modeling and Simulation in Material Science and Engineering* **22**, 25008–25022(15).

Sedláček, R., Kratochvíl, J. & Werner, E. (2003), 'The importance of being curved: bowing dislocations in a continuum description', *Philosophical Magazine* **83**, 3735–3752.

Sedlmayr, A., Bitzek, E., Gianola, D. S., Richter, G., Mönig, R. & Kraft, O. (2012), 'Existence of two twinning-mediated plastic deformation modes in Au nanowhiskers', *Acta Materialia* **60**(9), 3985–3993.

Shen, C., Ju, L. & Wang, Y. (2014), 'Predicting structure and energy of dislocations and grain boundaries', *Acta Materialia* **74**, 125–131.

Shen, C. & Wang, Y. (2003), 'Phase field modeling of dislocation networks', *Acta Materialia* **51**, 2595–2610.

Shen, C. & Wang, Y. (2004), 'Incorporation of gamma-surface to phase field model of dislocations: simulation dislocation dissociation in fcc crystals', *Acta Materialia* **52**, 683–691.

Steinmetz, D. R., Jäpel, T., Wietbrock, B., Eisenlohr, P., Gutierrez-Urrutia, I., Saeed-Akbari, A., Hickel, T., Roters, F. & Raabe, D. (2013), 'Revealing the strain-hardening behavior of twinning-induced plasticity steels: theory, simulations, experiments', *Acta Materialia* **61**, 494–510.

Stroh, A. N. (1958), 'Dislocations and cracks in anisotropic media', *Philosophical Magazine* **2**, 625–646.

Stukowski, A. (2010), 'Visualization and analysis of atomistic simulation data with OVITO–the Open Visualization Tool', *Modelling and Simulation in Materials Science and Engineering* **18**(1), 015012.

Stukowski, A., Bulatov, V. V. & Arsenlis, A. (2012), 'Automated identification and indexing of dislocations in crystal interfaces', *Modelling and Simulation in Materials Science and Engineering* **20**(8), 085007.

Suquet, P. (1997), *Continuum Micromechanics*, Vol. 377 of *CISM International Center for Mechanical Sciences*, Springer.

Swygenhoven, H. V., Derlet, P. M. & Frøseth, A. G. (2006), 'Nucleation and propagation of dislocation in nanocrystalline fcc metals', *Acta Materialia* **54**, 1975–1983.

Tadmor, E. & Miller, R. (2011), *Modeling materials: continuum, atomistic and multiscale techniques*, Cambridge University Press.

Taylor, G. I. (1934), 'The mechanism of plastic deformation of crystals. part i. theoretical', *Proceedings of the Royal Society of London A: Mathematical, Physical and Engineering Sciences* **145**(855), 362–387.

Teodosiu, C. (1982), *Elastic Theory of Crystals*, North Holland.

Tucker, G. J., Tiwari, S., Zimmerman, J. A. & McDowell, D. L. (2012), 'Investigating the deformation of nanocrystalline copper with microscale kinematic metrics and molecular dynamics', *Journal of the Mechanics and Physics of Solids* **60**(3), 471–486.

Vitek, V. (1968), 'Intrinsic stacking faults in body-centered cubic crystals', *Philosophical Magazine* **18**, 773–786.

Šilhavý, M. (1997), *The Mechanics and Thermodynamics of Continuous Media*, Springer.

Walgraef, D. & Aifantis, E. C. (1985), 'Dislocation patterning in fatigued metals as a result of dynamical instabilities', *Journal of Applied Physics* **58**, 688–691.

Walther, A. & Griewank, A. (2012), Getting started with adol-c, *in* U. Naumann & O. Schenk, eds, 'Combinatorial Scientific Computing', Chapman-Hall CRC Computational Science, chapter 7, pp. 181–202.

Wang, J. & Sehitoglu, H. (2013), 'Twinning stress in shape memory alloys: Theory and experiments', *Acta Materialia* **61**(18), 6790–6801.

Wang, J. & Sehitoglu, H. (2014*a*), 'Dislocation slip and twinning in Ni-based L12 type alloys', *Intermetallics* **52**, 20–31.

Wang, J. & Sehitoglu, H. (2014*b*), 'Modelling of martensite slip and twinning in NiTiHf shape memory alloys', *Philosophical Magazine* **94**(20), 2297–2317.

Wang, Y. & Li, J. (2010), 'Phase field modeling of defects and deformation', *Acta Materialia* **58**, 1212–1235.

Wang, Y. U., Jin, Y. M., Cutiño, A. M. & Khachaturyan, A. G. (2001), 'Nanoscale phase field microelasticity theory of dislocations: model and 3d simulations', *Acta Materialia* **49**, 1847–1857.

Wei, H. & Wei, Y. (2012), 'Interaction between a screw dislocation and stacking faults in FCC metals', *Materials Science and Engineering: A* **541**, 38–44.

Woodward, C., Trinkle, D. R., Hector, L. G. & Olmsted, D. L. (2008), 'Prediction of dislocation cores in aluminum from density functional theory', *Physical Review Letters* **100**, 045507.

Wu, K.-A., Adland, A. & Karma, A. (2010), 'Phase-field-crystal model for fcc ordering', *Physical Review E* **81**, 061601.

Xiang, Y., Wei, H., Ming, P. & E, W. (2008), 'A generalized Peirls-Nabarro model for curved dislocations and core structures of dislocation loops in Al and Cu', *Acta Materialia* **56**, 1447–1460.

Zimmerman, J. A., Gao, H. & Abraham, F. F. (2000), 'Generalized stacking fault energies for embedded atom FCC metals', *Modelling Simul. Mater. Sci. Eng.* **8**, 103–115.

LIST OF FIGURES

1.2 Dislocation definition in simple cubic lattice 3

1.3 Edge, screw and mixed characteristics of dislocations 3

1.4 Thompson tetrahedron for fcc crystals 4

2.1 Simulation box for SFE calculation 11

2.2 Stacking fault energy and typical energy paths 12

2.3 Periodic simulation box used for SFFE calculations 13

2.4 Free energy of fcc iron as a function of temperature 14

2.5 Free energy of bcc iron as a function of temperature 14

2.6 Free energy difference due to anharmonicity 15

2.7 Effect of the integration accuracy on free energy calculations 15

2.8 Free energy difference between fcc and bcc phases of Fe 16

2.9 Effect of relaxation on stacking fault energy in Al 17

2.10 Effect of relaxation on stacking fault energy in Cu 17

2.11 Effect of relaxation on stacking fault energy in Fe 18

2.12 Stacking fault free energy as a function of temperature for Fe 19

3.1 Simulation box for partially periodic dislocation-SF interaction modeling 23

3.2 Fully periodic simulation box for dislocation-SF interaction modeling 24

3.3 Fully periodic model configuration for dislocation-SF interaction modeling with finite SF layer size 25

3.4 Supercell for fully periodic dislocation-SF interaction modeling with infinite SF layer . . 26

3.5 Fully periodic model configuration for dislocation-SF interaction modeling with infinite SF layer 27

3.6 Shear stress as a function of time acting on the partial dislocation predicted by partially-periodic modeling 29

3.7 History of stress components and temperature in Cu predicted by partially periodic modeling of dislocation-SF interaction 29

3.8 History of stress components and temperature in Cu predicted by fully periodic modeling of dislocation-SF 30

3.9 Snap shots of annihilation mode of interaction between dislocation and SF 32

3.10 Three snapshots of dislocation configuration and Burgers vector during annihilation mode of interaction 33

3.11 Zoomed view of annihilation and growth modes of interaction 33

3.12 Stress contour around an intrinsic stacking fault layer 34

3.13 Stress jumps around SF layer as function of distance from center of SF layer 34

3.14 Evolution of three non-zero strain components during simulation time for different interaction modes 35

4.1 Different simulation boxes used to study effect of twinning on stress-strain curve 39

4.2 Stress-strain curves for perfect fcc and twinned crystal under tensile strain loading 40

4.3 Stress-strain curves for perfect fcc and twinned crystals with a void under tensile strain loading 42

4.4 Stress-strain curves for perfect fcc and twinned crystal under shear strain loading 43

4.5 Stress-strain curves for perfect fcc and twinned crystals with a void under shear strain loading 45

4.6 Detwinning process under shear loading 46

4.7 Twin boundary oscillations under shear loading 46

4.8 Twin boundary motion through formation of partial dislocations 46

5.1 Bulk twin model based on partial dislocations 53

5.2 PN-based twin disregistry with three partial dislocation dipoles 54

5.3 Stacking fault energy of Cu and Al 57

5.4 An example of the disregistry and the corresponding stacking fault energy for Cu 59

5.5 Comparison between V-based and PN-based stacking fault energy calculation as a function of dislocation seperation 59

5.6 V-based and PN-based energy of the twin model as a function of the dislocation separation 60

5.7 Comparison of critical twinning stress based on V and PN models for three dislocation partials 60

5.8 Comparison of critical twinning stress based on V and PN models for one dislocation partial 61

5.9 Comparison of V- and PN-based interaction force for one dislocation dipole 63

5.10 Non-dimensional velocity of twin during the dynamic simulation and the steady-state dislocation separation 63

5.11 Dislocation separation as a function of external loading and twin thickness 64

6.1 Shear directions on the (111) plane associated with the phase fields 70

6.2 Stacking fault energy surface for Al and Cu as well as the stacking fault detection function 74

6.3 Disregistry profiles for a dissociated screw dipole in Cu 76

6.4 Disregistry fields associated with dissociated straight edge dislocations in Al and Cu . . 76

6.5 Initial state of the dislocation loop in Cu 77

6.6 PKF on the three (111) partial dislocations depending on loading 78

6.7 Stages of dynamic dislocation loop transformation in Al and Cu on (111) during T_{33} loading. 79

6.B.1 Relation between the different Burgers vector conventions 85

7.1 Stress field of single dislocation as a function of dislocation core size 90

7.2 Stress field of dislocation wall as a function of the dislocation spacing 90

7.1 Left-half of regularized box-car function with different transition thickness 93

7.2 Interaction stress based on strongly and weakly non-local calculations for sharp and diffuse density distributions 94

7.3 Maximum interaction stress calculated with strongly non-local model as a function of discretization 94

7.4 Dependence of pile-up distribution and dislocation number conservation on grid size . . 95

7.5 Evolution of an initially uniform dislocation distribution during loading 96

7.6 Pile-up distribution resulting from wall transport driven by the external stress based on strongly and weakly non-local models 96

7.7 Curve fits to the Volterra-based pile-up results and strongly non-local one 97

7.8 Pile-up of dislocations under external loading and without external loading due to surface effects 97

7.9 Dislocation density and internal stress profiles based on weakly non-local model 98

7.10 Dislocation density and internal stress profiles based on strongly non-local model 99

7.11 Pile-up distribution for different glide-plane spacings 99

7.A.1 Comparison of V- and PN-based shear stress fields around dislocation 101

7.B.1 Effect of numerical resolution on pile-up distribution with hard boundary condition . . . 103

7.B.2 Effect of numerical resolution on pile-up distribution with soft boundary condition . . . 103

INDEX

ABOP analytic bond order potential . 10, 16, 18

bcc body-centered cubic. 5, 10, 13–16
BV Burgers vector. 52

CFL Courant-Friedrichs-Lewy. 92
CNA common neighbor analysis. 12, 39

DFT discrete Fourier transform . 92
DFT density functional theory. 38, 51, 56, 58, 68, 73, 80

EA embedded atom. 16, 18, 28, 38
ESF extrinsic stacking fault . 11, 22, 23, 31, 35, 36

fcc face-centered-cubic. 5, 6, 9–19, 37–45, 47, 51, 53, 55, 64, 68, 69, 71, 73, 75, 77–80, 84
FD finite difference. 92
FFT fast Fourier transform . 92

GSFE generalized stacking fault energy . 10

hcp hexagonal close packed. 11–13, 18, 39, 53
HRTEM high resolution transmission electron microscopy. 1, 2, 67

ISF intrinsic stacking fault. 11, 22, 23, 28, 31, 35

MD molecular dynamics. 5, 6, 10–16, 21–25, 28, 37, 38, 72, 80
MS molecular statics. 5, 10, 11, 68, 71, 73–76, 80

PF phase field. 6, 68, 71–77, 79, 80
PKF Peach-Köhler force. 68, 77–79, 84–86
PN Peierls-Nabarro. 6, 51–53, 55–58, 60, 62–64, 88–99, 101, 102

QHA quasi-harmonic approximation . 5, 12, 14–16, 19

SF stacking fault. 4, 5, 9, 21–36, 51, 54, 59, 67, 68, 70, 74, 75, 77–80
SFE stacking fault energy. 4–6, 9–11, 16–19, 28, 31, 38, 51, 52, 56–62, 67, 68, 70, 73, 74, 76, 78–80
SFFE stacking fault free energy. 5, 10, 13, 16, 18, 19
SNL strongly non-local. 6, 87–100, 102

TI thermodynamic integration. 5, 10, 12, 14–16, 19
TRIP transformation induced plasticity . 1
TSF twinning stacking fault . 11, 17, 18
TWIP twinning-induced plasticity. 1, 9, 10, 18, 21

V Volterra. 51–58, 60, 62–64, 91, 96, 101, 102

WNL weakly non-local. 6, 87, 88, 90–95, 97–100